



저작자표시-비영리-변경금지 2.0 대한민국

이용자는 아래의 조건을 따르는 경우에 한하여 자유롭게

- 이 저작물을 복제, 배포, 전송, 전시, 공연 및 방송할 수 있습니다.

다음과 같은 조건을 따라야 합니다:



저작자표시. 귀하는 원저작자를 표시하여야 합니다.



비영리. 귀하는 이 저작물을 영리 목적으로 이용할 수 없습니다.



변경금지. 귀하는 이 저작물을 개작, 변형 또는 가공할 수 없습니다.

- 귀하는, 이 저작물의 재이용이나 배포의 경우, 이 저작물에 적용된 이용허락조건을 명확하게 나타내어야 합니다.
- 저작권자로부터 별도의 허가를 받으면 이러한 조건들은 적용되지 않습니다.

저작권법에 따른 이용자의 권리는 위의 내용에 의하여 영향을 받지 않습니다.

이것은 [이용허락규약\(Legal Code\)](#)을 이해하기 쉽게 요약한 것입니다.

[Disclaimer](#)

공학박사학위논문

극한 주행 핸들링 성능 개선을  
위한 토크벡터링 제어 알고리즘

**Torque vectoring control algorithm for  
enhanced limit handling performance**

2023년 2월

서울대학교 대학원

기계공학부

차 현 수

# 극한 주행 핸들링 성능 개선을 위한 토크벡터링 제어 알고리즘

Torque vectoring control algorithm for enhanced  
limit handling performance

지도교수 이 경 수

이 논문을 공학박사 학위논문으로 제출함

2022년 10월

서울대학교 대학원

기계공학부

차 현 수

차현수의 공학박사 학위논문을 인준함

2022년 12월

위원장 : 박종우 (인)

부위원장 : 이경수 (인)

위원 : 박용래 (인)

위원 : 김아영 (인)

위원 : 우승훈 (인)

## Abstract

# Torque vectoring control algorithm for enhanced limit handling performance

Hyunsoo Cha

Department of Mechanical Engineering

The Graduate School

Seoul National University

This dissertation comprehensively details the design of a torque vectoring control algorithm for enhanced cornering performance using two front in-wheel motors (IWMs) and electronic limited slip differential (eLSD) at the rear axle. The main scopes to be covered in this dissertation can be divided into two categories: 1) individual control of IWM for torque vectoring control at the front axle; 2) integrated control of IWM and eLSD for both front and rear axle.

First, an individual control strategy of two front IWMs in a rear-wheel-drive vehicle has been designed to improve the cornering performance. The individual control of IWMs consists of steady-state and transient control input. The steady-state control input is devised to improve the steady-state cornering response with modifying the vehicle understeer gradient, and the transient control input is designed to enhance the lateral stability by increasing the yaw rate damping coefficient. The proposed algorithm has been investigated through both computer simulations and vehicle tests, in order to show that the proposed algorithm can enhance the cornering response achieving the control objectives and to show the superior control performance compared to the other cases, such as yaw rate tracking algorithm and uncontrolled case.

Second, the integrated control of two front IWMs and eLSD is designed to enhance the cornering performance at high speeds considering the characteristics of

each actuator. The two front IWMs are controlled to improve the cornering performance based on a feedforward control, and the eLSD is utilized for the yaw rate feedback control. The computer simulations are conducted to show the effects of each actuator on the vehicle lateral motion at aggressive cornering with longitudinal acceleration and deceleration. Additionally, vehicle test results show that the proposed controller improves the cornering performance at the limits of handling compared to the uncontrolled case.

In summary, this dissertation proposes a control algorithm for an enhanced limit handling performance based on vehicle understeer gradient and yaw rate damping characteristics, addressing also integrated control of in-wheel motors and electronic limited slip differential with considering the characteristics of each actuator. The proposed IWM control law is formulated to shape the understeer characteristics during steady-state cornering and yaw rate damping characteristic during transient cornering, and the eLSD control is designed to track the reference yaw rate. Computer simulations and vehicle tests are conducted to validate the control performance of the proposed algorithm, showing significant improvements in the agility and the stability of a test vehicle without chattering issues. Additionally, the vehicle tests at a racing track confirm the enhanced limit handling performance.

**Keywords :** Torque vectoring control, Integrated chassis control, Nonlinear control, Vehicle dynamics and control, Vehicle state estimation

**Student Number :** 2018-25595

# Table of Contents

<b>Chapter 1. Introduction.....</b>	<b>1</b>
1.1. Background and motivation.....	1
1.2. Previous research on considering tire characteristics .....	4
1.2. Previous research on vehicle controller design .....	8
1.3. Thesis objectives .....	13
1.4. Thesis outline .....	15
<b>Chapter 2. Vehicle Control System .....</b>	<b>17</b>
2.1. Vehicle chassis system.....	17
2.2. Vehicle tire–road interactions .....	22
2.3. Tire characteristics at the limits of handling.....	35
<b>Chapter 3. Torque Vectoring Control with In–Wheel Motors (IWMs) .....</b>	<b>49</b>
3.1. Upper level controller .....	53
3.1.1. Control strategies for steady–state response .....	54
3.1.2. Control strategies for transient response.....	57
3.1.3. Analysis on the closed–loop system with proposed controller .....	60
3.2. Lower level controller.....	65
3.2.1. Actuator characteristics of in–wheel motors.....	65
3.2.2. Torque inputs for yaw moment generation .....	66
<b>Chapter 4. Integrated Control of Two Front In– Wheel Motors (IWMs) and Rear–Axle Electronic</b>	

<b>Limited Slip Differential (eLSD) .....</b>	<b>68</b>
4.1. Upper level controller .....	71
4.1.1. Analysis on actuator characteristics and vehicle responses .....	71
4.1.2. Feedforward control using in-wheel motors .....	79
4.1.3. Feedback control using electronic limited slip differential .....	80
4.2. Lower level controller.....	82
4.2.1. Transforming the desired yaw moments to the torque command.....	82
4.2.2. Saturating the torque inputs considering the actuator and tire friction limit .....	83
4.2.3. Transferring the eLSD clutch torque in the desired direction.....	84
<b>Chapter 5. Simulation Results .....</b>	<b>87</b>
5.1. Effect of IWM control on vehicle motion .....	87
5.2. Effect of IWM/eLSD integrated control .....	98
<b>Chapter 6. Vehicle Test Results .....</b>	<b>108</b>
6.1. Test results for IWM control.....	108
6.2. Test results for integrated control of IWM and eLSD .....	116
<b>Chapter 7. Conclusion.....</b>	<b>121</b>
<b>Appendix A. Integrated control of two front in-wheel</b>	

<b>motors and rear wheel steering .....</b>	<b>123</b>
A.1. Prediction model for vehicle motion .....	124
A.2. Controller design .....	128
A.3. Simulation results .....	131
<b>Bibliography .....</b>	<b>138</b>
<b>Abstract in Korean.....</b>	<b>148</b>



## List of Figures

Figure 2.1. Advantages and limitations of each chassis module ...	18
Figure 2.2. Benefits for the integrated control of various chassis module .....	21
Figure 2.3. Identification results for the Magic Formula at pure longitudinal slip with optimized parameters .....	27
Figure 2.4. Identification results for the Magic Formula at pure lateral slip with optimized parameters.....	29
Figure 2.5. Identification results for the Magic Formula at combined slip with optimized parameters .....	31
Figure 2.6. Proposed friction ellipse model using optimization technique .....	37
Figure 2.7. Test vehicle and setup for the measurements of tire and vehicle states .....	38
Figure 2.8. Block diagram of the test vehicle for data acquisition .....	39
Figure 2.9. Road shape of a racing track for data acquisition.....	40
Figure 2.10. Comparison of the vehicle test data on a racing track and identified friction ellipse model using the indoor test data.....	42
Figure 2.11. Concept of the normlized friction circle .....	43
Figure 2.12. Longitudinal and lateral friction use on a racing track by an expert driver .....	45
Figure 2.13. Friction use with respect to the curvature of the vehicle trajectory .....	47
Figure 3.1. Target vehicle architecture and vehicle model.....	49
Figure 3.2. Concepts of the two cornering characteristics .....	51

Figure 3.3. Block diagram of the proposed in-wheel motor control algorithm.....	52
Figure 3.4. Vehicle cornering conditions.....	59
Figure 3.5. The effects of three design parameters in proposed control law .....	63
Figure 3.6. (a) Two front in-wheel motors equipped in test vehicle and (b) in-wheel motor T-N curve.....	65
Figure 4.1. Block diagram for the integrated control of in-wheel motors and electronic limited slip differential.....	69
Figure 4.2. Control strategy of the proposed algorithm .....	70
Figure 4.3. Vehicle model description: (a) the architecture of powertrain and (b) 3-DOF planar model and bicycle model .....	72
Figure 4.4. A schematic of eLSD equipped in the rear axle of the test vehicle .....	73
Figure 4.5. Yaw moment generation by a locked differential: (a) acceleration in a turn and (b) deceleration in a turn .....	78
Figure 4.6. State transition diagram for the eLSD activation condition .....	85
Figure 5.1. Vehicle states for the circular turn scenario with a constant radius of 30 m .....	90
Figure 5.2. Understeer curve in a circular turn with a constant radius of 30m .....	91
Figure 5.3. Open-loop step steer at 80 kph .....	93
Figure 5.4. Yaw rate damping coefficient identification .....	94
Figure 5.5. Closed-loop double lane change at 65 kph.....	96
Figure 5.6. Open-loop sinusoidal steering input with acceleration.. ..	101

Figure 5.7. Open-loop sinusoidal steering input with deceleration..	105
Figure 5.8. Open-loop step steer test at 80kph with a steady-state lateral acceleration of 0.7 g.....	107
Figure 6.1. Test vehicle setup .....	108
Figure 6.2. Block diagram of the test vehicle .....	109
Figure 6.3. Vehicle test results for closed-loop circular turn....	112
Figure 6.4. Vehicle test results for closed-loop double lane change test.....	114
Figure 6.5. Test vehicle setup .....	116
Figure 6.6. Block diagram of the test vehicle .....	117
Figure 6.7. Vehicle test results on a racing track.....	120
Figure A.1. (a) Target vehicle architecture and (b) 3-DOF planar model and bicycle model.....	125
Figure A.2. Block diagram for the integrated control of in-wheel motors and rear wheel steering .....	129
Figure A.3. Concept of the reference trajectory .....	130
Figure A.4. Open-loop sine with dwell at 100 kph .....	134
Figure A.5. Closed-loop double lane change at 100 kph .....	136

# Chapter 1 Introduction

## 1.1. Background and motivation

Numerous chassis modules that can improve the vehicle agility, maneuverability, stability, and handling performance of vehicles have been developed. Traditional chassis systems incorporate Anti-skid Brake System (ABS), Electronic Stability Control (ESC), Electronic Control Suspension (ECS), and Active Roll System (ARS). More recently, drivetrain and steering system are combined to improve the cornering performance of vehicles, such as torque vectoring (TV) and active steering system that includes rear wheel steering (RWS), active front steering (AFS), and four wheel steering (4WS). Recently, these chassis modules are quite common for need to be applied in one chassis system for options. In particular, the integrated system of various chassis modules can be applied in high-performance vehicles for improved handling performance.

Compared to the individual chassis module, the integrated system of multiple chassis modules can provide a higher level of handling performance and active safety. Especially for high-performance vehicles, multiple chassis modules are equipped in one vehicle to improve the cornering performance at the limits of handling. Since the integrated chassis system is not a simple sum of subsystems, the interaction between the multiple chassis modules should be considered to design the controller for the integrated system. Additionally, the influence of the individual chassis modules on vehicle response should be analyzed and considered to coordinate the control inputs of the various chassis modules.

Among the various chassis modules, the torque vectoring system are of interest in this study. Torque vectoring system can show to be promising candidates in enhancing the cornering performance of vehicles by appropriately transferring the engine torque to the front and rear axles or left and right wheels. Traditional torque vectoring systems, such as limited-slip differentials and dual-clutch differentials, have hardware limitations to be used for this purpose [Piyabongkarn'10]. For example, limited-slip differentials can only transfer torque from the faster wheel to the slower wheel, and dual-clutch differentials cannot generate forward and reverse torque simultaneously [Rubin'15]. However, compared to these traditional torque-vectoring devices, in-wheel motors have several advantages with regards to handling performance and lateral stability due to their ability to deliver torque to each wheel independently [Watt'10]. Additionally, in-wheel motors not only boast fast response times but are also capable of generating forward and reverse torque [Murata'12]. By utilizing the merits of in-wheel motors, in-wheel motor control can contribute to improving the dynamic performance of vehicles to a significantly higher level. Additionally, in-wheel motors can increase efficiency of electric vehicles through the regenerative braking [Pugi'20, Xu'19]. And the eLSD can transfer the wheel torques from one wheel to the other wheel by locking the differential case and one axle shaft [Piyabongkarn'10].

Especially, among the various torque vectoring devices and their integration with other chassis modules, the main scope of this study can be classified into three categories: 1) in-wheel motor (IWM); 2) in-wheel motor (IWM) and electronic limited slip differentials (eLSD); 3) in-wheel motor (IWM) and rear wheel steering (RWS). The in-wheel motors can generate the independent forward and reverse torques in each wheel with fast and direct torque inputs [Murata'12, Watts'10]. The

eLSD can only transfer the left and right wheel torques from one wheel to the other wheel by locking the clutch between the differential case and one axle shaft, though this device can only transfer torque from the faster wheel to the slower wheel [Piyabongkarn'07, Piyabongkarn'10, Hancock'07, Cha'22]. The RWS can improve vehicle handling performance and stability from mild handling to limit handling maneuvers by controlling the additional rear lateral tire forces [Park'20].

These three chassis modules can be properly controlled for the improvements of cornering performance from mild handling to limit handling driving situations. Moreover, the integrated control of these devices can be desirable approaches for limit handling control. Particularly, the focus of this dissertation is on developing a torque vectoring control with two front IWMs and eLSD at rear axle for enhanced limit handling performance. Additionally, the integrated control of torque vectoring and rear wheel steering was also handled in Appendix A.

## 1.2. Previous research on considering tire characteristics

Basically, since the tire forces in each wheel are determined by the interaction between the road and tire, the studies for the tire characteristics are the main issue to be revealed in vehicle dynamics and control. Though there are a lot of studies to describe the tire responses, it is still a challenging issue to investigate the mathematical representation of tire responses. This challenge comes from the nonlinear tire responses at combined slip and near the limits of handling.

A great deal of researches have focused on the mathematical description of tire characteristics. Pacejka comprehensively details the fundamental concepts of tire characteristics in ‘Tire and vehicle dynamics’ [Pacejka’05]. Among several tire models, the Magic Formula model is one of the representative semi-empirical model for the description of actual tire responses [Pacejka’92, Bakker’87]. Luge model describes a dynamic force for longitudinal tire and road interaction [Canudas-de-Wit’03]. UniTire model can describe the nonlinear and non-steady-state tire response for vehicle simulation and control under complex wheel motion considering the lateral slip, longitudinal slip, turn slip, and camber angles [Kuo’05]. Modified Magic Formula can account for parameters that influence road and tire contact, such as tire type, vehicle speed, and slips [Cabrera’18]. Machine learning techniques can be utilized to generate a tire force model for real-time estimation [Xu’ 20]. Some other researches are conducted to explore the identification of tire model parameters. Ortiz et al. proposed an optimization based on genetic algorithm to obtain a parameter set that can be utilized for the Magic Formula model

[Ortiz'06], with a follow-up study with self-adapting parameters of the optimization algorithm [Ortiz'09]. Alagappan et al. compared the numerous algorithms for obtaining the model coefficients of the Magic Formula, and discussed about the encounter issues for each algorithm [Alagappan'15]. Brach et al. revealed the limitation for the accuracy of friction circle model to describe the tire force limits [Brach'11].

Considering these tire characteristics at the limits of handling, some studies have been conducted to explore the vehicle control scheme at handling limits. Kritayakirana et al. designed an autonomous racing controller to gain insights into vehicle control at the friction limits, mimicking race driver's internal vehicle model [Kritayakirana'12]. Beal et al. presented an approach to vehicle stabilization by defining state boundaries that can exclude unstable vehicle dynamics and utilizes a model predictive envelope controller to bound the vehicle motion within the stable region of the state space [Beal'12]. Kapania et al. presented a feedback-feedforward steering controller that simultaneously maintains vehicle stability at the limits of handling while minimizing lateral path tracking deviation [Kapania'15]. Siampis et al. proposed a nonlinear model predictive control strategy for stabilization near the limit of lateral acceleration using the rear axle electric torque vectoring configuration [Siampis'17]. Herrmann et al. presented an optimization-based velocity planner that is mathematically formulated as a multi-parametric Sequential Quadratic Problem (mpSQP) [Herrmann'20]. De Castro et al. addressed the problem of minimum time manoeuvring in electric vehicles, and Smith et al. studied the effect of both passive and actively-controlled vehicle handling characteristics on minimum time maneuvering for vehicles with four-wheel torque vectoring system [De Castro'14, Smith'18]. Heilmeyer et al. showed a software



stack capable of planning a minimum curvature trajectory on the basis of an occupancy grid map and introduced a controller design that allows to follow the trajectory at the handling limits [Heilmeier'19]. Kapania et al. presented an iterative algorithm that divides the path generation task into two sequential sub-problems for maneuvering through a race course in minimum time [Kapania'16]. Subosits et al. derived a model that captures the effects of road topography on tire forces in emergency situations at tire force limits [Subosits'15]. Li et al. proposed a linear predictive lateral control method to stabilize an automated vehicle at the tire-road friction limits [Li'20]. Laurence et al. presented a slip angle-based control strategy of maintaining the front tires at the peak slip angle [Laurence'17].

Additionally, some other studies focused on the estimation of tire friction limits and force limits. Hsu et al. presented a model-based estimation method that utilizes pneumatic trail in steering torque to identify lateral handling limits that are defined by the tire slip angle and peak lateral force limits [Hsu'10]. Singh et al. aimed at estimating the tire-road friction coefficient by using brush tire model [Singh'15]. Choi et al. proposed a methodology to identify the tire-road friction coefficient in real time by means of linearized recursive least squares methods based on the combined longitudinal and lateral brush tire model [Choi'13]. Wang et al. estimated the tire-road friction coefficient through the integrated longitudinal and lateral force using a brush tire model [Wang'15]. Ribeiro et al. adopted a time delay neural network (TDNN) to detect and estimate road friction coefficient under lateral force excitations avoiding the use of tire models [Ribeiro'20]. Khaleghian et al. conducted a literature survey introducing different approaches that are widely used to estimate the tire friction and model parameters [Khaleghian'17]. Ko et al. suggested a road friction coefficient estimation method with estimating the

longitudinal and normal forces acting on the tire using onboard sensor measurements and motor torque information [Ko'15]. Zhang et al. presented an estimation framework based on a novel tire model and modified square-root cubature Kalman filter (SCKF) in order to identify the road friction coefficient of the left and right wheels [Zhang'22].

### 1.3. Previous research on vehicle controller design

On the other hand, due to the recent successes and growing interests in the field of machine learning, several studies have attempted data-driven approach in the field of vehicle dynamics and control. Rosolia et al. presented a learning model predictive controller for iterative tasks, improving the control performance by learning from previous iterations [Rosolia'17]. Kabzan et al. presented a learning-based control approach for autonomous racing with an application to the AMZ Driverless race car [Kabzan'19]. Hewing et al. summarized and categorized previous research on learning-based MPC [Hewing'20]. Mantripragada et al. proposed a model-free reinforcement learning-based control that can adapt to changing tire characteristics and effectively utilizing the available grip at tire-road interface [Mantripragada'22]. Ji et al. proposed a vehicle dynamics stability strategy using the adaptive radial basis function network sliding mode control (ARBFN-SMC) to learn the system uncertainty and eliminate its adverse effects [Ji'18]. Xu et al. applied machine learning techniques to estimate the tire forces with real-time processing of a tri-axial acceleration sensor data from an intelligent tire system [Xu'20]. However, these data-driven approaches for vehicle control requires comprehensive data on vehicle responses and iterative tasks for learning. Additionally, it is not desirable to utilize a data-driven approach in limit handling control due to the safety reasons that comes from the potential risk at untrained driving circumstances.

Returning to the previous works for controller design, many studies have been

conducted to enhance the cornering performance with the individual control of IMW, eLSD, and RWS. There are many researches about individual IWM control for vehicle lateral stability. The general approach for IWM control is to track the references of yaw rate and sideslip angle with vehicle state estimation. Kaiser et al. proposed feedback and feedforward controllers to track the references of yaw rate and sideslip angle with a linear quadratic Gaussian (LQG) control [Kaiser'11]. Geng et al. also designed feedback and feedforward controller to track the yaw rate and sideslip angle references with a linear quadratic regulator (LQR) control, estimating the sideslip angle based on a fuzzy observer with two bicycle models of high and low cornering stiffness [Geng'09, Geng'07]. Xiong et al. achieved a real-time update of the controller's feedforward and feedback gains through online estimation of the tire cornering stiffness [Xiong'12]. De Novellis et al. conducted a comparison between different torque-vectoring control structures for the yaw moment control of fully electric vehicles, evaluating two second-order sliding mode controllers against a feedforward controller combined with either a conventional or an adaptive PID controller [De Novellis'14]. Chen et al. designed a yaw moment controller to track the yaw rate reference based on the sliding mode control [Chen'13]. Nam et al. designed a lateral stability control of IWM vehicles based on sideslip angle estimation using lateral tire force sensors [Nam'12]. Nam et al. designed an adaptive sliding mode controller to address vehicle model parameter uncertainties [Nam'15]. Ding et al. and Zhang et al. proposed a second-order sliding mode controller with setting the derivative of the control input as a new control input [Ding'17, Zhang'16]. Park et al. designed a smooth sliding mode controller applying a boundary layer near the switching surface [Park'20]. Fujimoto et al. estimated front and rear tire cornering stiffnesses based on a yaw-

moment observer to track the yaw rate and side slip angle references [Fujimoto'06]. In most previous research for IWM control, the approach for lateral motion control was to design and track the yaw rate references. However, yaw rate tracking control can induce chattering issues in the case of in-wheel motor control without input smoothing techniques. This was especially the case for the high frequency steering inputs into the vehicle, where chattering issues were exacerbated. The chattering issue can be explained by the reference yaw rate being determined through the driver's steering angle. Under high frequency steering inputs, high-frequency yaw rate errors are induced, resulting in the chattering of the feedback control. Additionally, control input smoothing techniques, such as second-order sliding mode control and integral sliding mode control, cannot avoid the trade-off between chattering alleviation and control performance.

There are also a few previous studies to improve the lateral stability by reducing yaw rate overshoot with eLSD control. Piyabongkarn et al. designed a PI controller to reduce the yaw rate error [Piyabongkarn'07]. Hancock et al. proposed a linear quadratic regulator (LQR) to reduce the yaw rate error and sideslip angle error [Hancock'07]. Rubin et al. designed a model predictive controller using a linear parameter-varying (LPV) vehicle model to minimize the yaw rate and sideslip angle errors [Rubin'15]. Woo et al. presented a front-axle eLSD control algorithm to prevent excessive understeer during acceleration in a turn [Woo'21]. However, integrated control with other chassis modules are not investigated for eLSD control.

Additionally, some other researches have been conducted for lateral stability control using active steering system, such as active front steering (AFS) and rear wheel steering (RWS). Sano et al. proposed a traditional rear wheel steering algorithm in a manner that the rear wheels are steered in the same direction (or

opposite direction) as the front wheels when the vehicle speed is kept within a high range (or low range) [Sano'87]. Kim et al. designed an AFS control for crosswind disturbance compensation for the reduction of driver steering effort [Kim'14]. Ariff et al. proposed a four wheel steering control strategy to achieve the smaller turning radius for a low speed maneuver [Ariff'15]. Yu et al. designed a disturbance observer based control for four wheel steering vehicles to cope with the crosswind disturbance [Yu'16]. Nagai et al. proposed a feedback controller to maintain the zero sideslip angle based on a model-following RWS control [Nagai'97]. Lee et al. devised a four-wheel independent steering aiming to reduce the sideslip angle and actuating power [Lee'99]. Eguchi et al. designed a controller to make the sideslip angle to zero considering both lateral and suspension dynamics [Eguchi'89].

On the other hand, it is important to consider the interaction between the chassis modules in designing the integrated control of multiple chassis modules. In this regard, many studies on the integrated chassis control have been performed. Her et al. proposed a coordinating algorithm to improve the limit handling performance for the differential braking, traction torques, and active roll moment. The optimization-based control allocation is used to distribute the multiple actuator control inputs [Her'16]. Yim proposed a coordinated control with AFS, RWS and ESC based on the weighted pseudo-inverse based control allocation (WPCA) [Yim'15]. Yim et al. designed an integrated chassis controller for a four-wheel independent steering system in an in-wheel motor driving system [Yim'21]. Warth et al. designed a central feedforward control for rear-wheel steering and torque vectoring based the input-output linearization [Warth'20]. Vignati et al. proposed the coordination of RWS and torque vectoring (TV) achieved by weighting their contribution based on their impact on vehicle dynamic. Based on phase portrait

analysis, a performance index is proposed to weight more control action (TV or RWS) capable of leading vehicle at the nearest equilibrium point with fastest rate [Vignati'22]. Peters et al. proposed an integrated feedforward control of TV and RWS for improved driving performance [Peters'19]. Cha et al. designed an integrated control of IWM and eLSD considering the actuator characteristics [Cha'22]. Cho et al. proposed an integrated control of AFS and ESC with optimized coordination for the desired yaw moment and longitudinal force based on the Karush-Kuhn-Tucker (KKT) conditions [Cho'12]. Yim et al. compared the control performance based on the weighted pseudo-inverse-based control allocation (WPCA) between the active front steering (AFS), front wheel independent steering (FWIS), four wheel steering (4WS), and four wheel independent steering (4WIS) [Yim'20]. Nah et al. investigated and compared the effects of integrated control among AFS, RWS, TV, and ESC [Nah'19].

Among the various chassis module integrations, the main thesis of this dissertation concerns the integrated control of two front IWMs and an eLSD at rear axle. However, the two torque vectoring devices (i.e., IWM and eLSD) of interest in this dissertation have potential risks in their use for lateral motion control. Since the IWM actuators directly control the wheel torques and yaw moment, it can cause chattering problems for the yaw rate feedback control. The eLSD actuators can only transfer wheel torque from the faster wheel to the slower wheel. By integrating the two torque vectoring systems, the potential risk of the two devices can be complemented each other. Considering these actuator characteristics, in this research, the in-wheel motors are utilized for the feed-forward control to avoid the chattering issues, while the eLSD is employed for the feedback control to improve the robustness of the algorithm.

## 1.4. Thesis objectives

This dissertation focused on developing a torque vectoring control with two front in-wheel motors (IWMs) and electronic limited slip differential (eLSD) at rear axle. From the literature reviews, it can be confirmed that the torque vectoring control has the potential to improve the vehicle cornering performance from mild handling to limit handling maneuvers. Moreover, its integrated control with other chassis modules, such as RWS, can provide a higher level of cornering performance and vehicle safety compared to the individual torque vectoring control, as shown in Appendix A.

In particular, in this dissertation, an approach for the integrated control of IWMs and eLSD has been proposed to improve the handling performance in consideration of the characteristics of each actuator. The objective of the proposed control algorithm is to improve the lateral stability and prevent vehicle spinout at the limits of handling. The integrated control algorithm consists of a supervisor, upper-level, and lower-level controller. The supervisor determines the target motion based on a target understeer gradient and yaw rate reference. In the upper-level controller, the desired yaw moments for IWM and eLSD are calculated to generate the target motion. The desired yaw moment for IWM is designed to improve the cornering performance with a feedforward control based on a target understeer gradient. The desired yaw moment for eLSD is devised to reduce the yaw rate error with a feedback control based on a yaw rate reference. In the lower-level controller, the torques commands for IWMs and eLSD are determined based on the desired yaw moments. The tire friction limits are estimated using a tire model to avoid excessive torque inputs and tire saturation. Lastly, the performance of the proposed



control algorithm has been investigated via computer simulations and vehicle tests. The computer simulation has been conducted using the Carsim and Simulink Software. The vehicle tests have been performed using a rear wheel drive vehicle equipped with in-wheel motors in the two front wheels and an eLSD module in the rear axle. The vehicle test results show that the proposed algorithm can improve the handling performance in high-speed cornering at the limits of handling.

## 1.5. Thesis outline

The main scope of this dissertation can be classified into two categories: 1) torque vectoring control with in-wheel motors (IWM); 2) integrated control of IWMs and electronic limited slip differential (IWM and eLSD); The control algorithm for the two cases has been proposed in this study, and their control performance for each algorithm has been investigated via both the computer simulations and vehicle tests. The simulation and vehicle test results show that the proposed algorithm can contribute to improving the cornering and handling performance not only on mild maneuvers but also on limit handling maneuvers.

This dissertation is structured in the following manner. Chapter 2 introduces the fundamental characteristics of vehicle chassis system with tire characteristics, and discuss about the effects of individual and integrated chassis modules on vehicle responses. Chapter 3 explains the proposed torque vectoring control with in-wheel motors. In Chapter 4, the integrated control of in-wheel motors and electronic limited slip differential is proposed and its effects for the improvements of cornering performance is investigated. In Chapter 5, computer simulation results has been presented to show the effects of IWM and eLSD control on vehicle motion. Chapter 6 shows the vehicle test results to validate that the proposed algorithms can successfully enhance the vehicle cornering performance in actual vehicles. Chapter 7 summarizes this dissertation and mentions the future works to be further studied.

The main contributions of this dissertation can be summarized as follows:

(1) This dissertation proposes a control algorithm for enhanced limit handling performance based on vehicle understeer gradient and yaw rate damping

characteristics, addressing also an integrated control of in-wheel motors and electronic limited slip differential with considering the characteristics of each actuator.

(2) The proposed in-wheel motor control law is formulated to shape the understeer characteristics during steady-state cornering and yaw rate damping characteristic during transient cornering, and the eLSD control is designed to track the reference yaw rate.

(3) Computer simulations and vehicle tests have been conducted to validate the control performance of the proposed algorithm, showing significant improvements in the agility and stability of a test vehicle without chattering issues. Additionally, the vehicle tests at a racing track presents the enhanced limit handling performance.

# Chapter 2 Vehicle Control System

## 2.1. Vehicle chassis system

Before designing the controllers for vehicle chassis system, it is required to understand the characteristics of vehicle chassis system. Basically, vehicle motion is determined by the interaction between the tire and road, since the three-axial tire forces dominate the vehicle dynamics and motion. By adjusting the tire forces in each tire of a vehicle, the vehicle motion can be improved or deteriorated.

In a baseline vehicle (i.e., vehicle without any additional control actuators), vehicle motion is determined by the drivers' steering angle and pedal inputs. However, chassis modules can modify the vehicle motion by adjusting the tire forces at each tire using the additional equipped actuators, such as torque vectoring and active steering system.

On the other hand, various chassis control modules can be implemented in one vehicle to improve the vehicle stability and maneuverability [Her'16]. Among the various chassis modules, chassis modules for lateral motion control are of interest in this study. For example, active front steering (AFS) and rear wheel steering (RWS) can generate the additional steering angles and lateral tire forces to make the additional yaw moment and to improve the vehicle lateral motion. Additionally, torque vectoring (TV) and Electronic Stability Control (ESC) can generate the additional wheel torques and longitudinal tire forces, also improving the lateral motion with additional yaw moment. However, there are advantages and limitations for each chassis module.

Based on the considerable previous researches that is introduced in Section 1.2, the advantages and limitations of each chassis module can be arranged as Figure 2.1. As shown in Figure 2.1, the effects of each chassis module can be categorized in three: 1) Lateral stability; 2) Maneuverability; 3) Drivability. Lateral stability means the ability to sustain the yaw rate and sideslip angle responses with respect to the driver steering angle. Maneuverability stands for the ability to generate neutral steering characteristics. Drivability in Figure 2.1 is defined as the ability for maintaining the robust vehicle response to the external disturbances, such as crosswind and bank angle.

Module		Lateral Stability	Maneuverability	Drivability
Active Steering	AFS	OS & US prevention	low-speed maneuver	Less steering effort with correction
	RWS			
Torque Vectoring	IWM	OS & US & RO prevention	high-speed maneuver	-
	eLSD	OS Prevention Semi-active (dependent on wheel speed difference)	Wheel slip prevention Not effective in the moderate maneuver	-
ESC		OS & US & RO prevention Deceleration	-	Cope with sudden crosswind

\* Abbreviation  
 OS : oversteer      ■ Advantages  
 US : understeer    ■ Limitations  
 RO : roll-over  
 - : No previous study

Figure 2.1. Advantages and limitations of each chassis module.

Additionally, each chassis modules have the advantages and potential limitations to be considered in designing the individual and integrated control of various chassis modules, as shown in Figure 2.1. For example, for lateral stability, active steering system, such as AFS and RWS, can prevent the vehicle oversteer (OS) and

understeer (US). However, active steering system is not effective to be utilized for the rollover (RO) prevention, since decelerating the vehicle speed is the fundamental solution for rollover. On the other hand, in-wheel motors can control oversteer, understeer and rollover, since they can directly adjust the wheel torques in each wheel. Moreover, electronic limited slip differential (eLSD) can only control oversteer, generate the yaw moment outward to the cornering direction, since eLSD can only transfer the wheel torques from the faster (cornering outward) to slower (cornering inward) wheel. Electronic stability control (ESC) can prevent oversteer, understeer and rollover with differential braking. However, ESC should decelerate the vehicle speed, since the additional yaw moment in this system is generated via braking forces at each wheel.

For maneuverability, active steering system can be effective in improving the low-speed maneuver. However, active steering is not that effective in the high-speed cornering, since this system cannot improve the tire friction use. On the other side, in-wheel motor (IWM) control can enhance the maneuverability at high speed cornering, though it is not effective at low speed. Electronic limited slip differential (eLSD) can prevent wheel slip and indirectly improve the maneuverability at the limits of handling, since this system can prevent the tire saturation at high speed cornering. However, electronic stability control (ESC) is not a desirable chassis system to be utilized for maneuverability, since the intervention by differential braking can deteriorate the driving comfort.

For drivability, active steering and electronic stability control (ESC) can be utilized to compensate the disturbances like crosswind. However, there is not reported research paper about the torque vectoring control for disturbance compensation, since the main purpose of the torque vectoring control is to improve

the cornering performance of a vehicle.

Another issue to be considered is the effects and benefits for the integrated control of various chassis modules. Figure 2.2 summarizes the benefits for the integrated control of four chassis modules: 1) Active front steering (AFS); 2) Rear wheel steering (RWS); 3) Torque vectoring (TV); 4) Electronic Stability Control (ESC). Based on the four individual chassis modules, the expected control performance when chassis modules are added and integrated one by one has been investigated.

Basically, the four chassis modules (i.e., AFS, RWS, TV, and ESC) each have their own advantages and expected control performance for integration in one chassis system. For example, AFS has an advantage in improve the vehicle yaw rate response by providing an additional steering angle in addition to the driver steering angle. RWS is particularly effective in reducing the vehicle sideslip angle and improving the maneuverability at low-speed cornering. TV is specialized in improving the high-speed maneuverability and lateral stability in high lateral acceleration maneuvers. This is because TV system can use overall tire friction more efficiently by transferring the wheel torques from saturated tire to unsaturated tire. Lastly, ESC shows the best performance in improving the lateral stability and reducing the sideslip angle. However, frequent intervention of ESC can deteriorate the driving comfort with deceleration.

Based on advantages of each chassis module, some desirable integrations of multiple chassis modules can be considered. For the integrations of two chassis modules, four cases can be desirable: 1) AFS+RWS; 2) RWS+TV; 3) RWS + ESC; 4) ESC+TV. For the three module integrations, two cases can be considered: 1) AFS+RWS+TV; 2) RWS+TV+ESC.

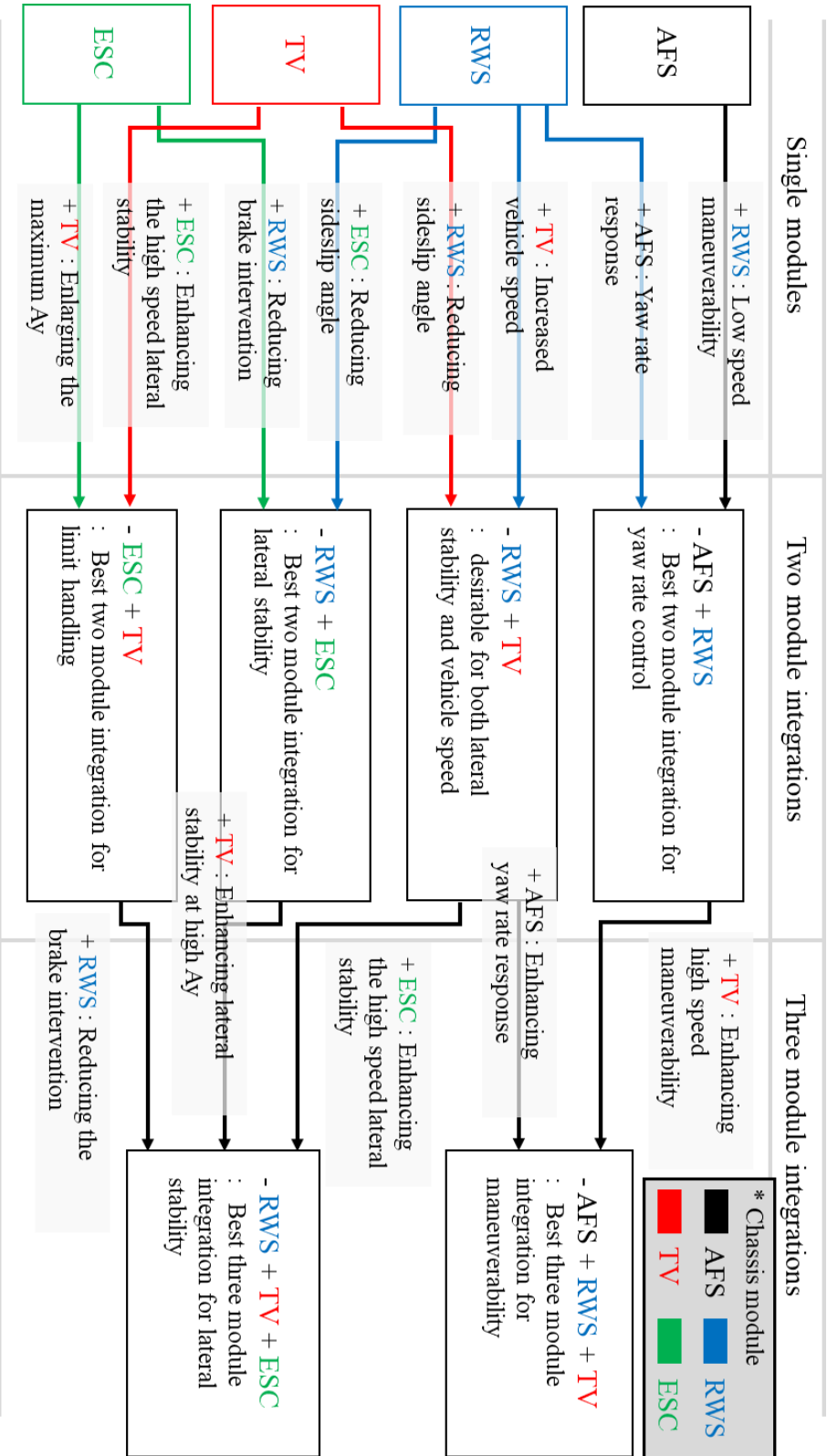


Figure 2.2. Benefits for the integrated control of various chassis modules.



## 2.2. Vehicle tire–road interactions

Since the vehicle motion is determined by the tire forces, it is necessary to investigate the tire characteristics. In this section, analysis on tire characteristics has been conducted using the two types of data: 1) indoor test data; 2) vehicle test data. In order to acquire the required data, two measurement system are utilized for each of the two tests. For the indoor test, a flat track test platform is utilized to obtain the tire forces and status in a precisely controllable and measurable conditions. Additionally, for the vehicle test data, a test vehicle is developed equipped with a wheel force transducer (WFT) at each wheel and a Differential Global Position System (DGPS). The test vehicle is manipulated by an expert driver for consistent measurement. The purpose of this analysis is to obtain a deeper insight into vehicle control through an analysis of the tire characteristics at the limits of handling. For the analysis of indoor test data, the Magic Formula [Pacejka'05] is utilized to derive the appropriate model parameters that can describe the real-world tire characteristics.

Additionally, in order to describe the tire force limits at the limits of handling, an optimization-based friction ellipse model has been proposed. The optimal solution for the proposed optimization problem can provide an envelope that can express the tire force limits. Additionally, based on the proposed friction ellipse model, a normalized friction circle model has been proposed to quantify tire friction use based on the proposed friction ellipse. The proposed method can contribute to quantitatively express tire characteristics with monitoring the friction use of each wheel.

In order to conduct the analysis on the tire characteristics on the Magic Formula

model, several tire measurements are required as follows: 1) slip angle  $\alpha$ ; 2) slip ratio  $\lambda$ ; 3) camber angle  $\gamma$ ; 4) longitudinal tire force  $F_x$ ; 5) lateral tire force  $F_y$ ; 6) vertical tire force  $F_z$ . In order to obtain these tire measurements under precisely controllable and measurable conditions, the Measure Test Simulate (MTS) Flat-Track test platform was utilized as a test rig. This platform was chosen for its capability to apply vertical, camber, steer, and drive/braking inputs to a rotating tire on flat surface. The type of flat belt was selected for the same condition to the dry asphalt road surface, following the recommendations of the manufacturer. The indoor test data has been recorded via the built-in filtering logic for the MTS Flat-Track test platform. The identification procedure is conducted using the indoor flat track test by means of an MTS Flat Track machine [Braghin'06, Braghin'11].

The Magic Formula model was utilized to derive the tire properties and characteristics using the acquired measurement data [Pacejka'05, Pacejka'92, Bakker'87]. The each model parameters in the Magic Formula have the intrinsic meaning, allowing the quantitative understanding of the tire characteristics, based on the identified model parameters that fit the indoor test data. The model parameters of the Magic Formula have been derived by means of an optimization technique that is devised to minimize the errors between the Magic Formula model and measured data [Ortiz'06, Ortiz'09, Alagappan'15], using the MATLAB function *lsqnonlin*.

In order to derive the proper tire model parameters using optimization techniques, tire measurements filter via the build-in logic were recorded for three cases: 1) Case 1: pure longitudinal slip; 2) Case 2: pure lateral slip; 3) Case 3:

Combined slip. Firstly, for pure longitudinal slip cases, the slip angle and camber angle were set to zero, and the slip ratio was varied for fixed camber angles and vertical loads. Secondly, for the pure slip angle cases, the slip ratio was fixed to zero, and the slip angle was changed for the fixed camber angle and vertical loads. Thirdly, for the combined slip cases, the slip ratio was altered with fixed values of slip angle, camber angle, and vertical force.

For the three cases, optimization has been performed to obtain the proper model parameter sets for the minimization of the tire force errors between the Magic Formula and measurements. Additionally, in order to prevent the over-fitting, the upper and lower bounds for the model parameters has been set referring the common range of the model parameters, following the recommendation of tire test engineer.

Before explaining the optimization processes, a brief summary for the tire model is conducted for clarity. The Magic Formula model [Pacejka'05, Pacejka'92, Bakker'87] has been utilized to describe the tire measurements. The tire force for pure lateral slip can be formulated as follows:

$$F_{y0} = D_y \cdot \sin[C_y \cdot \arctan\{B_y x - E_y \cdot (B_y x - \arctan(B_y x))\}] + V_y, \quad (1a)$$

$$\begin{aligned} C_y &= a_0, \quad D_y = \mu_y F_z, \quad \mu_y = (a_1 F_z + a_2) \cdot (1 - a_{15} \gamma^2), \\ BCD_y &= a_3 \cdot \sin(2 \cdot \arctan(F_z / a_4)) \cdot (1 - a_5 \cdot |\gamma|), \\ B_y &= BCD_y / (C_y D_y), \\ E_y &= (a_6 F_z + a_7) \cdot (1 - (a_{16} \gamma + a_{17}) \cdot \text{sgn}(\alpha + H_y)), \\ H_y &= a_8 F_z + a_9 + a_{10} \cdot \gamma, \\ V_y &= a_{11} F_z + a_{12} + (a_{13} F_z^2 + a_{14} F_z) \cdot \gamma, \\ B_y x &= B_y \cdot (\alpha + H_y), \end{aligned} \quad (1b)$$

The tire force for the pure longitudinal can be described as follows:

$$F_{x0} = D_x \cdot \sin[C_x \cdot \arctan\{B_x x - E_x \cdot (B_x x - \arctan(B_x x))\}] + V_x, \quad (2a)$$

$$\begin{aligned}
C_x &= b_0, \quad D_x = \mu_x F_z, \quad \mu_x = b_1 F_z + b_2, \\
BCD_x &= (b_3 \cdot F_z^2 + b_4 F_z) \cdot e^{(-b_5 F_z)}, \\
B_x &= BCD_x / (C_x D_x), \\
E_x &= (b_6 F_z^2 + b_7 F_z + b_8) \cdot (1 - b_{13} \cdot \text{sgn}(\lambda + H_x)) \\
H_x &= b_9 F_z + b_{10}, \\
V_x &= b_{11} F_z + b_{12}, \\
B_x x &= B_x \cdot (\lambda + H_x),
\end{aligned} \tag{2b}$$

Equations (1a) and (1b) correspond to the lateral force in case of the pure side slip, and Equations (2a) and (2b) correspond to the longitudinal force for the pure longitudinal slip. The model coefficients for the above equations, i.e.,  $a_0 - a_{17}$  and  $b_0 - b_{13}$ , are the model parameters for lateral and longitudinal forces.

Additionally, the formula extension for the combined slip correction [Pacejka'05, Bakker'87] can be described as follows:

$$F_y = \frac{\alpha^*}{\sigma^*} \cdot F_{y0}(\sigma^*), \quad F_x = \frac{\lambda^*}{\sigma^*} \cdot F_{y0}(\sigma^*), \tag{3a}$$

$$\lambda^* = \lambda / \lambda_{peak}, \quad \alpha^* = \alpha / \alpha_{peak}, \quad \sigma^* = \sqrt{(\lambda^*)^2 + (\alpha^*)^2}, \tag{3b}$$

$$\lambda_{peak} = c_0 F_z + c_1, \quad \alpha_{peak} = c_2 F_z + c_3, \tag{3c}$$

In the above equations, Equation (3a) corresponds to the lateral and longitudinal force at combined slip, and Equation (3b) and (3c) correspond to the included model parameter in Equation (3a). The variables in Equation (3b) are the normalized longitudinal slip, normalized lateral slip, and the resultant slip. In Equation (3c), the models for peak slip ratio and peak slip angle was slightly modified as a linear model instead of setting the peak values as constants to consider the effects of vertical force variation.  $c_1$  and  $c_3$  are the peak slip ratio and peak slip angle, respectively.  $c_0$  and  $c_2$  are the load influence on peak slip ratio and peak slip angle, respectively. Based on the 36 parameter in the model, i.e.,  $a_0 - a_{17}$ ,  $b_0 - b_{13}$ , and  $c_0 - c_3$ , the tire characteristics can be obtained by means of

an optimization technique.

For the pure longitudinal slip cases, the longitudinal tire force model in Equations (2a) and (2b) was utilized to obtain the tire characteristics at pure longitudinal slip. The model coefficients in Equation (2b), i.e.,  $b_0 - b_{13}$ , are obtained by solving the optimization problem as follows [Ortiz'06, Ortiz'09, Alagappan'15]:

$$\min \sum_{i=1}^n \sum_{j=1}^m \left[ F_{x0}(X_{lon}, \lambda_i, F_{z,j}) - F_{x,meas}(\lambda_i, F_{z,j}) \right]^2, \quad (4a)$$

$$s.t. \underline{X}_{lon} \leq X_{lon} \leq \bar{X}_{lon},$$

$$X_{lon} = [b_0, b_1, \dots, b_{13}], \quad (4b)$$

where  $X_{lon}$  is an model coefficient set for longitudinal tire force model;  $\underline{X}_{lon}$  and  $\bar{X}_{lon}$  are the upper and lower bounds of the model coefficients for pure longitudinal slip;  $m$  and  $n$  are the number of cases for vertical load and longitudinal slip at each vertical load case, respectively.

The objective of the optimization problem is to obtain the model parameter set that can minimize the sum of the squared errors between the model and measured data. The data for pure longitudinal slip was measured for three load cases, i.e., 2290N, 4580N, and 5950N. For each load case, the longitudinal slip were varied from -0.5 to 0.5. The identified model and its parameters have been presented in Figure 2.3 and Table 2.1. As shown in Figure 2.3, the tire model with optimized parameters can describe the longitudinal tire forces at pure longitudinal slip. Table 2.1 summarizes the specific values of the model parameters and their intrinsic meaning.

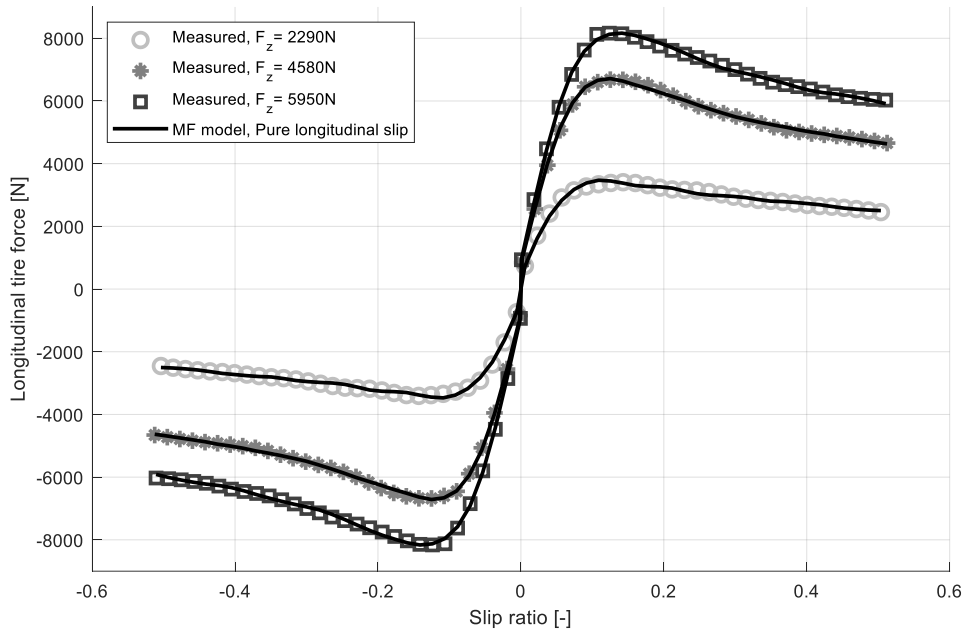


Figure 2.3. Identification results for the Magic Formula at pure longitudinal slip with optimized parameters.

Table 2.1. Longitudinal force parameters for pure longitudinal slip case.

Longitudinal coefficients	Units	Value
$b_0$ : shape factor for longitudinal force	-	1.7653
$b_1$ : load influence on longitudinal friction coefficient (* 1000)	1/kN	-83.013
$b_2$ : longitudinal friction coefficient (* 1000)	-	1522.8
$b_3$ : curvature factor of stiffness/load	N/%/kN <sup>2</sup>	0.0012
$b_4$ : change of stiffness with slip	N/%	313.53
$b_5$ : change of progressivity stiffness/load	1/kN	0.0994
$b_6$ : curvature change with squared load	-	0.0447
$b_7$ : curvature change with load	-	-0.4350
$b_8$ : curvature factor	-	0.8946
$b_9$ : load influence on horizontal shift	%/kN	0.3308
$b_{10}$ : horizontal shift	%	-0.8199
$b_{11}$ : vertical shift	N	-447.84
$b_{12}$ : vertical shift at zero load	N	617.88
$b_{13}$ : curvature shift	-	0.6970

The lateral tire force model in Equations (2a) and (2b) was adopted to investigate the tire forces for pure lateral slip cases. The model parameters in Equation (2b), i.e.,  $a_0 - a_{17}$  are also obtained via optimal solution of the following problem [Ortiz'06, Ortiz'09, Alagappan'15]:

$$\min \sum_{i=1}^n \sum_{j=1}^m \sum_{k=1}^l \left[ F_{y0}(X_{lat}, \alpha_i, F_{z,j}, \gamma_k) - F_{y,meas}(\alpha_i, F_{z,j}, \gamma_k) \right]^2 \quad (5a)$$

$$s.t. \underline{X}_{lat} \leq X_{lat} \leq \bar{X}_{lat}$$

$$X_{lat} = [a_0, a_1, \dots, a_{17}] \quad (5b)$$

where  $X_{lat}$  is the parameter set to be optimized for the lateral tire force description;  $\underline{X}_{lat}$  and  $\bar{X}_{lat}$  are the upper and lower bounds for the lateral force model coefficients;  $m$  and  $l$  are the number of vertical load and camber angle cases;  $n$  is the number of side slip angles at each case;

The objective of the presented optimization problem is to obtain the model coefficients for the lateral tire force that can minimize the sum squared error between the lateral tire force model and measured forces. The tire forces were measured for the tire slip angles ranging from -11.75deg to 11.75deg for the three load cases (2290N, 4580N, and 6870N) and three camber angle cases (-5deg, 0deg, 5deg), i.e., nine cases. The Magic Formula for pure lateral slip is shown in Figure 2.4, and the model parameters for pure lateral slip are presented in Table 2.2.

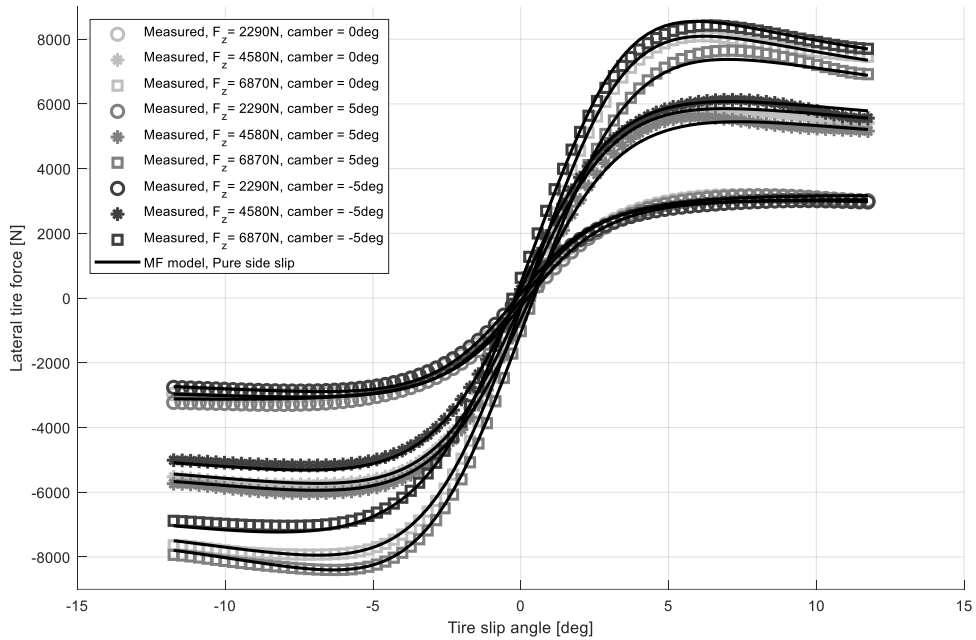


Figure 2.4. Identification results for the Magic Formula at pure lateral slip with optimized parameters.

Table 2.2. Lateral force parameters for pure side slip case.

Lateral coefficients	Units	Value
$a_0$ : shape factor for lateral force	-	1.5310
$a_1$ : load influence on lateral friction coefficient (* 1000)	1/kN	-42.284
$a_2$ : lateral friction coefficient (* 1000)	-	1457.3
$a_3$ : change of stiffness with slip angle	N/deg	2823.9
$a_4$ : change of progressivity of stiffness/load	1/kN	10.494
$a_5$ : camber influence on stiffness	%/deg/10 0	0.0094
$a_6$ : curvature change with load	-	-0.2671
$a_7$ : curvature factor	-	1.1602
$a_8$ : load influence on horizontal shift	deg/kN	-0.0099
$a_9$ : horizontal shift at zero load and zero camber	deg	-0.0836
$a_{10}$ : camber influence on horizontal shift	deg/deg	-0.0153
$a_{11}$ : vertical shift	N	3.9390
$a_{12}$ : vertical shift at zero load	N	47.352



$a_{13}$	: camber influence on vertical shift, load dependent	N/deg/kN	-1.5153
$a_{14}$	: camber influence on vertical shift	N/deg	-6.6162
$a_{15}$	: camber influence on lateral friction coefficient	1/deg	6.5348e <sup>-4</sup>
$a_{16}$	: curvature change with camber	-	0.1169
$a_{17}$	: curvature shift	-	-0.4956

In order to extract the tire properties at combined slip, the Magic Formula model with combined slip correction has been utilized. As shown in Equations (1a)-(3c), it is necessary to consider the 36 parameters to describe the tire forces at combined slip. Based on these models, following optimization problem was devised to obtain a model parameter set for combined slip cases:

$$\min \sum_{h=1}^o \sum_{i=1}^n \sum_{j=1}^m \sum_{k=1}^l \left[ \begin{aligned} & \left\{ F_y(X, \lambda_h, \alpha_i, F_{z,j}, \gamma_k) - F_{y,meas}(\lambda_h, \alpha_i, F_{z,j}, \gamma_k) \right\}^2 \\ & + \left\{ F_x(X, \lambda_h, \alpha_i, F_{z,j}, \gamma_k) - F_{x,meas}(\lambda_h, \alpha_i, F_{z,j}, \gamma_k) \right\}^2 \end{aligned} \right] \quad (6a)$$

$$s.t. \underline{X} \leq X \leq \bar{X}$$

$$X = \begin{bmatrix} X_{lat} \\ X_{lon} \\ X_{comb} \end{bmatrix} = \begin{bmatrix} a_0, a_1, \dots, a_{17} \\ b_0, b_1, \dots, b_{13} \\ c_0, c_1, c_2, c_3 \end{bmatrix} \quad (6b)$$

where  $X$  indicates the all the model parameters for longitudinal/lateral tire forces and their combined slip correction.  $\underline{X}$  and  $\bar{X}$  presents the upper and lower bounds for the model coefficients.  $X_{lat}$ ,  $X_{lon}$  and  $X_{comb}$  indicates the model coefficients for lateral force, longitudinal force, and combined slip correction, respectively.  $n$ ,  $m$  and  $l$  are the number of side slip angle cases, vertical load cases and camber angle load cases, respectively.  $o$  means the number of longitudinal slip ratios in each case.

Similarly in the previous optimization problem, the optimization objective is to minimize the errors in longitudinal and lateral tire forces between the tire model

and measurements. The longitudinal slip ratio was changed from -0.5 to 0.5 in three vertical loads (2290N, 4580N, and 6870N), four tire slip angles (-2deg, 2deg, 5deg, and 8deg), and three camber angles (-5deg, 0deg, and 5deg). Particularly, among the three camber angle cases, only the zero camber angle cases is presented in Figure 2.5 representatively. The optimized model parameters are arranged in Table 2.3. The model. However, it should be noted that the tire force characteristics at tire slip angles of -2deg and 2deg shows the difference due to the asymmetric sidewall shape and surface pattern in the tested tire, though the Magic Formula model shows the symmetric tire characteristics.

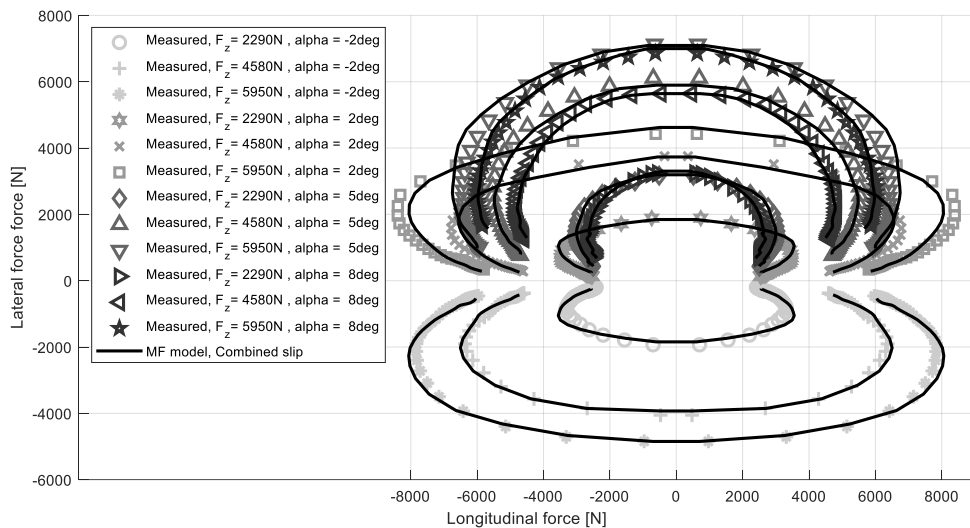


Figure 2.5. Identification results for the Magic Formula at combined slip with optimized parameters.

Table 2.3. Magic Formula model parameters for combined slip case.

Parameter	Value	Parameter	Value	Parameter	Value
$a_0$	1.5128	$a_{12}$	-2.7527	$b_6$	0.4632
$a_1$	75.709	$a_{13}$	-895.89	$b_7$	-4.9482

$a_2$	1670.0	$a_{14}$	1378.6	$b_8$	8.7204
$a_3$	1102.2	$a_{15}$	4.2334e <sup>-4</sup>	$b_9$	-0.2735
$a_4$	3.9543	$a_{16}$	-0.5895	$b_{10}$	-0.0050
$a_5$	9.2307	$a_{17}$	-0.4141	$b_{11}$	-69.718
$a_6$	4.5692	$b_0$	1.6710	$b_{12}$	86.356
$a_7$	9.7136	$b_1$	-58.229	$b_{13}$	-0.8966
$a_8$	0.5191	$b_2$	1723.2	$c_0$	-34.083
$a_9$	1.1885	$b_3$	1.5735e <sup>-4</sup>	$c_1$	82.984
$a_{10}$	38.944	$b_4$	388.34	$c_2$	-18.165
$a_{11}$	18.977	$b_5$	0.0833	$c_3$	44.425

In order to quantitatively evaluate and compare the fitted results in other camber angle cases at combined slip, two indicators are considered: 1) Sum-squared error (SSE); 2) Mean-squared error (MSE). Since only the results for zero camber angle cases is presented, SSE and MSE for other camber angles (-5deg and 5deg) are compared together, the equations for SSE and MSE can be described as follows [Ortiz'06, Ortiz'09, Alagappan'15]:

$$SSE = \sum_{h=1}^o \sum_{i=1}^n \sum_{j=1}^m \left[ \begin{aligned} & \left\{ F_y(X, \lambda_h, \alpha_i, F_{z,j}, \gamma_k) - F_{y,meas}(\lambda_h, \alpha_i, F_{z,j}, \gamma_k) \right\}^2 \\ & + \left\{ F_x(X, \lambda_h, \alpha_i, F_{z,j}, \gamma_k) - F_{x,meas}(\lambda_h, \alpha_i, F_{z,j}, \gamma_k) \right\}^2 \end{aligned} \right], \quad (7a)$$

$$MSE = \sqrt{\frac{\sum_{h=1}^o \sum_{i=1}^n \sum_{j=1}^m \left[ \begin{aligned} & \left\{ F_y(X, \lambda_h, \alpha_i, F_{z,j}, \gamma_k) - F_{y,meas}(\lambda_h, \alpha_i, F_{z,j}, \gamma_k) \right\}^2 \\ & + \left\{ F_x(X, \lambda_h, \alpha_i, F_{z,j}, \gamma_k) - F_{x,meas}(\lambda_h, \alpha_i, F_{z,j}, \gamma_k) \right\}^2 \end{aligned} \right]}{\sum_{h=1}^o \sum_{i=1}^n \sum_{j=1}^m \left[ \left\{ F_{y,meas}(\lambda_h, \alpha_i, F_{z,j}, \gamma_k) \right\}^2 + \left\{ F_{x,meas}(\lambda_h, \alpha_i, F_{z,j}, \gamma_k) \right\}^2 \right]}} \times 100, \quad (7b)$$

Based on the above equations, SSE and MSE for other camber angle cases are calculated and evaluated as follows: 1) For the camber angle of 0deg, SSE is  $1.0511 \cdot 10^7$  and MSE is 3.26; 2) For the camber angle of 5deg, SSE is  $2.0106 \cdot 10^7$  and MSE is 4.47; 3) For the camber angle of -5deg, SSE is

$4.1606 \cdot 10^7$  and MSE is 6.36. From these results, it can be shown that the errors in tire forces between the tire model and measurements increases at combined slip with additional camber angle, i.e., 5deg and -5deg, showing the complex tire characteristics at combined slip with additional camber angles.

Additionally, Table 2.4 shows the comparison in the identified tire model parameters between the pure slip (i.e., pure longitudinal slip and pure lateral slip) and combined slip cases. The ‘Pure’ column indicates values of the identified tire model parameters for pure side slip and pure longitudinal slip cases. In the values in ‘Pure’ column, the tire model parameters for pure side slip (i.e.,  $a_0 - a_{17}$ ) indicate the obtained values using the pure sideslip cases, and the tire model parameters for pure longitudinal slip (i.e.,  $b_0 - b_{13}$ ) stands for the derived values from the pure longitudinal slip cases. Additionally, the parameter values in the ‘Comb’ column are obtained from the combined slip cases. As shown in Table 2.4, it should be noted that the parameters values for the ‘Pure’ and ‘Comb’ columns are different. This further shows the difficulty in determining a single parameter set that can fully describe the all operating regions of the tire incorporating pure side slip cases, pure longitudinal slip cases, and combined slip cases.

Table 2.4. Comparison of Magic Formula model parameters between pure longitudinal/lateral slip and combined slip cases.

Param	Pure	Comb	Param	Pure	Comb	Param	Pure	Comb
$a_0$	1.5310	1.5128	$a_{12}$	47.352	-2.7527	$b_6$	0.0447	0.4632
$a_1$	-42.284	-75.709	$a_{13}$	-1.5153	-895.89	$b_7$	-0.4350	-4.9482
$a_2$	1457.3	1670.0	$a_{14}$	-6.6162	1378.6	$b_8$	0.8946	8.7204
$a_3$	2823.9	1102.2	$a_{15}$	$6.5348e^{-4}$	$4.2334e^{-4}$	$b_9$	0.3308	-0.2735
$a_4$	10.494	3.9543	$a_{16}$	0.1169	-0.5895	$b_{10}$	-0.8199	-0.0050
$a_5$	0.0094	9.2307	$a_{17}$	-0.4956	-0.4141	$b_{11}$	-447.84	-69.718
$a_6$	-0.2671	-4.5692	$b_0$	1.7653	1.6710	$b_{12}$	617.88	86.356

$a_7$	1.1602	9.7136	$b_1$	-83.013	-58.229	$b_{13}$	0.6970	-0.8966
$a_8$	-0.0099	-0.5191	$b_2$	1522.8	1723.2	$c_0$	0.0447	-34.083
$a_9$	-0.0836	1.1885	$b_3$	0.0012	$1.5735e^{-4}$	$c_1$	-0.4350	82.984
$a_{10}$	-0.0153	-38.944	$b_4$	313.53	388.34	$c_2$	0.8946	-18.165
$a_{11}$	3.9390	-18.977	$b_5$	0.0994	0.0833	$c_3$	0.3308	44.425

Additionally, from these results, it can be confirmed that Magic Formula parameters cannot sufficiently describe the tire force limits. As shown in Equations (1a)-(2b), the longitudinal and lateral friction coefficients can be expressed as  $\mu_x = b_1 F_z + b_2$  and  $\mu_y = (a_1 F_z + a_2) \cdot (1 - a_{15} \gamma^2)$  that is the maximum lateral and longitudinal forces that can be generated by the side slip angle and slip ratio. In this regard, it can be confirmed that the friction ellipse using the Magic Formula parameters is not enough to describe the tire force limits. In this regard, it is required to propose a new approach to represent the tire force limits. Thus, a new approach for expressing the tire force limits has been proposed, which can be utilized under the condition that the tire measurements can be sufficiently obtained.

### 2.3. Tire characteristics at the limits of handling

Tire force limit is a substantial factor that influences the vehicle motion at the limits of handling. In particular, excessive wheel torque input can deteriorate the vehicle cornering performance at handling limits. In order to consider this issue, the friction ellipse model stands as one of the widely utilized models in vehicle control to consider the tire force limits [Zhang'20, Ataei'17, 'Ataei'20, Li'15, Cha'22]. The friction ellipse model express the tire force limits based on the tire forces and friction coefficients. The friction ellipse model for each  $i$  ( $= fl, fr, rl, rr$ ) can be expressed as follows:

$$\left( \frac{\mu_x}{\mu_{x,\max}} \right)^2 + \left( \frac{\mu_y}{\mu_{y,\max}} \right)^2 = 1, \quad (8a)$$

$$\mu_x = F_{x,i} / F_{z,i}, \quad \mu_y = F_{y,i} / F_{z,i}, \quad (8b)$$

where  $\mu_x$  and  $\mu_y$  stands for the longitudinal and lateral friction coefficients, respectively;  $\mu_{x,\max}$  and  $\mu_{y,\max}$  are their maximum values.

However, it should be noted that the maximum values for the friction coefficient (i.e.,  $\mu_{x,\max}$  and  $\mu_{y,\max}$ ) can differ depending on the tire characteristics. The maximum friction coefficients is varied for identical road surface conditions depending on the type of tire to be used. As an example, a certain high-performance tire shows the longitudinal coefficient of around 1.5 on a dry asphalt surface. On the other hand, for some tires, the longitudinal friction coefficient does not exceed 1.0 on the same road surface (i.e., dry asphalt). In this regard, it is another issue to determine the appropriate friction ellipse model in consideration of

tire characteristics. A new approach to address this issue will be introduced in the next section.

In this section, an optimization based friction ellipse model has been presented in order to describe and estimate the tire force limits from the sufficient measurements in tire characteristics. A convex optimization problem to be utilized for the identification of the friction ellipse model can be expressed as follows [Boyd'04]:

$$\min \left( \frac{1}{2} \mu_{x,\max}^2 + \frac{1}{2} \mu_{y,\max}^2 \right), \quad (9a)$$

$$s.t. \quad \frac{(F_{x,i}/F_{z,i})^2}{\mu_{x,\max}^2} + \frac{(F_{y,i}/F_{z,i})^2}{\mu_{y,\max}^2} - 1 \leq 0, \quad i=1, \dots, n, \quad (9b)$$

$$\mu_{x,\max,lb} \leq \mu_{x,\max} \leq \mu_{x,\max,ub}, \quad \mu_{y,\max,lb} \leq \mu_{y,\max} \leq \mu_{y,\max,ub}, \quad (9c)$$

where  $\mu_{x,\max}$  and  $\mu_{y,\max}$  are the optimization variables to be derived;  $\mu_{x,\max,lb}$  and  $\mu_{x,\max,ub}$  are the lower and upper bounds for  $\mu_{x,\max}$ , respectively;  $\mu_{y,\max,lb}$  and  $\mu_{y,\max,ub}$  are the lower and upper bounds for  $\mu_{y,\max}$ , respectively;  $n$  is the number of measured data.

The objective of proposed optimization problem is to find the friction ellipse with minimum area that contains the tire force measurements in the friction ellipse. In order to apply the this method, the data for the combined slip cases were utilized again. As shown in Figure 2.6, three friction ellipses were derived for three vertical load cases (2290N, 4580N, and 5950N). Using the proposed method, the maximum friction coefficients can be obtained. Additionally, the friction ellipse in Figure 2.6 shows that the optimal solutions from the proposed optimization problem can generate the proper friction ellipses that appropriately envelop the tire force

measurement. This result has been compared with the vehicle test results on a dry asphalt road, further explained in the next subsection.

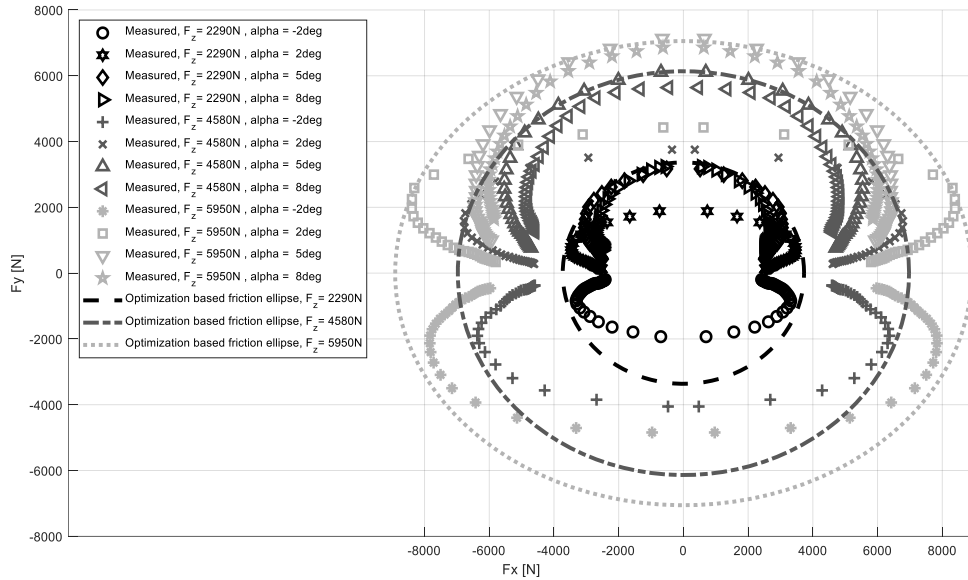


Figure 2.6. Proposed friction ellipse model using optimization technique.

The racing track test was performed to compare the tire force limit model with the tire force measurements during driving test with the help of a professional driver. Since the race car drivers and highly skilled driver can instinctively utilize the tire forces to the limits without losing control, such as spin-out and run-off-road, analyzing their driving data can provide some insights into the tire force limits.

In order to achieve the purpose, a test vehicle has been developed based on a rear-wheel-drive D-sedan to measure and analyze the handling characteristics and tire forces by an expert driver. As shown in Figure 2.7, two additional measurement devices have been additionally equipped in the test vehicle: 1) A Differential Global Positioning System (DGPS); 2) A wheel force transducers (WFTs) for each wheel. The DGPS and WFTs can collect data regarding the vehicle position and



velocity with three axial tire forces at each wheel. The DPGS was mounted in the trunk with an industrial computer and a MicroAutobox, and the four WFTs were mounted on each wheel hub. Additionally, a data acquisition module (DAQ module) for the WFTs was installed on the back seats. The DQA module has the ability to filter the measurement noise and other outliers by the built-in filtering logic.

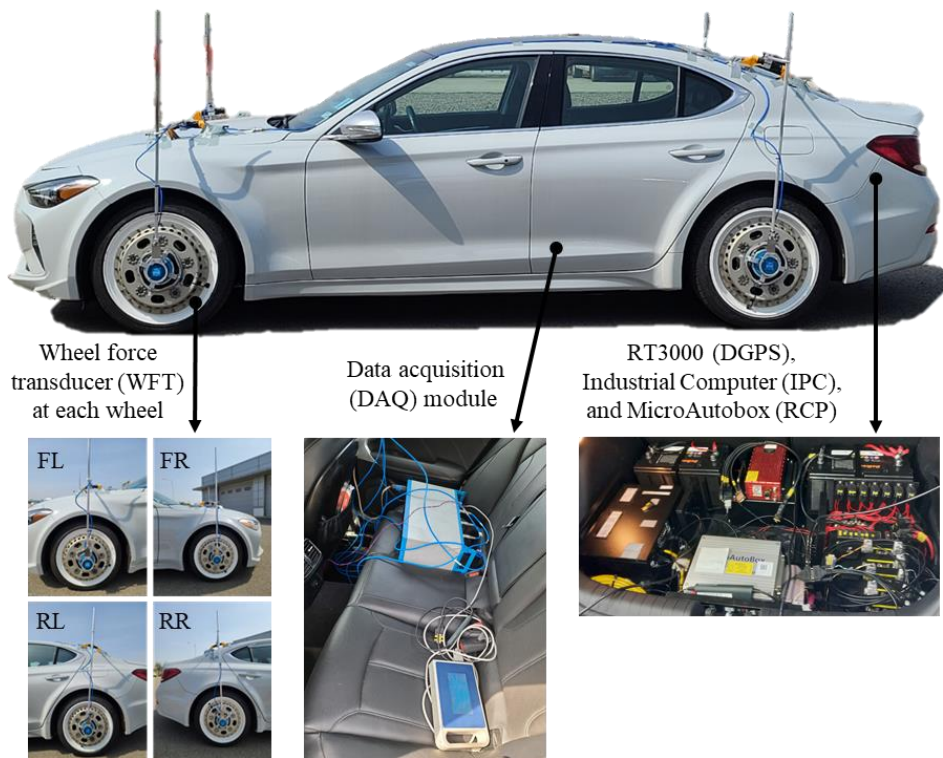


Figure 2.7. Test vehicle and setup for the measurements of tire and vehicle states.

The block diagram of the test vehicle is illustrated in Figure 2.8. The measurements from all sensors (i.e., on-board sensors, DGPS signals, and WFT signals) are transmitted to the Controller Area Network (CAN) bus, and the measurements from the sensors are transmitted to the MicroAutobox via CAN communication. MicroAutobox receives and records these sensor signals and

measurements in the industrial computer (IPC), and the industrial computer retrieves data from the Radio Technical Commission for Maritime Services (RTCM) using the Standard for Networked Transport of RCTM via Internet Protocol (NTRIP).

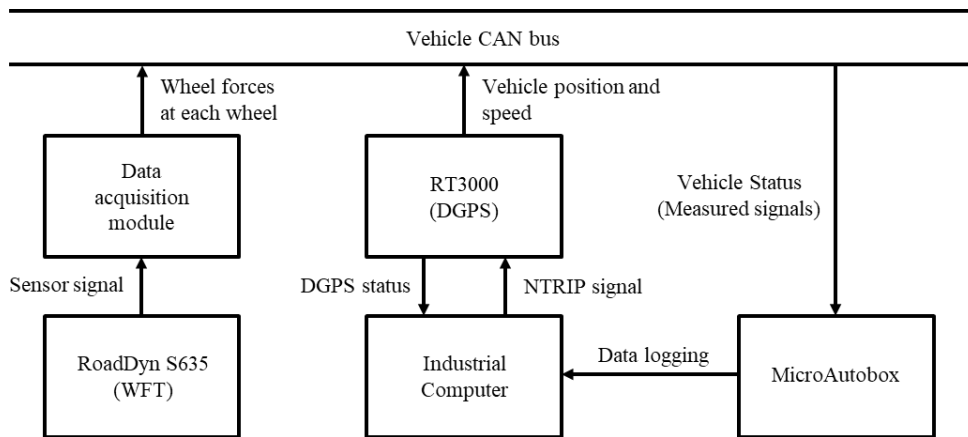


Figure 2.8. Block diagram of the test vehicle for data acquisition.

Figure 2.9 shows the road shape of the racing circuit for the data acquisition with the test vehicle. On this circuit, a professional driver tried to drive 10 consecutive laps in counterclockwise direction, minimizing the overall lap times and using the tire friction maximally. The red dotted line in Figure 2.9 stands for a vehicle path where the driver recorded the minimum lap time among the 10 laps. Additionally, the vehicle states and tire forces from on-board and additional sensors were measured in order to analyze the driving data of the professional driver. In particular, the measurements near the two hairpin corners that are shown in Figure 2.9(b) and (c) are important, since the tire friction limit can be mainly achieved near the hair corners. Since the tire force usage by professional driver can provide some important insights, further analysis has been conducted in the next subsection.

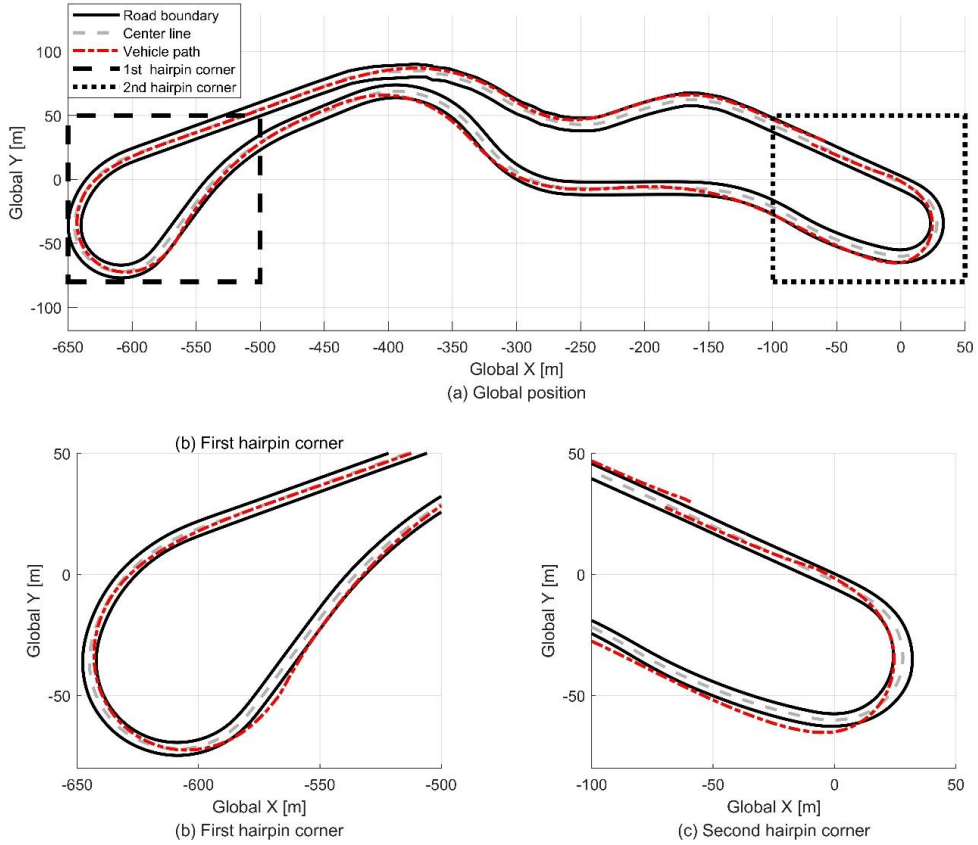


Figure 2.9. Road shape of a racing track for data acquisition.

While the vertical tire force can be fixed in the indoor test by the indoor test platform, it cannot be fixed in the vehicle tests due to the load transfer during the driving and cornering. Thus, for the fair comparison between the measurements from indoor tests and vehicle tests, the longitudinal and lateral forces were expressed as their normalized values by vertical tire forces, i.e.,  $F_x/F_z$  and  $F_y/F_z$ . As shown in Figure 2.10, the proposed friction ellipse model using the indoor test data were compared with the measured tire forces in vehicle tests with a normalized forces. The black dotted line in Figure 2.10 indicates the identified friction ellipse model from the indoor test data. However, it should be noted that

the friction ellipse is represented as a constant ellipse for graphical representation, although the shape of the proposed friction ellipse model varies depending on the vertical forces. Additionally, the ideal friction circle with friction coefficients of 1.0 and 1.1 were drawn together in the red and blue lines, respectively, of Figure 2.10 for comparison with conventional methodologies.

Figure 2.10 indicates that the normalized tire forces from vehicle tests protrude out of the friction circles with friction coefficient of 1.0 and 1.1. Thus, the conventional friction circle model with a pre-defined friction coefficient cannot provide an accurate description of the tire force limits. Though a perfect prediction for the tire force limits still proves to be challenging, the proposed friction ellipse model can better describe the tire force limits compared to the ideal friction circle model with a predetermined friction coefficient.

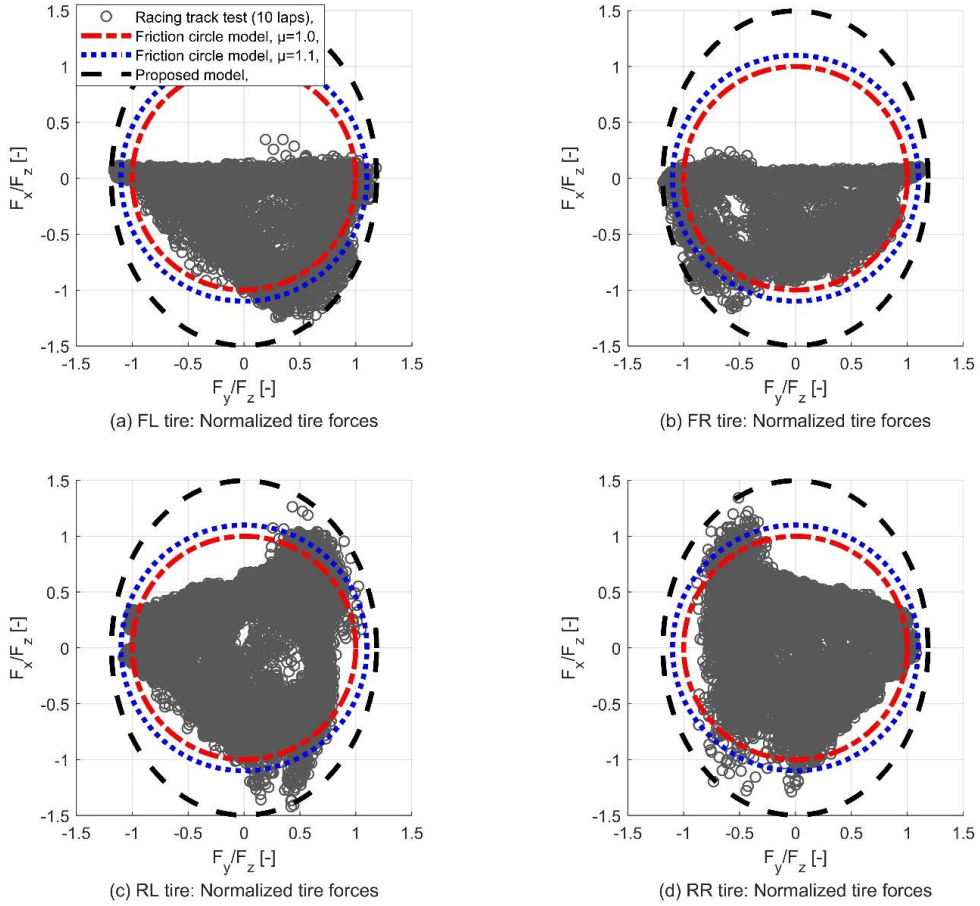


Figure 2.10. Comparison of the vehicle test data on a racing track and identified friction ellipse model using the indoor test data.

Based on the proposed approach in the previous section, the friction use for sliding tires can be quantified in order to monitor the tire behaviors. In order to quantify the friction use in sliding contact tires, a normalized friction circle has been proposed in this study. Before explaining about the concept of the normalized friction circle, it is necessary to state about the tire curves, as shown in Figure 2.11. The longitudinal and lateral curves show that the maximum values of longitudinal and lateral friction coefficients can be achieved at peak slip ratio  $\lambda_{peak}$  and peak

slip angle  $\alpha_{peak}$ , respectively.

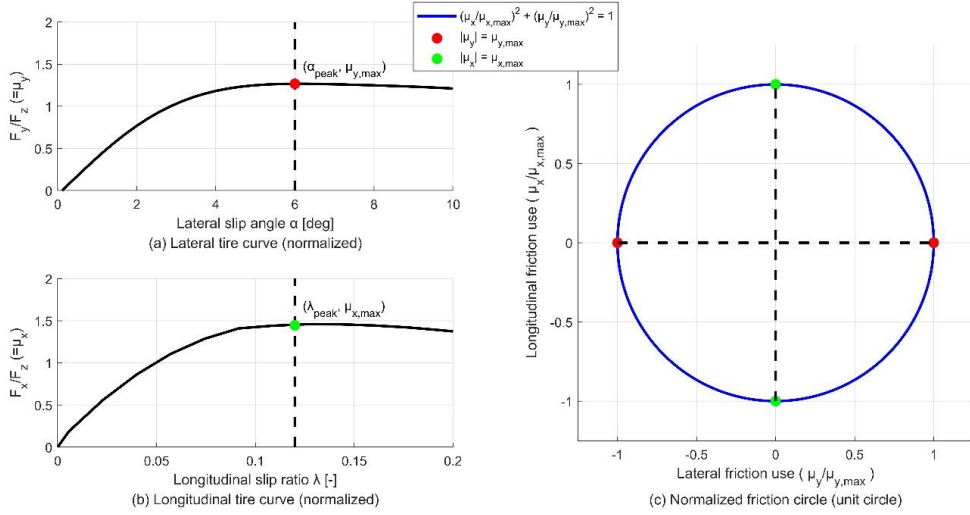


Figure 2.11. Concept of the normlized friction circle.

The normalized friction circle describes the available longitudinal and lateral friction coefficients as ratios to their maximum values for the quantitative representation of the tire friction use in sliding contact. In the normalized friction circle, any point on the edge of the unit circle stands for the maximum tire forces, as shown in Figure 2.11(b). In order to quantify the tire friction use in sliding contact, three indices have been devised as follows:

$$\bar{\mu}_x = \frac{\mu_x}{\mu_{x,max}}, \quad (10a)$$

$$\bar{\mu}_y = \frac{\mu_y}{\mu_{y,max}}, \quad (10b)$$

$$\bar{\mu}_{res} = \sqrt{\bar{\mu}_x^2 + \bar{\mu}_y^2} \quad (10c)$$

where  $\bar{\mu}_x$ ,  $\bar{\mu}_y$ , and  $\bar{\mu}_{res}$  are the longitudinal, lateral and resultant friction use in

sliding contact, respectively. For example,  $|\bar{\mu}_x|=1$  corresponds to the maximum driving and braking tire force, and  $|\bar{\mu}_y|=1$  indicates the maximum cornering tire forces.  $\bar{\mu}_{res}=1$  holds at any point on the edge of the unit circle in Figure 2.11(c).

Based on the proposed approach, the friction ellipse model and tire force measurements in Figure 2.10 can be expressed in a new coordinate system, as shown in Figure 2.12, which shows that the proposed method can be utilized to monitor and longitudinal and lateral friction use in a racing track. By monitoring the friction use, the characteristics in friction use by a professional driver can be analyzed, particularly with respect to the behavior of rear-wheel-drive vehicles in a racing track. The following three indices are considered: 1) lateral friction use  $\bar{\mu}_y$ ; 2) longitudinal friction use  $\bar{\mu}_x$ ; 3) resultant friction use  $\sqrt{\bar{\mu}_x^2 + \bar{\mu}_y^2}$ .

As shown in Figure 2.12, the resultant friction use for the front tires and rear tires is mainly occupied by the lateral friction use. This fact indicates that drivers can directly manipulate the steering angle and control lateral tire forces in the front wheels, though the lateral tire forces in the rear wheels cannot be directly controlled by drivers. Lateral tire forces on the rear wheels cannot be controlled without the help of additionally equipped systems such as rear wheel steering. However, the professional driver can control the longitudinal tire forces of the rear wheels by the throttle pedal inputs. In Figure 2.12(c) and (d), it can be shown that the profession driver strived to fully use the longitudinal tire forces of the rear wheels at the limits of handling.

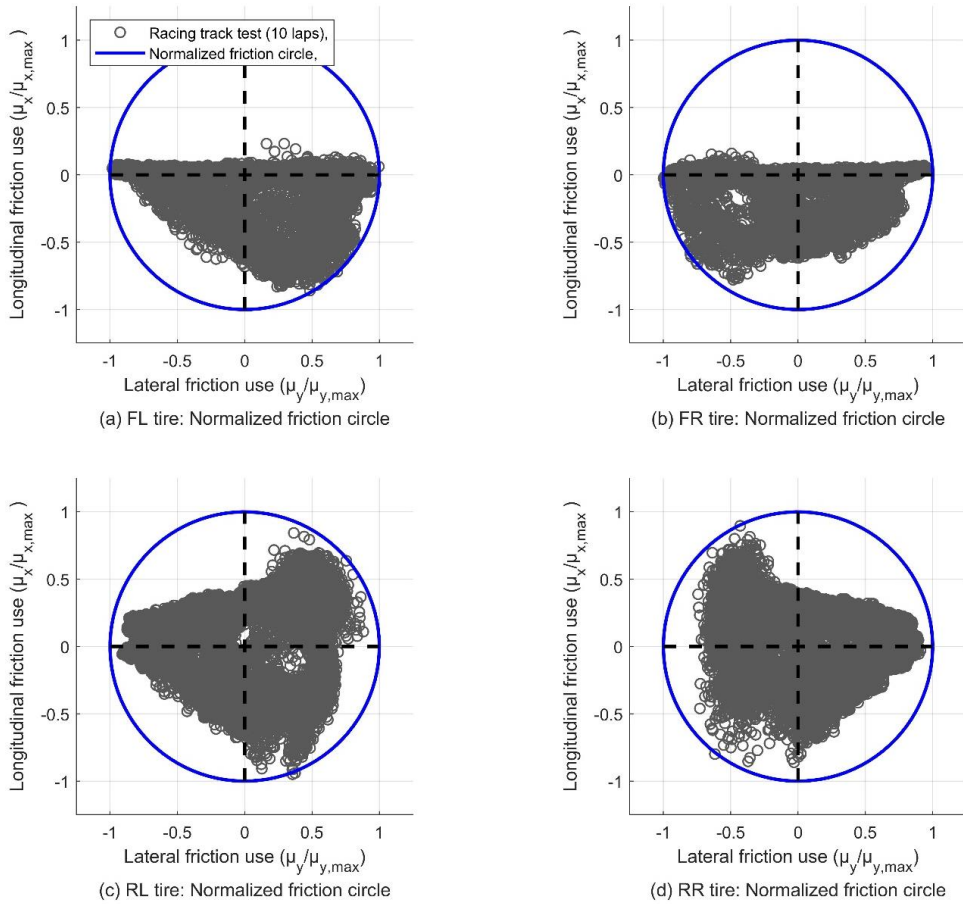


Figure 2.12. Longitudinal and lateral friction use on a racing track by an expert driver.

Additionally, Figure 2.12 shows that manipulation efforts should be made to avoid the tire saturation of the inner tires at high-speed cornering. Since the positive (or negative) values of lateral friction use correspond to the left (or right) turn, the positive values of lateral friction use at front-left and rear-left wheels indicate the friction use of inner wheels at high-speed cornering. As shown in Figure 2.12(b) and (d), the inner wheels are more prone to be saturated due to the load transfer, compared to the outer wheels.

Figure 2.13 shows the scattered plot for the absolute values for the friction use in



each wheel versus the absolute values for the curvature of vehicle path driven by the expert driver. The curvature of the driven paths can be calculated as follows [Kegelman'17]:

$$\kappa = \frac{d\psi}{ds_p} = \frac{d\psi}{dt} \frac{dt}{ds_p} = \frac{\dot{\psi}}{v_x} \quad (11)$$

where  $\kappa$  is the path curvature;  $\psi$  is the angle of vehicle velocity vector;  $s_p$  is the distance along the vehicle path; The highest values for the path curvature correspond to the minimum turning radius, indicating the hair corners. Figure 2.13 shows that the resultant friction uses of the four wheels remain high throughout the entire curvature region. As shown in Figure 2.13(a) and (b), the lateral friction use becomes dominant for the front wheel friction use compared to the longitudinal friction use. Conversely, as shown in Figure 2.13(d), the lateral friction use is prevalent in the rear wheels.

However, as shown in Figure 2.13(c), it should be noted that the friction use of the rear-left wheel that is the inner driven wheel is considerably different from that of the other tires. The longitudinal friction use contributes more towards the resultant value than that of the other three wheels in the region of high path curvature. The result indicate that the driven inner wheel is more prone to saturation, mainly due to the longitudinal friction use. It also shows that expert drivers made attempts to prevent the saturation of the inner driven tire in order to prevent the loss of stability and oversteer in the hairpin corners.

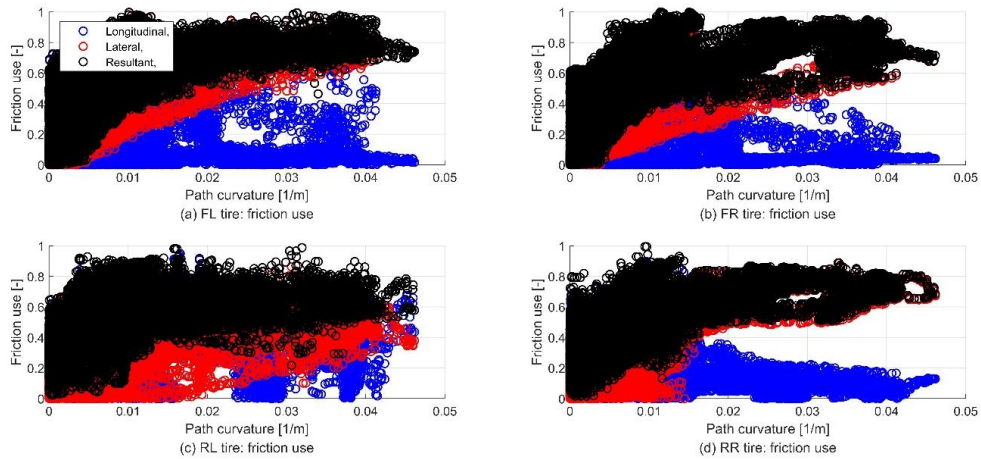


Figure 2.13. Friction use with respect to the curvature of the vehicle trajectory.

In Section 2, an investigation into the high-performance tire characteristics has been conducted based on the data obtained from indoor test rig and vehicle tests. The indoor test data was analyzed using the Magic Formula model with extracting the proper model parameters. Optimization techniques have been adopted to fit the Magic Formula model to the indoor test data with the goal of tire force error minimization. Based on the fitted results, the tire characteristics were explored and discussed.

Additionally, the tire force limits were analyzed based on the data from indoor and vehicle tests. To describe the tire force limits, an optimization-based friction ellipse model has been devised, where optimization techniques were utilized to determine the proper coefficients of the ellipse model. The optimization goal was to find a parameter set that can generate smallest ellipse incorporating all obtained tire force measurements. In order to evaluate the estimation results with vehicle test results, a test vehicle has been developed that allows to measure the vehicle states and tire forces. The driving data of an expert driver on a racing track shows that the

proposed friction ellipse model can better describe the tire force limits compared to the friction circle model with a pre-determined friction coefficient such as 1.0.

Lastly, a normalized friction model was proposed to consider the anisotropic tire force limits based on three indices (i.e., longitudinal, lateral, and resultant friction use). On the other hand, the driving characteristics of a professional driver in a rear-wheel-drive vehicle were investigated using the three indices. The analysis results show that the expert driver attempted to maximally use the tire forces at each wheel throughout the entire curvature region within the path. In particular, two driving characteristics were derived. Firstly, the lateral forces of the front wheels were maximized and sustained near the edge of the tire force limits. Secondly, the tire saturation of the inner driven wheel was avoided in high curvature region such as hairpin corners, since the saturation of the rear tire in high sideslip maneuvers can induce the overall reduction of lap time with the possibility of causing vehicle spinout and reduced lap time.

# Chapter 3 Torque Vectoring Control with Two Front In-Wheel Motors

This section presents the control strategies of the torque vectoring control algorithm using two front in-wheel motors [Cha'22]. As shown in Figure 3.1, the target vehicle architecture is an internal combustion engine (ICE) based rear-wheel drive vehicle with two front in-wheel motors. This section is primarily focused on controlling only the lateral motion of an internal combustion engine (ICE) vehicle by controlling the two additionally equipped front in-wheel motors. The brake and accelerator pedal operated by the driver still acts as the control input for the rear-wheel-drive ICE vehicle in terms of longitudinal motion. In short, longitudinal motion control is not the primary scope of this section.

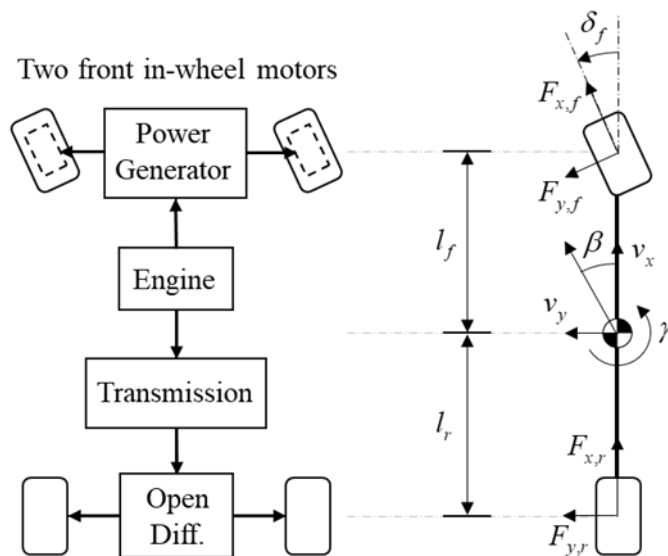


Figure 3.1. Target vehicle architecture and vehicle model.

The proposed torque vectoring algorithm is designed to modify the vehicle

understeer gradient and yaw rate damping coefficient. The understeer gradient is a coefficient that significantly affects the steady-state yaw rate response [Abe'15]. As shown in Figure 3.2(a), one measure of the understeer gradient is the slope of the constant radius skid pad curve [Milliken'95]. The neutral steer vehicle maintains the required steering angle at the Ackermann Steering Angle as the lateral acceleration increases. On the other hand, in understeer (or oversteer) vehicles, the required steering angle increases (or decreases) from the Ackermann angle as the lateral acceleration increases. A normal passenger car, including the vehicle of interest in this study, conforms to the nonlinear understeer characteristics.

The other cornering characteristic to be considered is the yaw rate damping. As shown in Figure 3.2(b), the yaw rate damping coefficient determines the yaw rate overshoot in the transient yaw rate response [Abe'15]. An increased yaw rate damping coefficient can achieve a reduced yaw rate overshoot. However, if the yaw rate damping coefficient becomes too large, the rise time of the yaw rate becomes too low. For this reason, a critically damped response was considered to be desirable in this study. Although the yaw rate damping coefficient cannot be accurately measured and is dependent on driving conditions, the proposed algorithm has been devised to modify the yaw rate damping coefficient based on a closed-loop system model that expresses the yaw rate response for steering angle input.

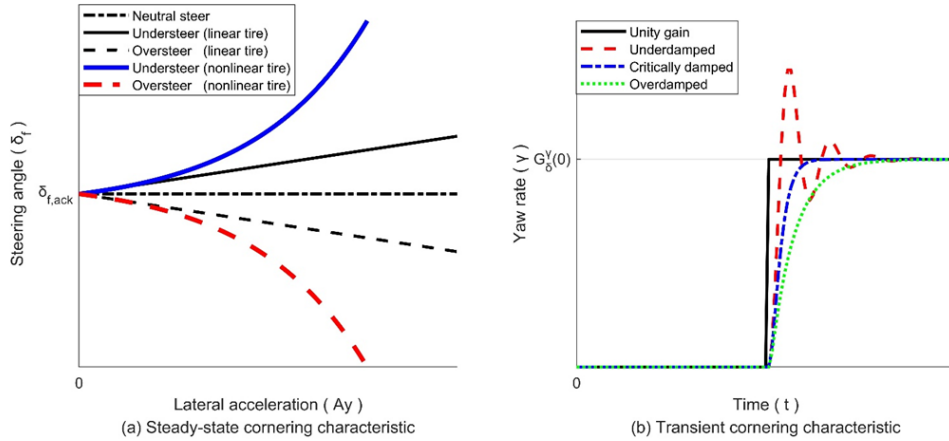


Figure 3.2. Concepts of the two cornering characteristics.

The overall block diagram of the in-wheel motor control algorithm is illustrated in Figure 3.3. The control algorithm consists of steady-state and transient control inputs [Vignati'16, Canale'08, Yang'18, Park'20]. The two control inputs each have their own purpose. Firstly, the purpose of the steady-state control input is to increase the steady-state yaw gain of a vehicle by decreasing the understeer gradient. Secondly, the purpose of the transient control input is to decrease the yaw rate overshoot by increasing the yaw rate damping coefficient. By integrating the steady-state and transient control inputs, the desired yaw moment can be calculated. The desired yaw moment is then converted into the desired in-wheel motor torque inputs. The desired torque inputs are constrained according to the in-wheel motor T-N (torque-rpm) curve used as a lookup table that receives the wheel speed at each wheel as inputs to obtain the motor torque limits. Additionally, the estimators for cornering stiffness and vehicle states are designed to implement the proposed algorithm in both simulations and vehicle tests.

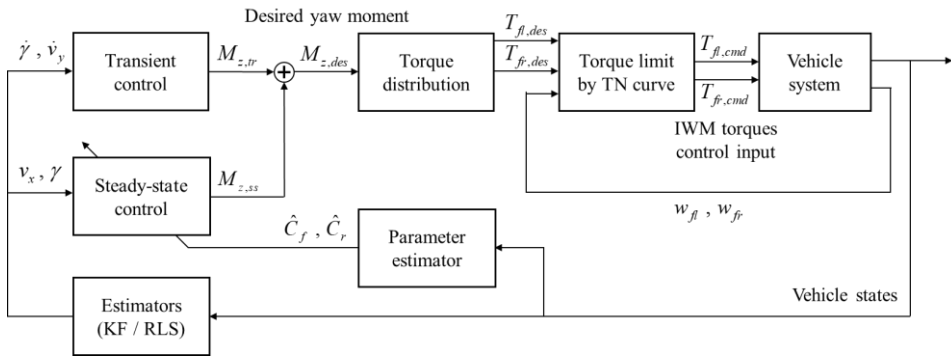


Figure 3.3. Block diagram of the proposed in-wheel motor control algorithm.

### 3.1. Upper level controller

Since the longitudinal motion control is not the primary scope of this study, a bicycle model (single-track model) [Rajamni'11] is adopted for design simplicity and is sufficient in describing the lateral motion of the vehicle as a linear system. In the bicycle model, the direct yaw moment can be described as an additional single control input, and lateral vehicle dynamics can be simplified as a state-space form [Rajamani'11]. Based on the bicycle model, the lateral dynamics can be described as follows:

$$mv_x \left( \frac{d\beta}{dt} + \gamma \right) = F_f^y \cos \delta_f + F_r^y, \quad (12a)$$

$$I_z \frac{d\gamma}{dt} = l_f F_f^y \cos \delta_f - l_r F_r^y + M_z, \quad (12b)$$

Under the assumption that tire slip angles are small, the lateral tire force and tire slip angle can be taken to be approximately linear, as follows [Pacejka'05]:

$$F_f^y = 2C_f \left( \delta_f - \beta - \frac{l_f \gamma}{v_x} \right), \quad (13a)$$

$$F_r^y = 2C_r \left( -\beta + \frac{l_r \gamma}{v_x} \right), \quad (13b)$$

Based on Equations (12a)-(13b) and the small steering angle approximation (i.e.,  $\cos \delta_f \approx 1$ ), vehicle lateral dynamics can be presented in the form of a state-space equation as follows:



$$\begin{aligned}\frac{dx(t)}{dt} &= Ax(t) + Bu(t) \\ &= Ax(t) + B_{\delta_f} \delta_f(t) + B_{M_z} M_z(t),\end{aligned}$$

where  $x = [\beta, \gamma]^T$ ,  $u = [\delta_f, M_z]^T$ ,

$$\begin{aligned}A &= \begin{bmatrix} -\frac{2(C_f + C_r)}{mv_x} & -\frac{2(C_f l_f - C_r l_r)}{mv_x^2} - 1 \\ -\frac{2(C_f l_f - C_r l_r)}{I_z} & -\frac{2(C_f l_f^2 + C_r l_r^2)}{I_z v_x} \end{bmatrix}, \\ B &= \begin{bmatrix} \frac{2C_f}{mv_x} & 0 \\ \frac{2l_f C_f}{I_z} & \frac{1}{I_z} \end{bmatrix}, \quad B_{\delta_f} = \begin{bmatrix} \frac{2C_f}{mv_x} \\ \frac{2l_f C_f}{I_z} \end{bmatrix}, \quad B_{M_z} = \begin{bmatrix} 0 \\ \frac{1}{I_z} \end{bmatrix},\end{aligned}\tag{14}$$

where the steering angle  $\delta_f$  is the driver input and the yaw moment  $M_z$  is the additional control input to be generated by the two front in-wheel motors.

### 3.1.1. Control strategies for steady-state response

As aforementioned, the purpose of the steady-state control input is to increase the steady-state yaw gain by modifying the vehicle understeer gradient. The steady-state control input is designed based on the steady-state assumption in the bicycle model. By applying the steady-state assumption (i.e.,  $d\beta/dt = d\gamma/dt = 0$ ) to the bicycle model, the bicycle model can be reformulated to express the steady-state cornering as follows:

$$0 = \begin{bmatrix} a_{11} & a_{12} \\ a_{21} & a_{22} \end{bmatrix} \cdot \begin{bmatrix} \beta \\ \gamma \end{bmatrix} + \begin{bmatrix} b_{11} \\ b_{21} \end{bmatrix} \cdot \delta_f + \begin{bmatrix} b_{12} \\ b_{22} \end{bmatrix} \cdot M_z,\tag{15}$$

where  $a_{ij}$  and  $b_{ij}$  are the elements in the  $i$ th row and  $j$ th column of 2-by-2 matrices A and B in Equation (14), respectively. Equation (15) can be rearranged including the understeer gradient in order to describe the steady-state yaw rate

response as follows:

$$\gamma_{ss} = \frac{v_x}{L + K_{us}v_x^2} \delta_f + \frac{C_f + C_r}{2C_f C_r L} \cdot \frac{v_x}{L + K_{us}v_x^2} M_z, \quad K_{us} = \frac{m(C_r l_r - C_f l_f)}{2C_f C_r L}, \quad (16)$$

In order to design the yaw moment  $M_z$  for the modification of vehicle understeer gradient, a steady-state response with a variation of understeer gradient  $\Delta K_{us,IWM}$  by in-wheel motor control can be described as follows:

$$\gamma_{ss,des} = \frac{v_x}{L + K_{us,des}v_x^2} \delta_f = \frac{v_x}{L + (K_{us} + \Delta K_{us,IWM})v_x^2} \delta_f \quad (17)$$

where  $\gamma_{ss,des}$  and  $K_{us,des}$  are the desired steady-state yaw rate response and desired understeer gradient, respectively.

From Equations (16) and (17), the steady-state yaw moment control input  $M_{z,ss}$  can be derived as follows:

$$\begin{aligned} M_{z,ss} &= \frac{2\hat{C}_f \hat{C}_r L}{\hat{C}_f + \hat{C}_r} \cdot (K_{us} - K_{us,des}) \cdot v_x \gamma \\ &= \frac{2\hat{C}_f \hat{C}_r L}{\hat{C}_f + \hat{C}_r} \cdot \Delta K_{us,IWM} \cdot v_x \gamma \end{aligned} \quad (18)$$

where  $\hat{C}_f$  and  $\hat{C}_r$  are the estimated cornering stiffness of front and rear tires, respectively. The target variation in the understeer gradient by in-wheel motor control  $\Delta K_{us,IWM}$  is determined based on a nonlinear static map that uses the steering angle and vehicle speed as input variables [Goggia'14, Cha'22]. In particular, it should be noted that the measured lateral acceleration is affected by the gravity component  $g \cdot \sin(\phi_{bank} + \phi_{roll})$  of the road bank angle and roll angle [Kim'12]. For this reason, in the steady-state control input, the lateral acceleration  $a_y$  is replaced by the product of the vehicle speed and yaw rate in order to remove any effect of the gravity component.

Additionally, the cornering stiffness of front and rear tires (i.e.,  $\hat{C}_f$  and  $\hat{C}_r$ ) are estimated by means of the recursive least square method with exponential forgetting factor based on the bicycle model as follows [Cha'22, Joa'20]:

$$\begin{aligned}
F_{y,i} &= C_i \alpha_i, \quad i = f, r \\
C_i(k) &= C_i(k-1) + K_i(k) \cdot [F_{y,i}(k) - C_i(k-1) \alpha_i(k)] \\
K_i(k) &= P_i(k-1) \alpha_i(k) / [\lambda_i + P_i(k-1) \alpha_i^2(k)] \\
P_i(k) &= [1 - K_i(k) \alpha_i(k)] \cdot P_i(k-1) / \lambda_i
\end{aligned} \tag{19}$$

The two forgetting factors were both set to 0.7 (i.e.,  $\lambda_f = \lambda_r = 0.7$ ). The lateral tire forces and slip angles in Equation (19) are calculated based on the following equations:

$$\begin{aligned}
F_{y,f} &= \frac{l_r m}{L} \cdot a_y(k) + \frac{I_z}{L} \cdot \frac{d\gamma}{dt}(k), & F_{y,r} &= \frac{l_f m}{L} \cdot a_y(k) - \frac{I_z}{L} \cdot \frac{d\gamma}{dt}(k) \\
\alpha_f(k) &= \delta_f(k) - \frac{v_y(k) + l_f \gamma(k)}{v_x(k)}, & \alpha_r(k) &= -\frac{v_y(k) - l_r \gamma(k)}{v_x(k)}
\end{aligned} \tag{20}$$

The vehicle states in the above equations were measured using onboard sensors and the Differential Global Position System (DGPS) in the test vehicle. The yaw acceleration  $d\gamma/dt$  is estimated using a Kalman filter with the first-order Taylor formula as follows [Joa'19]:

$$\begin{aligned}
x(k+1) &= A_d x(k), \\
z(k+1) &= H_d x(k+1), \\
\text{where } x(k) &= \left[ \gamma(k), \frac{d\gamma}{dt}(k), \frac{d^2\gamma}{dt^2}(k) \right]^T, \quad z(k+1) = \gamma(k), \\
A_d &= \begin{bmatrix} 1 & \Delta t & \Delta t^2 / 2 \\ 0 & 1 & \Delta t \\ 0 & 0 & 1 \end{bmatrix}, \quad H_d = [1 \ 0 \ 0],
\end{aligned} \tag{21}$$

where  $\Delta t$  is a sampling time with fixed step size. The process and measurement noise variance matrix is defined as  $Q = \text{diag}([0.5 \ 3 \ 30])$  and  $R = 0.1$ ,

respectively. Based on the aforementioned model, the discrete Kalman filter is implemented for yaw rate acceleration estimation [Brown'97].

### 3.1.2. Control strategies for transient response

The transient control input is devised to decrease the yaw rate overshoot by modifying the yaw rate damping coefficient. The bicycle model can be expressed in two equations as follows:

$$\frac{d\beta}{dt} = a_{11}\beta + a_{12}\gamma + b_{11}\delta_f + b_{12}M_z, \quad (22a)$$

$$\frac{d\gamma}{dt} = a_{21}\beta + a_{22}\gamma + b_{21}\delta_f + b_{22}M_z, \quad (22b)$$

where  $a_{ij}$ ,  $b_{ij}$  ( $i, j = 1, 2$ ) are the elements of matrices A and B in Equation (14), respectively;  $b_{12}$  is equal to zero. The lateral acceleration  $a_y$  can be expressed in terms of the acceleration along with the vehicle latera axis and centripetal acceleration as follows [Rajamani'11]:

$$a_y = v_x \cdot \left( \frac{d\beta}{dt} + \gamma \right), \quad (23)$$

By substituting Equation (22a) into Equation (23), the following expression for lateral motion can be obtained as follows:

$$\frac{a_y}{v_x} = -\frac{2(C_f + C_r)}{mv_x} \cdot \beta - \frac{2(C_f l_f - C_r l_r)}{mv_x^2} \cdot \gamma + \frac{2C_f}{mv_x} \cdot \delta_f \quad (24)$$

Applying the Laplace Transform on Equation (24) and yaw rate dynamics (22b) and integrating the two transformed equations, the vehicle lateral motion can be described in the s-domain as follows:

$$\gamma_{tr}(s) = \frac{1}{\tau s + 1} \cdot \frac{v_x}{L} \left[ 1 - K_{us} \cdot a_y(s) + \frac{L}{I_z v_x} \tau \cdot M_z(s) \right], \quad \tau = \frac{I_z v_x (C_f + C_r)}{2C_f C_r L^2}, \quad (25)$$

where  $\tau$  is a parameter that affects the transient yaw rate response with lateral

acceleration and yaw moment control input, which can be regarded as the time constant of a first order delay;  $\gamma_{tr}$  is the transient yaw rate response.

The yaw rate response tuning parameter  $\eta$  is newly introduced in order to express the modified transient yaw rate response with the modified time constant  $\eta\tau$  and the steady-state control input  $M_{z,ss}$  as following equation:

$$\gamma_{tr,mod}(s) = \frac{1}{\eta\tau \cdot s + 1} \cdot \frac{v_x}{L} \left[ 1 - K_{us} \cdot a_y(s) + \frac{L}{I_z v_x} \tau \cdot M_{z,ss}(s) \right], \quad (26)$$

where  $\gamma_{tr,mod}$  is the modified transient yaw rate response, which is the objective transient response for in-wheel motor. Equations (25) and (26) can be arranged as Equations (27) and (28), respectively, as follows:

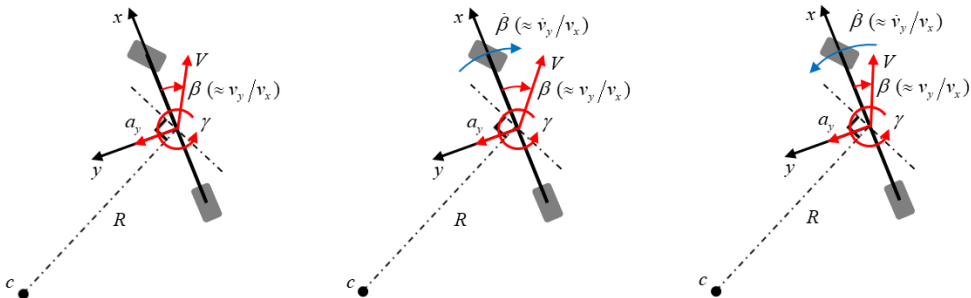
$$\tau [s \cdot \gamma(s) - M_z(s) / I_z] = \frac{v_x}{L} [1 - K_{us} a_y] - \gamma(s), \quad (27)$$

$$\tau [\eta s \cdot \gamma(s) - M_{z,ss}(s) / I_z] = \frac{v_x}{L} [1 - K_{us} a_y] - \gamma(s), \quad (28)$$

By dividing Equation (27) by Equation (28), the time constant  $\tau$  can be eliminated, and the following equation can be obtained:

$$M_z(s) = M_{z,ss}(s) + I_z(1 - \eta) \cdot s\gamma(s), \quad (29)$$

Additionally, in order to reduce the vehicle oversteering and understeering behavior [Vignati'16], a feedback gain  $k$  for the lateral velocity rate is added, increasing the yaw rate damping coefficient, which will be specifically explained later.



(a) Steady-state

(b) Oversteering

(c) Understeering

Figure 3.4. Vehicle cornering conditions.

Figure 3.4 describes three cornering conditions: (a) steady-state condition; (b) oversteering condition; (c) understeering condition. Since the magnitude of the lateral velocity rate increases under the oversteering and understeering conditions, as shown in Figure 3.4(b) and (c), feedback control for the lateral velocity rate can prevent the vehicle from spinning by assisting the vehicle behavior such that the vehicle behavior is maintained in a steady-state cornering condition as described in Figure 3.4(a) [Vignati'16, Joa'20]. With this concept, the desired yaw moment control input can be expressed in the time domain as follows:

$$M_{z,IWM} = M_{z,ss} + M_{z,tr}, \quad (30a)$$

$$M_{z,ss} = \frac{2\hat{C}_f\hat{C}_r}{\hat{C}_f + \hat{C}_r} \cdot \Delta K_{us,IWM} \cdot v_x \gamma, \quad (30b)$$

$$M_{z,tr} = I_z(1-\eta) \cdot \frac{d\gamma}{dt} + k \cdot \frac{dv_y}{dt}, \quad (30c)$$

where  $M_{z,ss}$  is the steady-state control input;  $M_{z,tr}$  is the transient control input;  $M_{z,IWM}$  is the desired yaw moment by in-wheel motor control and is equivalent to the sum of the steady-state and transient control inputs. For steady-state yaw rate response, only steady-state control input modifies vehicle understeer gradient. For the transient yaw rate response, steady-state and transient control inputs modify the yaw rate damping coefficient through the three tuning parameters: 1) target variation in the understeer gradient  $\Delta K_{us,IWM}$ ; 2) feedback gain  $k$ ; 3) yaw rate response tuning parameter  $\eta$ ; The parametric study for the three tuning parameters will be introduced in the next subsection.

Additionally, the cornering stiffnesses of front and rear axles (i.e.,  $\hat{C}_f$  and  $\hat{C}_r$ ) in the steady-state control input are estimated considering the transient cornering response by means of the recursive least square method based on the following equations [Joa'20, Ljung'99]:

$$\begin{aligned}
F_{y,i} &= C_i \alpha_i, \quad i = f, r \\
C_i(k) &= C_i(k-1) + K_i(k) \cdot [F_{y,i}(k) - C_i(k-1) \alpha_i(k)], \\
K_i(k) &= P_i(k-1) \alpha_i(k) / [\lambda_i + P_i(k-1) \alpha_i^2(k)], \\
P_i(k) &= [1 - K_i(k) \alpha_i(k)] \cdot P_i(k-1) / \lambda_i,
\end{aligned} \tag{31}$$

The value of forgetting factor  $\lambda$  is set as 0.7. The lateral tire forces and tire slip angle in the above equation are calculated using the bicycle model based on the following equations:

$$F_{y,f} = \frac{l_r m}{L} a_y + \frac{I_z}{L} \frac{d\gamma}{dt}, \quad F_{y,r} = \frac{l_f m}{L} a_y - \frac{I_z}{L} \frac{d\gamma}{dt}, \tag{32a}$$

$$\alpha_f = \delta_f - \frac{v_y + l_f \gamma}{v_x}, \quad \alpha_r = -\frac{v_y - l_r \gamma}{v_x} \tag{32b}$$

The yaw acceleration  $d\gamma/dt$  in the above equations are esimated by means of a Kalman filter using the first-order Taylor formula as follows [Brown'97]:

$$\begin{aligned}
x(k+1) &= A_d x(k), \\
z(k+1) &= H_d x(k+1), \\
\text{where } x(k) &= \left[ \gamma(k), \frac{d\gamma}{dt}(k), \frac{d^2\gamma}{dt^2}(k) \right]^T, \quad z(k+1) = \gamma(k+1), \\
A_d &= \begin{bmatrix} 1 & \Delta t & \Delta t^2 / 2 \\ 0 & 1 & \Delta t \\ 0 & 0 & 1 \end{bmatrix}, \quad H_d = [1 \ 0 \ 0],
\end{aligned} \tag{33}$$

where  $\Delta t$  is a fixed step size sampling time. The process and measurement noise covariance matrix is set as  $Q = \text{diag}([0.5 \ 3 \ 30])$  and  $R = 0.1$ , respectively.

### 3.1.3. Analysis on the closed-loop system with proposed controller

This subsection describes the analysis on the closed-loop system with proposed controller, in order to reveal the effects of each design parameter in proposed control law. This analysis was conducted in Laplace domain using the bicycle model. In particular, the vehicle dynamic response to the variations of the three parameters (i.e.,  $\Delta K_{us}$ ,  $\eta$  and  $k$ ) were analyzed. Based on the analysis on the closed-loop system response, the appropriate values of the three design parameters were adopted in the proposed algorithm.

In order to analyze the steady-state and transient responses of the closed-loop system, the bicycle model of Equation (22) and yaw moment control law (30) were reformulated in Laplace domain to analyze the transfer function that describes the yaw rate output for steering angle input. The second-order transfer function with proposed control can be calculated as follows:

$$\frac{\gamma}{\delta_f}(s) = \frac{w_n^2}{s^2 + 2\zeta w_n s + w_n^2} \cdot (T_r s + 1) \cdot G_\delta^\gamma(0), \quad (34)$$

where  $G_\delta^\gamma(0)$  is the steady-state yaw gain;  $T_r$  is the time constant of the closed-loop zero. The model parameters in Equation (34) can be calculated as follows:

$$G_\delta^\gamma(0) = \frac{v_x}{L + (K_{us} + \Delta K_{us})v_x^2}, \quad (35a)$$

$$w_n = \sqrt{\frac{1}{\eta} \left( a_{11}a_{22} - a_{21}a_{12} - \frac{v_x}{I_z} \cdot \frac{2C_f C_r L}{C_f + C_r} \Delta K_{us} a_{11} \right)}, \quad (35b)$$

$$\zeta = \frac{\frac{1}{\eta} \left[ -a_{22} - \eta a_{11} + \frac{v_x}{I_z} \cdot \frac{2C_f C_r L}{C_f + C_r} \Delta K_{us} \cdot (a_{12} + 1) - \frac{v_x}{I_z} k \cdot a_{12} \right]}{2 \sqrt{\frac{1}{\eta} \left( a_{11}a_{22} - a_{21}a_{12} - \frac{v_x}{I_z} \cdot \frac{2C_f C_r L}{C_f + C_r} \Delta K_{us} a_{11} \right)}}, \quad (35c)$$



$$T_r = \frac{b_{21} + \frac{v_x}{I_z} \left( -\frac{2C_f C_r L}{C_f + C_r} \Delta K_{us} + k \right) b_{11}}{a_{21} b_{11} - a_{11} b_{21}}, \quad (35d)$$

where  $a_{ij}$  and  $b_{ij}$  are the elements in the  $i$ th row and  $j$ th column of 2-by-2 matrices A and B in Equation (14), respectively.

As shown in Equations (35a)-(35d), the three design parameters (i.e.,  $\Delta K_{us}$ ,  $\eta$  and  $k$ ) affects the three model parameters (i.e.,  $G_\delta^y(0)$ ,  $\zeta$  and  $T_r$ ) of the closed-loop system. Firstly, the steady-state yaw gain is affected by the understeer gradient variation. Secondly, the yaw rate damping coefficient varies with all three design parameters. Thirdly, the time constant of the closed-loop zero is influenced by the understeer gradient variation and feedback gain. Based on the aforementioned analysis, the proper values of the three design parameters can be determined. Using the target vehicle parameters and Equation (35), the effects of the three parameters on the vehicle response are illustrated in Figure 3.5.

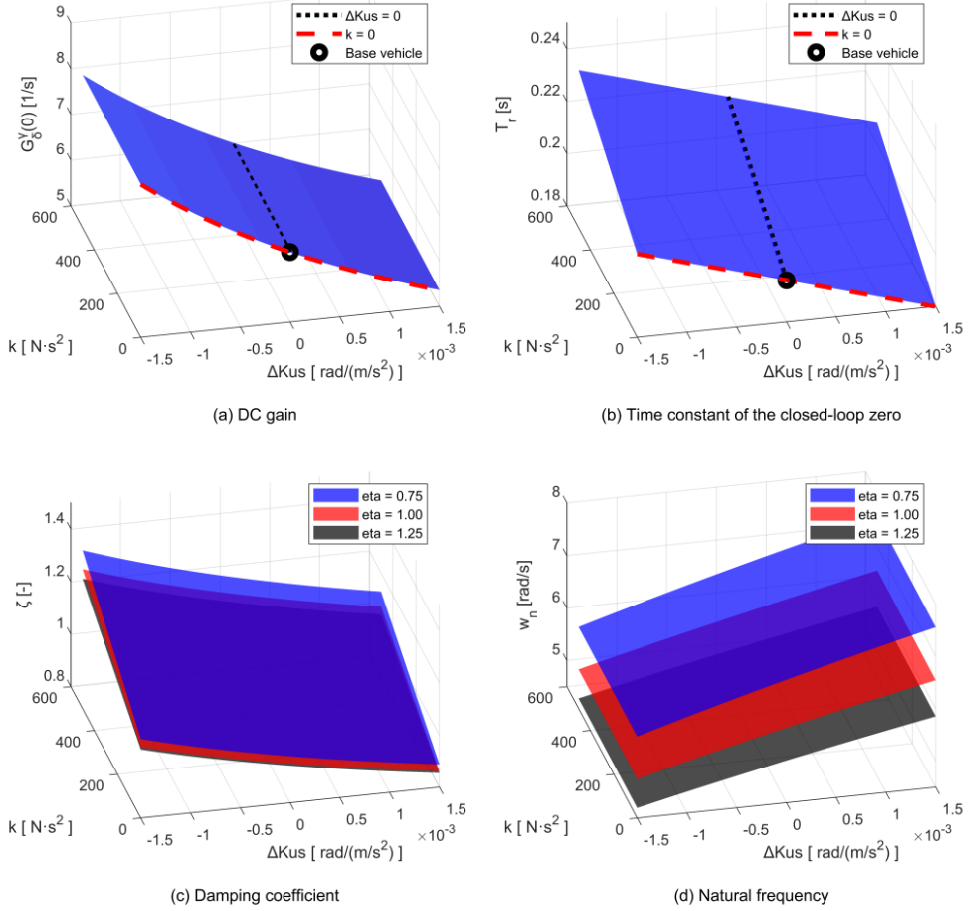


Figure 3.5. The effects of three design parameters in proposed control law.

As shown in Figure 3.5 and Equations (35a)-(35d), by properly choosing the values of the three design parameters, the steady-state and transient yaw rate responses can be modified, achieving the control objective of the proposed methodologies. For example, selecting a negative value for understeer gradient variation  $\Delta K_{us}$  is desirable for increasing the steady-state yaw gain and yaw rate damping coefficient. Additionally, selecting proper value of feedback gain  $k$  can also increase the yaw rate damping coefficient  $\zeta$  without affecting the steady-state yaw gain  $G_s^\gamma(0)$ . Lastly, the yaw rate response tuning parameter  $\eta$  can also

increase the yaw rate damping coefficient.

One thing to be noted is that the effects of three design parameters on the closed-loop response show a similar characteristics with little regard to variations in vehicle speed and cornering stiffness. In short, even if the vehicle speed and cornering stiffness are varied, the steady-state and transient yaw rate response can be improved using the proposed controller. The parameter selection process consists of the four steps shown below:

Step 1) Determining the proper value of  $\Delta K_{us}$  to reduce the vehicle understeer gradient within the maximum torque range of the in-wheel motor. An adequate range for this parameter was set between 0 and  $-0.1 \times 10^{-2}$ ;

Step 2) Determining the proper value of  $\Delta \zeta$  to increase the yaw rate damping coefficient. An adequate range for this parameter was determined to be between 0 and 0.3;

Step 3) Scheduling the gain  $k$  based on the pre-determined  $\Delta K_{us}$  and  $\Delta \zeta$ . The gain was scheduled based on the analysis results given in Equation (35) and Figure 3.5 under the assumption of nominal cornering stiffnesses and  $\eta = 1$ .

Step 4) Tuning the design parameter  $\eta$  manually to generate a satisfactory transient response. An adequate range for this parameter was between 0.75 and 1.00;

## 3.2. Lower level controller

The role of the lower level controller is to convert the desired yaw moment from the upper level controller to the two front in-wheel motor torque inputs. The two motor torque inputs are determined in order to generate the desired yaw moment considering the actuator characteristics of in-wheel motors and tire friction limits.

### 3.2.1. Actuator characteristics of in-wheel motors

As aforementioned, the in-wheel motors can directly and independently control torque of each wheel. Since in-wheel motors can precisely generate a fast response and the capability of forward and reverse torque generation [Murata'12, Watts'10], the errors and delays in torque generation are negligible in controller design.

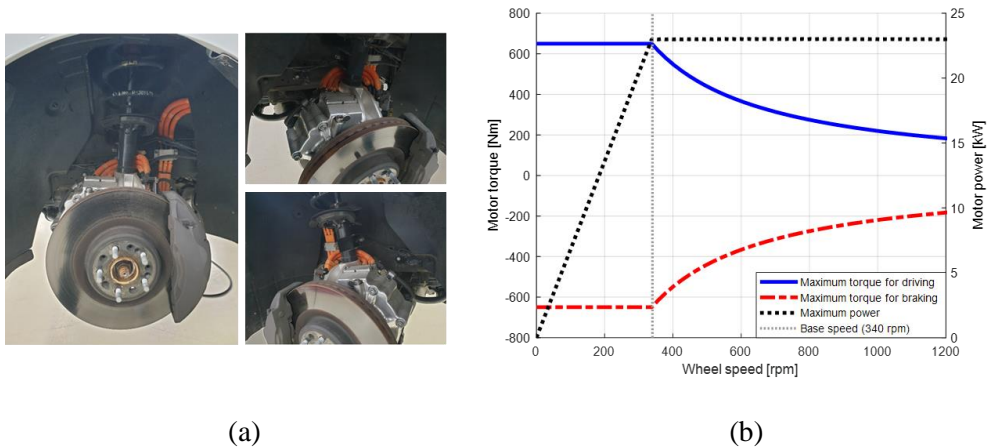


Figure 3.6. (a) Two front in-wheel motors equipped in test vehicle and (b) In-wheel motor T-N curve.

As shown in Figure 3.6(a), the two in-wheel motors can be installed in the wheel hubs of the test vehicle. Since the motor type of the two front in-wheel motors is the permanent magnet synchronous motor (PMSM), the range of allowable torque

output is determined by the wheel speed, as shown in Figure 3.6(b). When the wheel speed is lower (or higher) than the base speed, the motor torque (or power) remains constant. The actuator specifications can be specified in Table 3.1.

Table 3.1. Actuator specifications.

Two front IWMs	Symbol	Value	Unit
Maximum torque	$T_{IWM,max}$	650	Nm
Maximum power	$P_{IWM,max}$	23	kW
Base speed	$w_{base}$	340	rpm
Maximum speed	$w_{IWM,max}$	1610	rpm

### 3.2.2. Torque inputs for yaw moment generation

The desired yaw moment from the upper-level controller is converted to the two front in-wheel motor torque inputs. The basic torque inputs are determined based on the following equations [Fujimoto'05, Nam'12, Cha'22]:

$$M_{z,des} = \frac{t_{wf}}{2} (F_{x,fr} - F_{x,fl}), \quad (36a)$$

$$F_{x,fl} + F_{x,fr} = 0, \quad T_{fl} = r_{eff} F_{x,fl}, \quad T_{fr} = r_{eff} F_{x,fr}, \quad (36b)$$

$$T_{fl,des} = -\frac{r_{eff}}{t_{wf}} M_{z,des}, \quad T_{fr,des} = \frac{r_{eff}}{t_{wf}} M_{z,des} \quad (36c)$$

where  $T_{fl,des}$  and  $T_{fr,des}$  are the desired motor torque inputs for front left and front right wheels, respectively. Equation (36b) shows that the two front in-wheel motors are controlled only for the lateral motion and not the longitudinal motion, since the main scope of this study is to control lateral motion using all of the available torque outputs. Based on Equations (36a) and (36b), the desired motor torques can be obtained as Equation (36c).

In order to prevent the actuator failure and tire saturation at each wheel, actuator

and friction limit have to be considered in the lower-level controller. The tire friction limits at each wheel are defined using the friction circle model [Pacejka'05]. The actuator and tire friction limits can be described as follows:

$$T_{fl,max} = \begin{cases} T_{IWM,max} & \text{if } w_{fl} \leq w_{base} \\ \frac{P_{IWM,max}}{w_{fl}} & \text{else} \end{cases}, \quad T_{fr,max} = \begin{cases} T_{IWM,max} & \text{if } w_{fr} \leq w_{base} \\ \frac{P_{IWM,max}}{w_{fr}} & \text{else} \end{cases}, \quad (37a)$$

$$\hat{F}_{x,max,i} = \sqrt{(\mu \hat{F}_{z,i})^2 - \hat{F}_{y,i}^2}, \quad (37b)$$

where  $T_{fl,max}$  and  $T_{fr,max}$  are the maximum motor torque output at front left and front right wheel, respectively;  $T_{IWM,max}$  is the maximum motor torque in the torque constant region;  $P_{IWM,max}$  is the maximum motor power in the power constant region;  $w_{base}$  is the base speed that is the boundary speed between the torque and power constant region;  $\hat{F}_{x,max,i}$  is the longitudinal tire force limits at  $i$  th wheel.

Base on Equations (37a) and (37b), the torque commands for the two in-wheel motors can be described as follows:

$$\begin{aligned} T_{fl,cmd} &= \max(-T_{f,max}, T_{fl,des}), \\ T_{fr,cmd} &= \min(T_{f,max}, T_{fr,des}), \end{aligned} \quad \text{if } M_{z,des} \geq 0 \quad (38a)$$

$$\begin{aligned} T_{fl,cmd} &= \min(T_{f,max}, T_{fl,des}), \\ T_{fr,cmd} &= \max(-T_{f,max}, T_{fr,des}), \end{aligned} \quad \text{else } M_{z,des} < 0 \quad (38b)$$

$$T_{f,max} = \min(T_{fl,max}, T_{fr,max}, r_{eff} \hat{F}_{x,max,fl}, r_{eff} \hat{F}_{x,max,fr}), \quad (38c)$$

where  $T_{fl,cmd}$  and  $T_{fr,cmd}$  are the torque commands for front left and front right wheel, respectively;  $T_{f,max}$  is the maximum torque limit for the two motor, which are devised to saturate the motor torque inputs with guaranteeing the condition (36b), i.e.,  $F_{x,fl} + F_{x,fr} = 0$ .

# Chapter 4 Integrated Control of Two Front In-Wheel Motors (IWM) and Rear-Axle Electronic Limited Slip Differential (eLSD)

In this section, an approach for the integrated control of in-wheel motors (IWMs) and electronic limited slip differential (eLSD). However, two torque vectoring devices pose potential risks for their use in lateral motion control. For example, IWM actuators can cause chattering problems for yaw rate feedback control, since IWM actuators directly control the wheel torques and yaw moment [Chae'19, Nam'15, Nam'12]. And the eLSD clutch can only transfer wheel torque from the faster wheel to the slower wheel [Rubin'15, Piyabongkarn'10, Piyabongkarn'07, Hancock'07]. However, by integrating the two devices, the potential risk of each torque vectoring system can be complemented. Considering the characteristics of each actuator, the in-wheel motors can be used for feedforward control to prevent the chattering problem and the eLSD is utilized for feedback control to improve the robustness of the overall algorithm.

As aforementioned, an integrated control of IWMs and eLSD has been devised to improve the handling performance in consideration of the characteristics of each actuator. The objective of the integrated control algorithm is to improve the lateral stability preventing the vehicle spinout at the limits of handling. The integrated control algorithm consists of upper-level and lower-level controllers. The upper-level controller determines the desired yaw moments for IWM and eLSD, and the lower-level controller calculates the torque commands for IWM and eLSD to generate the desired yaw moments. The desired yaw moments for IWM for eLSD

are designed for a feedforward control and a feedback control, respectively, to achieve a yaw rate reference.

As shown in Figure 4.1, the integrated control of IWMs and eLSD consists of four parts in detail: 1) supervisor; 2) upper-level controller; 3) lower-level controller. Firstly, the target understeer gradient and target yaw rate are determined by the supervisor. Secondly, the upper-level controller calculates the desired yaw moments for IWMs and eLSD to track the target yaw rate. Thirdly, the torque inputs for IWM and eLSD are determined considering the actuator characteristics and tire saturation. The tire friction limits are estimated based on the tire model and friction circle model to prevent tire saturation with limiting the torque inputs. The performance of the proposed algorithm has been investigated via both simulations and vehicle tests. The performance of the integrated control was compared with those of individual control and uncontrolled case in computer simulations. The vehicle tests has been performing using a rear wheel drive vehicle equipped with two front IWMs and eLSD. Additionally, the vehicle test was conducted on a racing track to confirm that the proposed algorithm can enhance the lateral stability near the limits of handling.

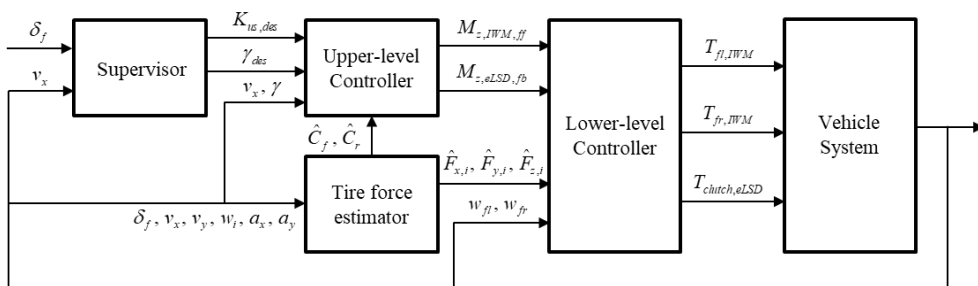


Figure 4.1. Block diagram for the integrated control of in-wheel motor and electronic limited slip differential.



The overall control strategies of the integrated controller are summarized in Figure 4.2. In a normal driving conditions where tire saturation does not occur, the in-wheel motor is used for a feedforward control to generate the target yaw rate, and eLSD is controlled to generate understeering effects [Piyabongkarn'06, Piyabongkarn'07]. When the yaw rate is lower than the target yaw rate, the eLSD is not engaged and operates as an open differential, since eLSD locking in this condition can interrupt the target motion generation [Gadola'18, Cha'21]. Near the limits of handling where tire saturation can occur, the in-wheel motor torque inputs are saturated based on the friction circle model [Pacejka'92]. In particular, it should be noted that the eLSD clutch should be opened when the rear inner wheel is saturated, since eLSD locking in this situation can induce the vehicle spinout.

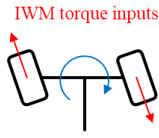
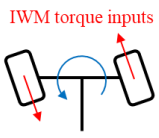
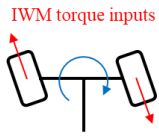
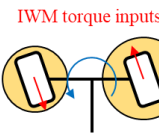
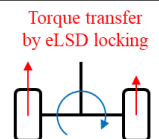
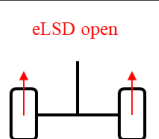
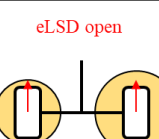
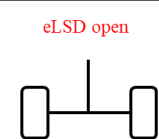
Actuators	Without tire saturation		With tire saturation	
	Oversteer ( $\gamma > \gamma_{des}$ )	Understeer ( $\gamma < \gamma_{des}$ )	Oversteer (rear tire saturation)	Understeer (front tire saturation)
Front IWMs	<p>IWM torque inputs</p>  <p>Understeering effect</p>	<p>IWM torque inputs</p>  <p>Oversteering effect</p>	<p>IWM torque inputs</p>  <p>Understeering effect</p>	<p>IWM torque inputs</p>  <p>Oversteering effect</p>
Rear eLSD	<p>Torque transfer by eLSD locking</p>  <p>Understeering effect</p>	<p>eLSD open</p>  <p>Understeering effect if locked</p>	<p>eLSD open</p>  <p>Oversteering effect if locked</p>	<p>eLSD open</p>  <p>Understeering effect if locked</p>

Figure 4.2. Control strategy of the proposed algorithm.

## 4.1. Upper-level controller

### 4.1.1. Analysis on actuator characteristics and vehicle responses

Before introducing the upper-level controller, it is necessary to explain the actuator characteristics, since the proposed control algorithm has been designed considering the characteristics of each actuator, i.e., IWMs and eLSD. In particular, since the actuator characteristics of in-wheel motors were discussed in detail in Section 3.2.1, this section focused on the characteristics of eLSD and their effects on vehicle response.

As shown in Figure 4.3(a), the powertrain architecture of interest in this section is rear wheel drive vehicle equipped with two front in-wheel motors and an eLSD at rear axle. In order to describe the vehicle lateral motion, a three-degree-of-freedom (3-DOF) planar model and bicycle model are used, as shown in Figure 4.3(b) [Gillespie'92, Rajamani'11]. The bicycle model can simplify the lateral dynamics, expressing the direct yaw moment as a single control input. The 3-DOF planar model can separately describe the forces and torques at each wheel. In this regard, bicycle model is used to design upper-level controller, and the 3-DOF planar model is utilized for lower-level controller design.

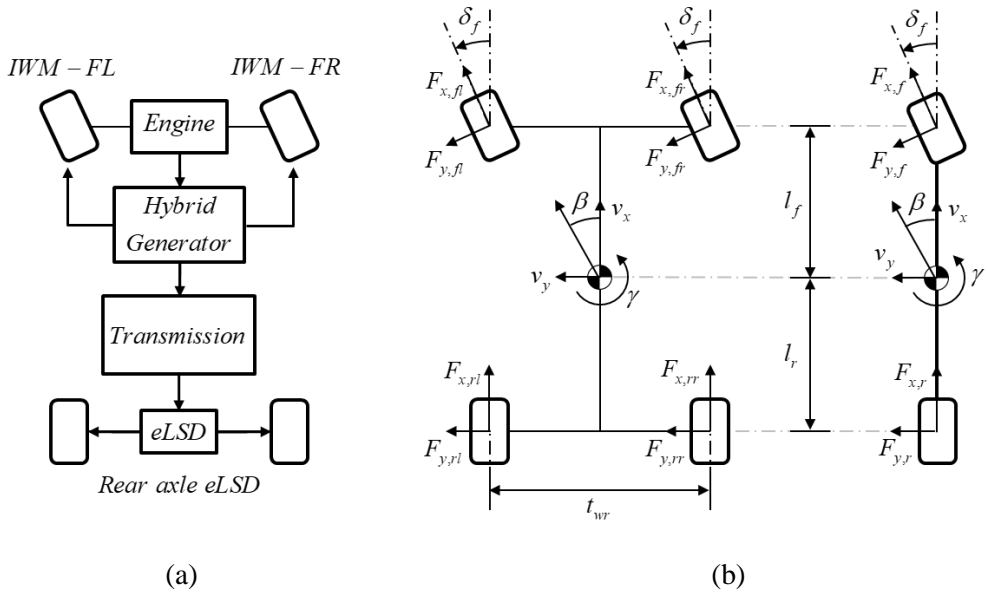


Figure 4.3. Vehicle model description: (a) the architecture of powertrain and (b) 3-DOF planar model and bicycle model.

In order to describe and understand the influences of the torque inputs for IWMS and eLSD, a 3-DOF planar model is slightly modified as follows:

$$\frac{dx}{dt} = f(x) + g \cdot u$$

where  $x = [v_x, \beta, \gamma]^T$ ,  $u = [F_{xfl,IWM}, F_{xfr,IWM}, M_{z,eLSD}]^T$ ,

$$f(x) = \begin{bmatrix} \frac{-F_{y,f} \sin \delta_f + F_{x,r} + v_x \beta \gamma}{m} \\ \frac{F_{y,f} \cos \delta_f + F_{y,r} - \gamma}{m v_x} \\ \frac{l_f F_{y,f} \cos \delta_f - l_r F_{y,r}}{I_z} \end{bmatrix}, g = \begin{bmatrix} \frac{\cos \delta_f}{m} & \frac{\cos \delta_f}{m} & 0 \\ \frac{\sin \delta_f}{m v_x} & \frac{\sin \delta_f}{m v_x} & 0 \\ \frac{l_f \sin \delta_f}{I_z} & \frac{l_f \sin \delta_f}{I_z} & \frac{1}{I_z} \end{bmatrix} \quad (39)$$

where  $F_{xfl,IWM}$  and  $F_{xfr,IWM}$  are the longitudinal tire forces to be controlled by two front in-wheel motors;  $M_{z,eLSD}$  is the yaw moment generated by the eLSD at rear axle.

Since Equation (39) is not enough to describe how eLSD clutch torque input

generate the yaw moment, the eLSD clutch model is additionally introduced to express the vehicle response to the eLSD clutch torque input.

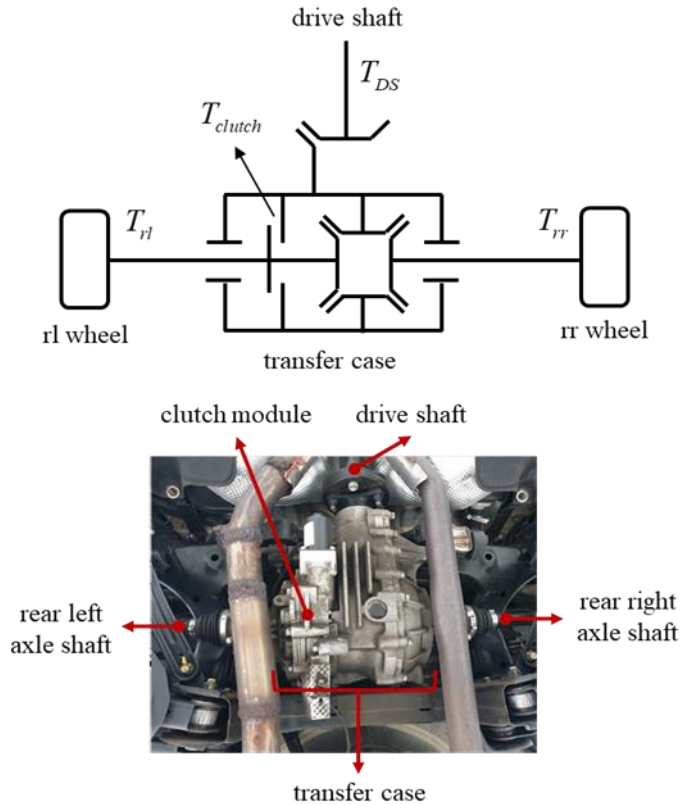


Figure 4.4. A schematic of eLSD equipped in the rear axle of the test vehicle.

As shown in Figure 4.4, the eLSD clutch module can provide the additional torque transfer path to the left or right wheel, generating the torque bias between left and right wheels. In order to mathematically express this torque biasing effect, following assumptions were applied: 1) the efficiency of torque transfer is 1.0; 2) The mass and moment inertia of each eLSD module component is negligible. Based on these assumptions, following equations can be utilized as follows [Piyabongkarn'06]:

$$T_{DS} = T_{clutch} + T_{TC}, \quad (40a)$$

$$T_{rl} = T_{clutch} + \frac{T_{TC}}{2} = \frac{T_{DS} + T_{clutch}}{2}, \quad (40b)$$

$$T_{rr} = \frac{T_{TC}}{2} = \frac{T_{DS} - T_{clutch}}{2}, \quad (40c)$$

$$\text{sgn}(T_{clutch}) = \text{sgn}(\Delta w),$$

$$\Delta w = w_{TC} - w_{rl} = \left( \frac{w_{rl} + w_{rr}}{2} \right) - w_{rl} = \frac{w_{rr} - w_{rl}}{2}, \quad (40d)$$

where  $T_{DS}$  is a transferred torque through the drive shaft;  $T_{clutch}$  is an eLSD clutch torque;  $T_{TC}$  is a torque transferred to the transfer case;  $w_{TC}$  is the angular speed of the differential transfer case;  $\Delta w$  is a relative rotational speed between the differential transfer case and rear left axle.

As described in Equations (40a)-(40d), the eLSD clutch plate can only transfer torque from the faster to the slower wheels. Thus, the sign of the relative speed between the transfer case and rear-left axle  $\Delta w$  is the same with that of the eLSD clutch torque  $T_{clutch}$ . In short, the relative speed between the left and right wheels determines the direction of the torque transfer, i.e.,  $\text{sgn}(T_{clutch}) = \text{sgn}(w_{rr} - w_{rl})$ .

Based on the wheel dynamics [Rajamani'11] and Equations (40b)-(40c), the additionally generated yaw moment by eLSD can be expressed as follows:

$$I_w \frac{dw_{rl}}{dt} = T_{rl} - r_{eff} F_{x,fl}, \quad I_w \frac{dw_{rr}}{dt} = T_{rr} - r_{eff} F_{x,rr}, \quad (41a)$$

$$T_{rl} = \frac{T_{DS} + T_{clutch}}{2}, \quad T_{rr} = \frac{T_{DS} - T_{clutch}}{2}, \quad (41b)$$

$$M_{z,eLSD} = \frac{t_{wr}}{2} (F_{x,rr} - F_{x,rl}) = \frac{t_{wr}}{2r_{eff}} \left[ -T_{clutch} - I_w \frac{d(w_{rr} - w_{rl})}{dt} \right] \quad (41c)$$

where  $I_w$  is the moment of inertia for each wheel; With the assumption that the moment of inertia for each wheel is negligible, the 3-DOF planar model can be slightly modified in terms of the torque inputs for IWMs and eLSD as follows:

$$\frac{dx}{dt} = f(x) + g^* \cdot u^*$$

where  $x = [v_x, \beta, \gamma]^T$ ,  $u^* = [F_{xfl,IWM}, F_{xfr,IWM}, M_{z,eLSD}]^T$ ,

$$f(x) = \begin{bmatrix} \frac{-F_{y,f} \sin \delta_f + F_{x,r}}{m} + v_x \beta \gamma \\ \frac{F_{y,f} \cos \delta_f + F_{y,r}}{mv_x} - \gamma \\ \frac{l_f F_{y,f} \cos \delta_f - l_r F_{y,r}}{I_z} \end{bmatrix}, g^* = \begin{bmatrix} \frac{\cos \delta_f}{m} & \frac{\cos \delta_f}{m} & 0 \\ \frac{\sin \delta_f}{mv_x} & \frac{\sin \delta_f}{mv_x} & 0 \\ \frac{l_f \sin \delta_f}{I_z} & \frac{l_f \sin \delta_f}{I_z} & \frac{1}{I_z} \end{bmatrix}, \quad (42)$$

$$g^* = g \cdot \text{diag} \left[ \frac{1}{r_{eff}}, \frac{1}{r_{eff}}, -\frac{t_{wr}}{(2 \cdot r_{eff})} \right]$$

where  $T_{fl,IWM}$  and  $T_{fr,IWM}$  are the front-left and front-right wheel torques generated by in-wheel motor control, respectively.

However, there are some points to be checked in Equation (42). Firstly, the longitudinal tire forces of the rear wheels  $F_{y,r}$  are generated by the drivers' throttle and brake pedal inputs. Secondly, the control inputs  $u^*$  to the IWM and eLSD modules are expressed in the form of the torque commands. Lastly, since the outer wheel is faster than the inner wheel in a normal cornering conditions without wheel slip, the sign of eLSD clutch torque input  $T_{clutch}$  is defined as a positive value in this condition. Thus, in this moderate driving, the eLSD clutch torque input generates yaw damping and understeering effect of the lateral motion [Gadola'18]. Additionally, it is necessary to understand the actuator characteristics for a controller design. Especially, the potential risk of the eLSD control should be revealed to design an eLSD controller.

From Equations (41a), the following equation can be derived:

$$I_w \frac{d}{dt} (w_{rr} - w_{rl}) = -T_{clutch} - r_{eff} F_{x,rr} + r_{eff} F_{x,rl}, \quad (43)$$

On the other hand, the eLSD clutch can be modeled using a torsional spring-damper as follows [Piyabongkarn'06]:

$$T_{clutch} = c \cdot \Delta w + \int_{t_0}^{t_0+t} k \cdot \Delta w dt, \quad (44)$$

$$\Delta w = w_{rC} - w_{rl} = \frac{w_{rl} + w_{rr}}{2} - w_{rl} = \frac{w_{rr} - w_{rl}}{2},$$

where  $c$  is the torsional damping coefficient of clutch;  $k$  is the torsion spring coefficient of clutch;  $t_0$  is the starting time of the clutch locking;  $t$  is the elapsed time after locking the clutch. Integrating the Equations (43) and (44), the following equation can be obtained:

$$2I_w \cdot \frac{d\Delta w}{dt} + c \cdot \Delta w + \int_{t_0}^{t_0+t} k \cdot \Delta w dt = r_{eff} (F_{x,rl} - F_{x,rr}), \quad (45)$$

As shown in the above equation, eLSD clutch module cannot directly control the direction magnitude of the transferred torque, and they are determined by the dynamic relationship between the relative angular velocity  $\Delta w$  and the longitudinal tires forces of the left and right wheels, i.e.,  $F_{x,rl}$  and  $F_{x,rr}$ . However, it can be confirmed that the left and right wheel speeds become the same as the eLSD clutch module is locked.

To analyze the cornering response with a locked eLSD, it is assumed that left and right wheels are rigidly connected and rotating at the same wheel speed with a lock differential [Gadola'18]. The wheel slip ratio in accelerating and braking is defined as follows [Pacejka'05]:

$$\lambda_i = \begin{cases} \frac{v_{x,i} - r_{eff} w_i}{v_{x,i}} & (v_{x,i} > r_{eff} w_i, \text{ braking}) \\ \frac{r_{eff} w_i - v_{x,i}}{r_{eff} w_i} & (v_{x,i} < r_{eff} w_i, \text{ accelerating}) \end{cases} \quad (46)$$

where  $w_i$  and  $v_{x,i}$  are the wheel speed and longitudinal at the  $i$ th wheel center, respectively;  $i$  is the index corresponding to the front-left, front-right, rear-left, and rear-right ( $= fl, fr, rl, rr$ ).

In the accelerating and braking conditions at cornering, the slip ratio difference between the rear-left and rear-right wheels can be expressed as follows [Gadola'18]:

$$\lambda_{rl} - \lambda_{rr} = \begin{cases} r_{eff} w_r \cdot \frac{t_{wr} \cdot \gamma}{\left(v_x - \frac{t_{wr}}{2} \gamma\right) \left(v_x + \frac{t_{wr}}{2} \gamma\right)} & (v_{x,i} > r_{eff} w_i, \text{ braking}) \\ \frac{t_{wr}}{r_{eff} w_r} \cdot \gamma & (v_{x,i} < r_{eff} w_i, \text{ accelerating}) \end{cases} \quad (47a)$$

$$w_r = w_{rl} = w_{rr}, \quad (47b)$$

where  $w_r$  is the wheel speed of rear wheels; As shown in Equation (47a), the slip ratio difference is determined by the vehicle states, such as rear wheel speeds, vehicle speed, and the yaw rate.

The additional yaw moment generated by a locked differential clutch is determined by the tire characteristics that depend on the slip ratio and vertical load difference between the left and right wheels. One thing to be noted is that the effects of the locked differential on vehicle motion is different under acceleration and deceleration in a turn [Gadola'18]. Depending on the driving conditions, a locked differential can create an understeering effect or an oversteering effect. Therefore, it is important to understand these characteristics well for eLSD controller design, since the control can be performed in the opposite direction to the intended one if the eLSD is locked without considering the driving conditions.

As shown in Figure 4.5, under the acceleration and deceleration in a turn with low lateral acceleration, the locked eLSD clutch differential makes the understeering effect on lateral motion. Additionally, under the deceleration in a turn with high lateral acceleration, the understeering effect is further enlarged due to the load transfer between the left and right wheels, as shown in Figure 4.5(b).



However, it should be noted that the eLSD locking can cause the oversteering effect under acceleration in a turn with high lateral acceleration, as shown in Figure 4.5(a). In other words, locking the eLSD in this situation can cause the spin-out and loss of stability, deteriorating the oversteering maneuvers. Thus, it should be avoided to lock the rear-wheel-drive eLSD clutch at the on-throttle cornering with high lateral acceleration.

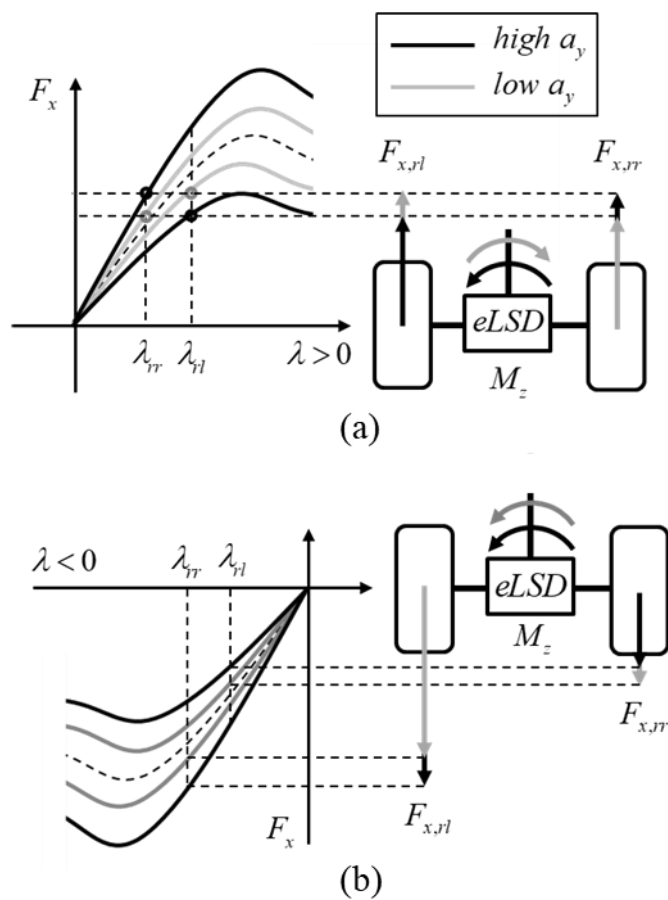


Figure 4.5. Yaw moment generation by a locked differential: (a) acceleration in a turn and (b) deceleration in a turn.

Before explaining the desired yaw moments for IWMs and eLSD, it is necessary

to explain how to target motion has been determined. The target motion is determined based on a target understeer gradient and yaw rate reference. The target understeer gradient is designed to modify the steady-state yaw rate using a nonlinear static map that receives the steering angle and vehicle speed as input variables [Canale'08, Goggia'14], and the yaw rate reference is calculated based on the target understeer gradient. With the assumption of steady-state cornering, the target understeer gradient and yaw rate reference can be formulated as follows:

$$\Delta K_{us,IWM} = f(\delta_f, v_x), \quad (48a)$$

$$K_{us,des} = K_{us} + \Delta K_{us,IWM}, \quad (48b)$$

$$\gamma_{des} = \frac{v_x}{L + K_{us,des} v_x^2} \cdot \delta_f, \quad (48c)$$

where  $K_{us,des}$  is the target understeer gradient;  $\Delta K_{us,IWM}$  is the variation of the understeer gradient to be modified by in-wheel motor control;  $\gamma_{des}$  is the yaw rate reference to be tracked by eLSD control.

#### 4.1.2. Feedforward control using in-wheel motors

The purpose of the upper-level controller is to calculate the desired yaw moment for target motion generation. The upper-level controller separately calculates the two desired yaw moments for each actuators, i.e., in-wheel motor (IWM) and electronic limited slip differential (eLSD). Considering the actuator characteristics, the in-wheel motors are controlled to shape both the steady-state and transient yaw rate responses, and the eLSD was utilized for feedback control to enhance the robustness against the model uncertainties by tracking the yaw rate reference. The upper-level controller consists of the three parts: 1) feedforward control for steady-state yaw rate response; 2) feedforward control for transient yaw rate response; 3)

feedback control to track the yaw rate reference;

The feedforward IWM control input can be expressed in the time domain based on Equation (29) of Section 3.1.2 as follows:

$$M_{z,IWM,ff} = M_{z,IWM,ff} + M_{z,IWM,tr}, \quad (49a)$$

$$M_{z,IWM,ss} = -\frac{2\hat{C}_f\hat{C}_rL}{\hat{C}_f + \hat{C}_r} \Delta K_{us,IWM} \cdot v_x \gamma, \quad (49b)$$

$$M_{z,IWM,tr} = I_z(1-\eta) \cdot \frac{d\gamma}{dt}, \quad (49c)$$

where  $M_{z,IWM,ff}$  is the feedforward in-wheel motor control input;  $M_{z,IWM,ss}$  is the feedforward control input for steady-state response;  $M_{z,IWM,tr}$  is the feedforward control input for transient response.

#### 4.1.3. Feedback control using electronic limited slip differential

The sliding mode control is designed to track the yaw rate reference using the electronic limited slip differential (eLSD) [Piyabongkarn'10]. As aforementioned, in a normal driving without tire saturations, eLSD locking generates the yaw damping and understeering effect on the vehicle lateral motion. Thus, the eLSD should be controlled only when the yaw rate is greater than the yaw rate reference. On the contrary, the eLSD controller should disengage the clutch when the yaw rate is lower than its reference value, since eLSD locking can only generate the understeering effect.

The yaw rate tracking control is devised using the bicycle model with in-wheel motor control input as follows:

$$ma_y = F_{y,f} + F_{y,r}, \quad (50a)$$

$$I_z \frac{d\gamma}{dt} = l_f F_{y,f} - l_r F_{y,r} + M_{z,IWM,ff} + M_{z,eLSD,fb}, \quad (50b)$$

where  $M_{z,IWM,ff}$  is the feedforward in-wheel motor control input;  $M_{z,eLSD,fb}$  is the eLSD control input to be designed for yaw rate feedback; According to the sliding mode theory [Slotine'91, Khalil'15, Edwards'98], the sliding surface and reaching condition can be described as follows:

$$s = \gamma - \gamma_{des}, \quad (51a)$$

$$\frac{1}{2} \frac{d}{dt} s^2 = s \cdot \frac{ds}{dt} \leq -k_s |s|, \quad (51b)$$

where  $s$  is the sliding surface;  $k_s$  is the sliding gain. Based on Equations (50a)-(51b), the desired yaw moment for yaw rate tracking with eLSD can be described as follows:

$$M_{z,eLSD,fb} = I_z \frac{d\gamma_{des}}{dt} - l_f \hat{F}_{y,f} + l_r \hat{F}_{y,r} - M_{z,IWM,ff} - k_s \cdot sat(s), \quad (52a)$$

$$sat(s) = \begin{cases} s & \text{if } |s| < s_{th} \\ \text{sgn}(s) & \text{else} \end{cases}, \quad (52b)$$

where  $\hat{F}_{y,f}$  and  $\hat{F}_{y,r}$  are the estimated lateral tire forces of front rear wheels, respectively;  $s_{th}$  is the threshold value for the saturation function.

## 4.2. Lower-level controller

The lower level controller determines the torque inputs commands for the two front in-wheel motors (IWMs) and electronic limited slip differential (eLSD) at rear axle in consideration of the actuator characteristics and tire saturation. As aforementioned, the in-wheel motor torque inputs are calculated to generate the desired yaw moment for feedforward control, and the eLSD torque inputs is determined to reduce the yaw rate overshoot with generating the understeering effect based on the desired yaw moment from the upper-level controller for yaw rate error feedback. Additionally, the eLSD torque inputs are devised to avoid the unintended loss of lateral stability, particularly, in the case of eLSD-locking at the on-throttle cornering with high lateral acceleration maneuvers [Gadola'18]:

In summary, the lower-level controller determines the torque commands for the two actuators, i.e., IWM and eLSD, satisfying the following conditions:

- 1) Transforming the desired yaw moments to the torque commands;
- 2) Saturating the torque inputs considering the actuator and tire friction limit;
- 3) Transferring the eLSD clutch torque in the desired direction to avoid the unintended loss of lateral stability;

### 4.2.1. Transforming the desired yaw moments to the torque commands

In the lower-level controller, the desired yaw moment for feedforward control  $M_{z,IWM,ff}$  is converted to the two front wheel torque inputs. The desired in-wheel motor torque inputs are calculated using the following equations [Nam'12, Fujimoto'05]:

$$M_{z,IWM,ff} = \frac{t_{wf}}{2}(F_{x,fr} - F_{x,fl}), \quad (53a)$$

$$F_{x,fl} + F_{x,fr} = 0, \quad T_{fl} = r_{eff} F_{x,fl}, \quad T_{fr} = r_{eff} F_{x,fr}, \quad (53b)$$

$$T_{fl,des} = -\frac{r_{eff}}{t_{wf}} M_{z,IWM,ff}, \quad T_{fr,des} = \frac{r_{eff}}{t_{wf}} M_{z,IWM,ff}, \quad (53c)$$

where  $T_{fl,des}$  and  $T_{fr,des}$  are the desired torque inputs for front-left and front-right wheels, respectively. As shown in Equation (53b), the two front in-wheel motors are controlled only the lateral motion and not the longitudinal motion. The condition (53b) is set in order to use all available torque inputs for the lateral motion control. From Equations (53a) and (53b), the desired torque inputs for the two front wheels are calculated as Equation (53c).

On the other hand, the desired yaw moment for feedback control using the eLSD can be converted as the clutch torque command. The desired torque input for eLSD can be calculated as following equations:

$$M_{z,eLSD,fb} = \frac{t_{wr}}{2}(F_{x,rr} - F_{x,rl}), \quad (54a)$$

$$T_{rl} = r_{eff} F_{x,rl} = \frac{T_{DS} + T_{clutch}}{2}, \quad T_{rr} = r_{eff} F_{x,rr} = \frac{T_{DS} - T_{clutch}}{2}, \quad (54b)$$

$$T_{clutch,des} = -\frac{2r_{eff}}{t_{wr}} M_{z,eLSD,fb}, \quad (54c)$$

where  $T_{clutch,des}$  is the desired clutch torque input for eLSD module. Especially, it should be noted that the desired clutch torque input  $T_{clutch,des}$  is positive (or negative) value when the rear-right wheel is faster (or slower) than the rear-left wheel, i.e.,  $\text{sgn}(T_{clutch,des}) = \text{sgn}(w_{rr} - w_{rl})$ .

#### 4.2.2. Saturating the torque inputs considering the actuator and tire friction limit

Another one to be considered in the lower-level controller is the actuator and tire

friction limit in order to prevent the tire saturation and actuator failure. The actuator limits for in-wheel motors are already explain in Section 3.2.1. The tire friction limits can be considered using the friction ellipse model [Pacejka'05]. The actuator and tire friction limits for IWM control can be expressed using the following equations:

$$T_{fl,max} = \begin{cases} T_{IWM,max} & \text{if } w_{fl} \leq w_{base} \\ \frac{P_{IWM,max}}{w_{fl}} & \text{else} \end{cases}, \quad T_{fr,max} = \begin{cases} T_{IWM,max} & \text{if } w_{fr} \leq w_{base} \\ \frac{P_{IWM,max}}{w_{fr}} & \text{else} \end{cases}, \quad (55a)$$

$$\hat{F}_{x,max,i} = \sqrt{(\mu \hat{F}_{z,i})^2 - \hat{F}_{y,i}^2}, \quad (55b)$$

where  $T_{fl,max}$  and  $T_{fr,max}$  are the maximum in-wheel motor torque inputs for front-left and front-right wheels, respectively;  $T_{IWM,max}$  and  $P_{IWM,max}$  are the maximum motor torque and power in the torque and power constant region, respectively;

#### 4.2.3. Transferring the eLSD clutch torque in the desired direction

As aforementioned in Section 4.1.1, the left and right torque transfer by eLSD clutch cannot be directly controlled, and the torque transfer is determined by the wheel slip difference and the tire characteristics. Therefore, eLSD locking during the acceleration near the limits of handling can cause the vehicle instability and spinout [Gadola'18]. Due to this reason, the activating conditions for eLSD are required to guarantee the torque transfer in the desired direction [Cha'22].

In order to guarantee the feasibility for the torque transfer to the desired direction, three new indices are proposed in this study as follows: 1) an oversteer index  $I_{ovx}$ ; 2) a torque transfer direction index  $I_{dir}$ ; 3) a handling limit index  $I_{lim}$ ;

The oversteer index  $I_{ovx}$  shows whether the current yaw rate is greater than the yaw rate reference. The torque transfer direction index  $I_{dir}$  indicates whether torque will be transferred in the intended direction when the eLSD clutch is locked. The handling limit index  $I_{lim}$  expresses whether the vehicle is in a limit handling condition. The three indices can be described as follows:

$$I_{ovs} = \begin{cases} 1 & \text{if } \text{sgn}(\delta_f) = \text{sgn}(\gamma - \gamma_{des}), \\ 0 & \text{else} \end{cases}, \quad (56a)$$

$$I_{dir} = \begin{cases} 1 & \text{if } \text{sgn}(T_{clutch,des}) = \text{sgn}(w_{rr} - w_{rl}), \\ 0 & \text{else} \end{cases}, \quad (56b)$$

$$I_{limit} = \begin{cases} 1 & \text{if } a_y > a_{y,th} \text{ and } APS > APS_{th}, \\ 0 & \text{else} \end{cases}, \quad (56c)$$

where  $a_{y,th}$  is the threshold value for high lateral acceleration;  $APS$  and  $APS_{th}$  are the acceleration pedal sensor signal value and its threshold for high longitudinal acceleration, respectively. Utilizing the three indices, the state transition diagram for eLSD activation conditions can be described as Figure 4.6.

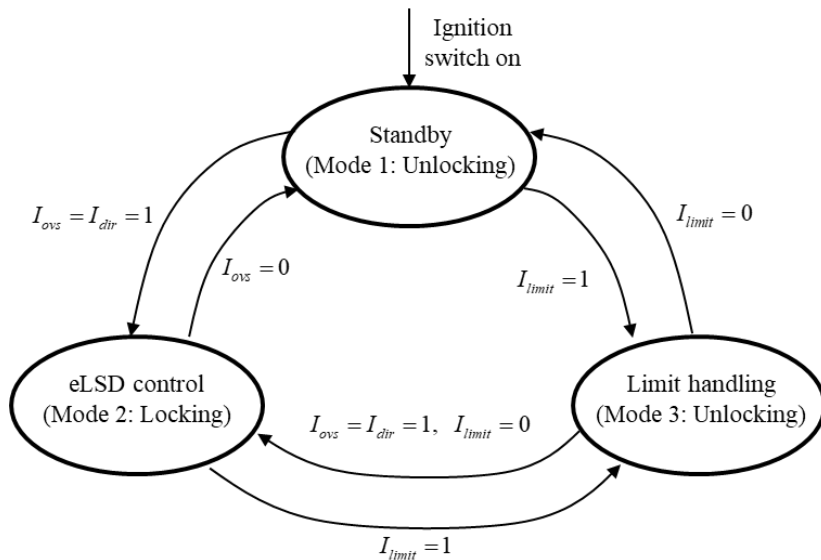


Figure 4.6. State transition diagram for the eLSD activation condition.



As presented in Figure 4.6, there are three modes to determine the eLSD control authority: 1) Standby; 2) eLSD control; 3) Limit handling. The three modes each have their own meaning as follows: 1) Standby mode is the default state that is started when the ignition switch is on; 2) eLSD control mode stands for the condition that need to be contented for the activation of the eLSD; 3) Limit handling mode is a warning signal to unlocked the eLSD clutch to avoid the loss of stability due to the locked differential at handling limits. The state transition from one state to another one only occurs when the transition conditions are satisfied based on the proposed three indices, as shown in Figure 4.6. For example, the state transition from Mode 1 to Mode 2 takes place only when the oversteer and torque transfer direction indices are equal to one, i.e.,  $I_{ovx} = I_{dir} = 1$ , which stands for the condition that the current yaw rate is larger than the desired value and the eLSD clutch torque would be transferred in the intended direction. Additionally, the eLSD clutch is controlled only in the eLSD control mode (mode 2). In this mode, the lower-level controller determines the eLSD torque command to be transmitted to the eLSD clutch module in the form of the absolute value for the desired eLSD clutch torque, i.e.,  $T_{clutch,cmd} = |T_{clutch,des}|$ .

# Chapter 5 Simulation Results

## 5.1. Effect of IWM control on vehicle motion

The proposed torque vectoring control algorithm for two front in-wheel motors has been investigated via the computer simulations using software Carsim and Matlab/Simulink. The vehicle parameters utilized for the computer simulations can be summarized in Table 5.1.

Table 5.1. Vehicle model parameters.

Parameter	Quantity	Value
$m$	Total vehicle mass	2300 kg
$l_f$	CG to front axle distance	1.51 m
$l_r$	CG to rear axle distance	1.50 m
$I_z$	Yaw moment of inertia	4400 kg·s <sup>2</sup>
$t_{wf}$	Track width of front axle	1.650 m
$r_{eff}$	Effective radius	0.332 m
$h_{RC}$	Height of roll center	0.57 m
$C_{f0}$	Nominal tire cornering stiffness of each front wheel	60000 N/rad
$C_{r0}$	Nominal tire cornering stiffness of each rear wheel	65000 N/rad
SGR	Steering gear ratio	14.583

The specifications of the in-wheel motor are described as follows: Maximum power, 30kW, maximum torque, 650Nm, maximum speed, 1610rpm, and base speed, 340rpm. The simulation studies have been conducted based on a hybrid drive vehicle, which is an E-segment sedan equipped with two front in-wheel

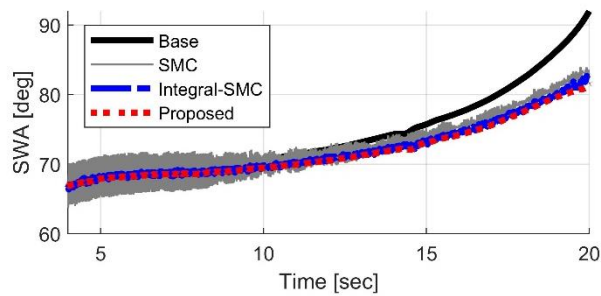
motors and an open-differential rear wheel drive with an internal combustion engine. Additionally, all simulations were conducted on dry asphalt road conditions, since the main scope of this study is to investigate the lateral motion control performance at high speeds. Sensor noise with the same variance level in test vehicle was added in the simulations.

The proposed control algorithm has been compared with three other cases: 1) a sliding mode controller for yaw rate tracking; 2) an integral sliding mode controller for yaw rate tracking; 3) an uncontrolled case. The uncontrolled case refers to the rear-wheel-drive ICE vehicle not receiving any form of in-wheel motor control. Additionally, an integral sliding mode controller was devised to avoid chattering and eliminate the discontinuous control action with a first-order low-pass filter [Goggia'14].

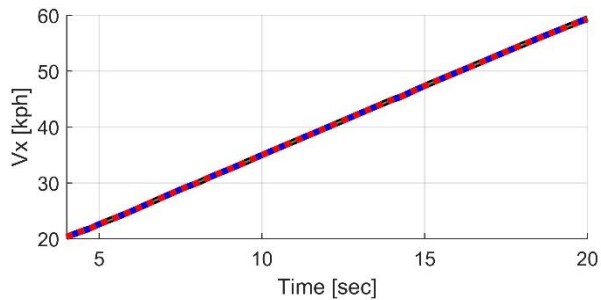
In order to evaluate the control performance, three test scenarios were considered: 1) constant radius circular turn test; 2) step steer test; 3) double-lane change test. Firstly, the purpose of the circular turn test is to investigate the steady-state cornering performance for several cases. Particularly, through the circular turn test, it can be confirmed that the proposed algorithm can reduce the understeer gradient and can increase the steady-state yaw gain, which is one of the control objective for the proposed algorithm. Secondly, the step steer test was conducted to compare the transient responses of several cases. Moreover, the yaw rate damping coefficient to steering input was identified to show the increased damping coefficient of the closed-loop system that was modified by the proposed algorithm. Lastly, the double-lane change test was also conducted to show the effects of the transient control input in severe maneuvers, with the results showing that the proposed algorithm could improve the lateral stability and reduce the vehicle

sideslip angle.

The purpose of the closed-loop circular turn test is to investigate the steady-state cornering performance. In this scenario, the path following driver model [Guo'93] is adopted to follow a circular path with a constant radius of 30m. The longitudinal velocity is steadily accelerated from 20kph to 60kph. In Figure 5.1, four cases were compared together: (1) an uncontrolled vehicle (Base); (2) yaw rate tracking with sliding mode control (SMC); (3) yaw rate tracking with integral sliding mode control (Integral-SMC); (4) proposed control algorithm (Proposed). The target understeer gradient is applied equally to all cases.



(a) Steering wheel angle



(b) Longitudinal velocity

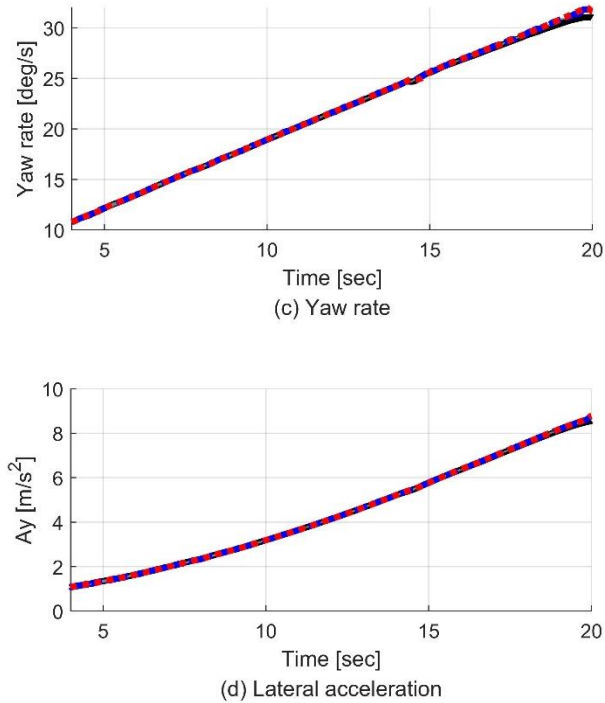


Figure 5.1. Vehicle states for the circular turn scenario with a constant radius of 30m.

Since the four cases are compared in the closed-loop tests, the vehicle speed, yaw rate, and lateral acceleration are all almost the same, as shown in Figure 5.1(b), (c), and (d). However, compared to the sliding mode control (SMC) and the uncontrolled case (Base), the proposed algorithm (Proposed) and integral sliding mode control (Integral-SMC) can reduce the steering effort at steady-state cornering without chattering problems, as shown in Figure 5.1(a). In order to directly display the enhanced steering characteristics and understeer gradient, the understeer curves have been illustrated in Figure 5.2.

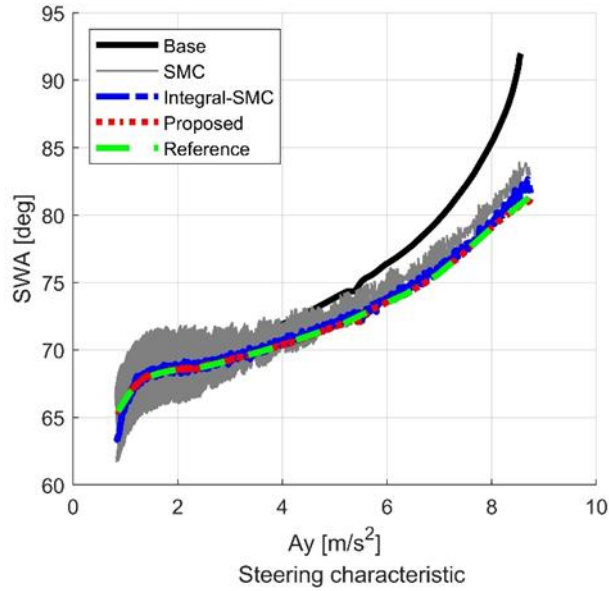
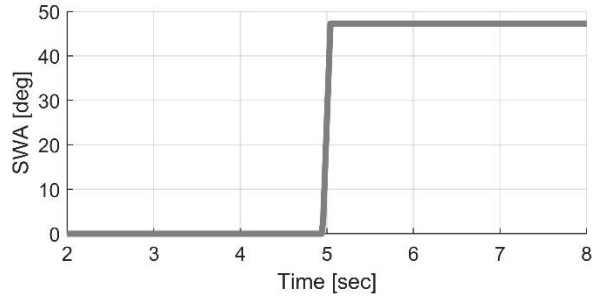


Figure 5.2. Understeer curve in a circular turn with a constant radius of 30m.

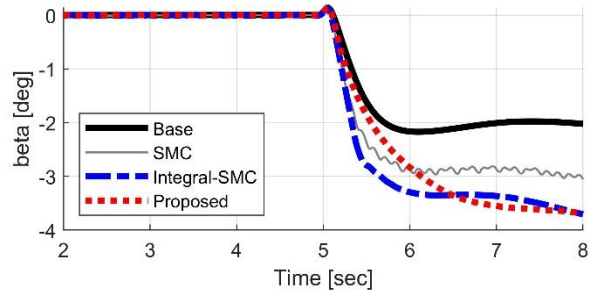
As shown in Figure 5.2, the proposed algorithm and integral sliding mode control can reduce the vehicle understeer gradient with increasing the steady-state yaw gain, compared to the Base vehicle. However, it should be noted that control input smoothing techniques, such as integral sliding mode control or boundary layer near the sliding surface in sliding mode control, can deteriorate the control performance in the transient responses, which will be further described in following simulation results.

The open-loop step steer test is performed to study the cornering performance in transient response. In the step steer, the open-loop step steering input is given to the vehicle. The vehicle speed is set as a constant 80kph. As in the previous simulation, four cases were compared: 1) Base; 2) SMC; 3) Integral-SMC; 4) Proposed. According to the ISO 7401 standard, the same step steer input is given to the vehicle in order to generate a lateral acceleration of 0.6g at steady-state for the the

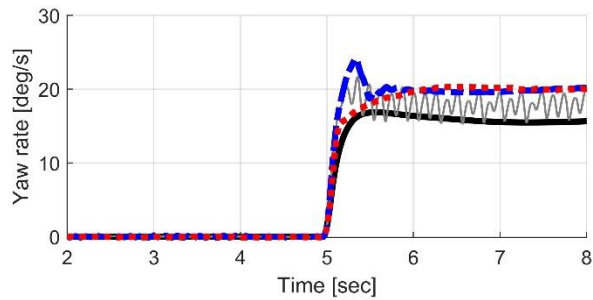
uncontrolled case (Base), as shown in Figure 5.3(a). The target understeer gradient is tuned equally for fair comparison. The simulation results are plotted in Figure 5.3.



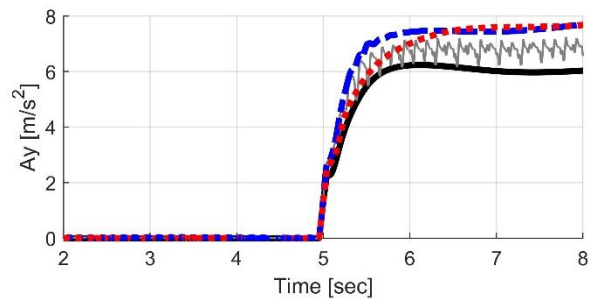
(a) Steering wheel angle



(b) sideslip angle



(c) Yaw rate



(d) Lateral acceleration

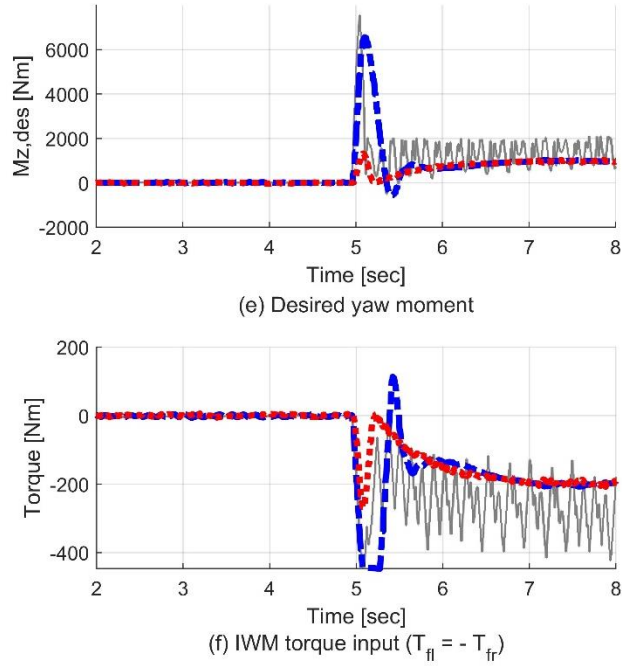


Figure 5.3. Open-loop step steer at 80kph.

As shown in Figure 5.3(c), the proposed algorithm can reduce the yaw rate overshoot with increasing the steady-state yaw gain. However, yaw rate response with sliding mode control suffers from the chattering issues, and delayed control input with the integral sliding mode control cannot effectively reduce the yaw rate overshoot in transient response, as shown in Figure 5.3(e) and (f). In short, though the Integral-SMC can alleviate the chattering issue and increase the steady-state yaw gain, the Integral-SMC shows a delayed control input compared to the SMC, which induces the deterioration of control performance in transient response. Meanwhile, the proposed algorithm can improve both the steady-state and transient responses, achieving their control objectives.



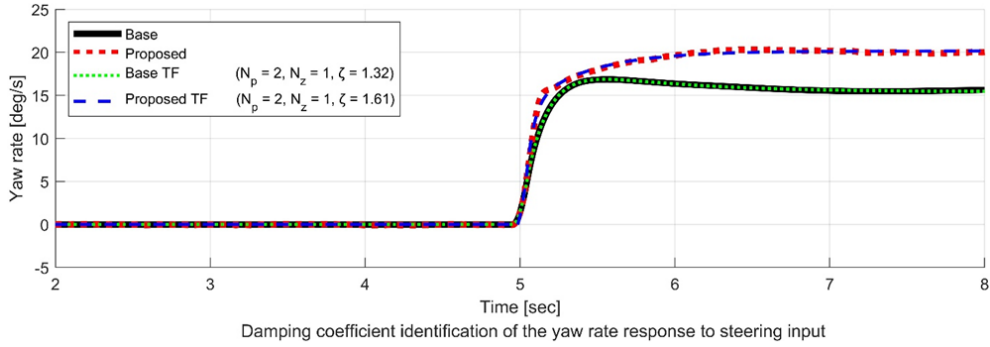
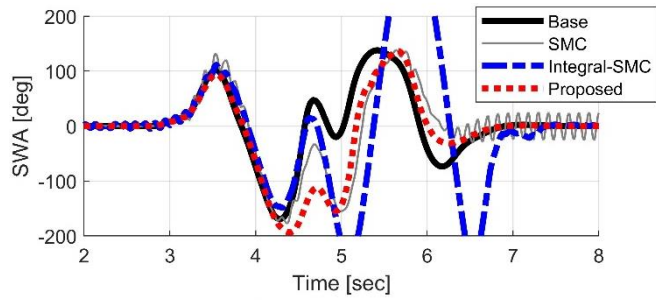


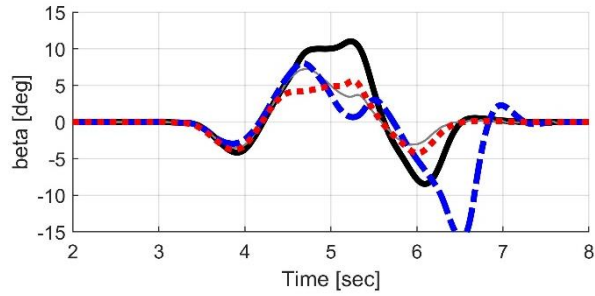
Figure 5.4. yaw rate damping coefficient identification.

Additionally, in order to show the increase yaw rate damping coefficient that is the objective of the transient control input, the closed-loop transfer function has been identified. The number of poles and zero, i.e.,  $N_p$  and  $N_z$ , is set as two and one, as described in Equation (34). As shown in Figure 5.4, the identification result shows that the proposed algorithm can increase the damping coefficient of the closed-loop system, compared to the Base vehicle. The damping coefficient of the other two cases (i.e., SMC and Integral-SMC) are not compared together, since the proposed algorithm is designed to increase yaw rate damping coefficient but other methodologies are not. In summary, the step steer test results in simulation show that the steady-state and transient control inputs can accomplish their objectives, shaping the steady-state and transient yaw rate response.

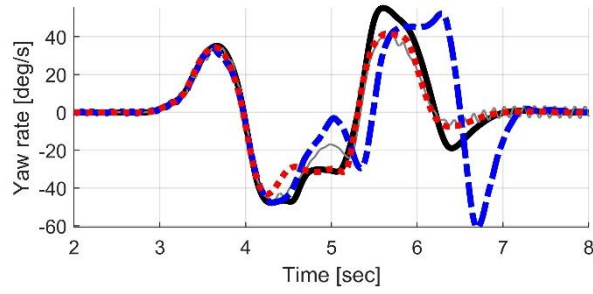
The closed-loop double lane change is conducted to examine the transient cornering response with high-frequency steering input and in a severe maneuver. In this test, a path following model [Guo'93] attempted to negotiate the given path. The initial speed was set as 65kph, and no throttle and brake input were applied to excluding the effects of pedal inputs on lateral motion.



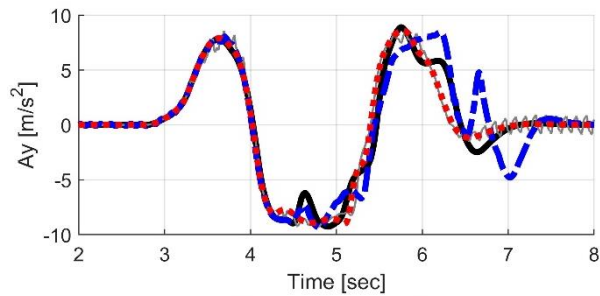
(a) Steering wheel angle



(b) sideslip angle



(c) Yaw rate



(d) Lateral acceleration

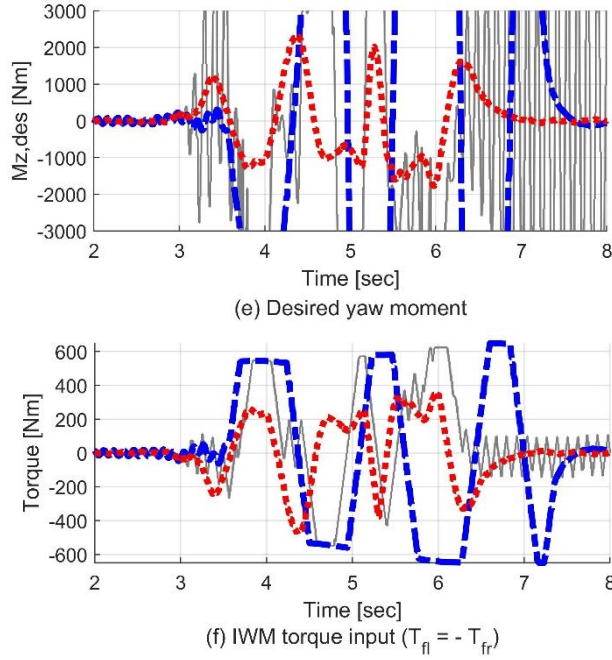


Figure 5.5. Closed-loop double lane change at 65kph.

As shown in Figure 5.5(b) and (c), the SMC is effective in reducing the sideslip angle, the chattering problem can be induced in the yaw rate response. Additionally, as shown in Figure 5.5(e) and (f), the control input for SMC shows high frequency chattering, and the control input for Integral-SMC deteriorate the transient cornering performance due to the delayed control action. It can shown in this scenario that the yaw rate tracking control can cause the chattering issues, and the chattering alleviation techniques cannot avoid the trade-off relationship between chattering smoothing and control performance, especially in severe maneuvers with high-frequency steering input.

Compared to the other compared methods (i.e., Integral-SMC, SMC, and Base), the proposed controller can improve the lateral stability and reduce the sideslip angle even in this severe maneuvers without chattering issues. In summary, the proposed control algorithm can achieve the significant improvements to vehicle

agility and lateral stability at steady-state and transient cornering, showing the superior performance compared to the other methodologies.

## 5.2. Effect of IWM/eLSD integrated control

In order to investigate and understand the effects of each actuator, i.e., IWMs and eLSD, on the high speed cornering performance, three simulation scenarios are performed as follows: 1) Open-loop sinusoidal steering input with acceleration; 2) Open-loop sinusoidal steering input with acceleration; 3) Open-loop step steering input with constant speed. The first two scenarios, i.e., open-loop sinusoidal steering input with acceleration and deceleration, are devised to mimic the aggressive cornering maneuvers at the limits of handling [Joa'18, Song'08]. These two scenarios are not incorporated in the ISO standard test scenario, and these are devised to study the cornering performance at aggressive high-speed cornering. Another scenario is the step steer scenario to show the yaw damping performance of the proposed algorithm.

The computer simulations for the validation of controller performance have been conducted for a rear wheel drive D-segment sedan that equipped with two additional actuators: 1) two front in-wheel motors (IWMs) and 2) the electronic limited slip differential (eLSD) in the rear axle. The computer simulations were conducted using the Carsim and Simulink software. The vehicle parameters utilized in the simulations are summarized in Table 5.2.

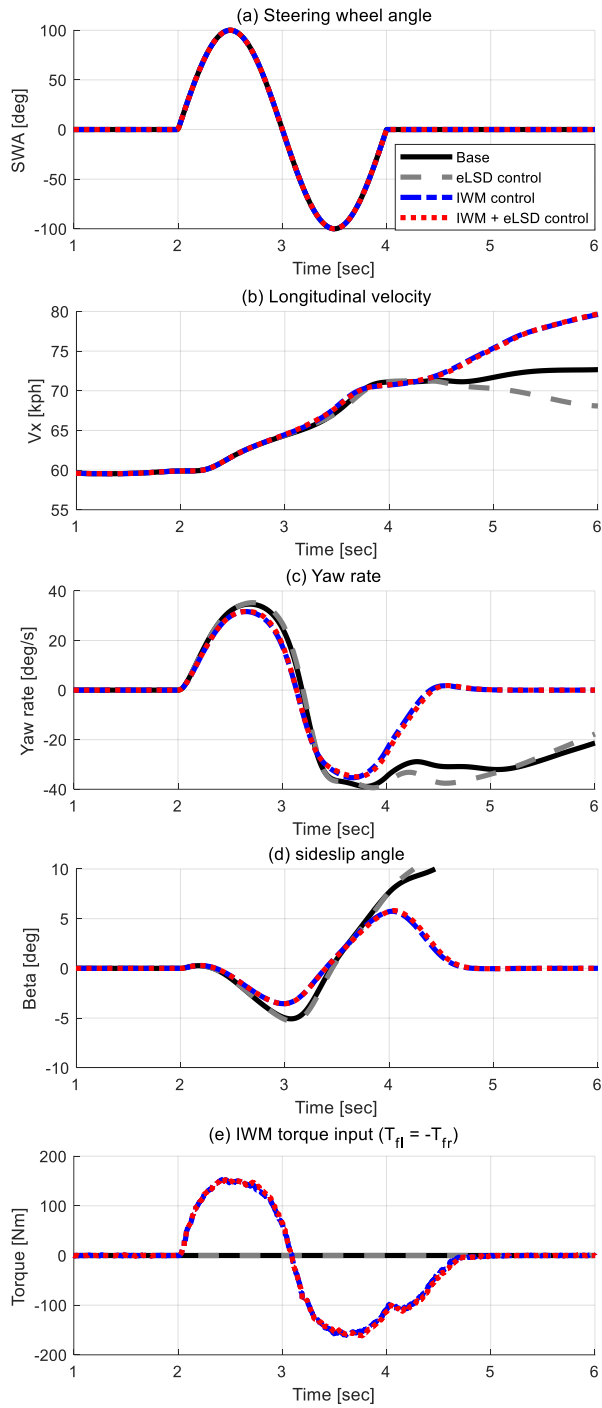
Table 5.2. Vehicle parameters.

Vehicle parameter	Symbol	Value	Unit
Vehicle mass	$m$	1960	kg
Yaw moment of inertia	$I_z$	3400	kg·s <sup>2</sup>
CG to front axle distance	$l_f$	1.32	m
CG to rear axle distance	$l_r$	1.52	m

Track width of front axle	$t_{wf}$	1.63	m
Track width of rear axle	$t_{wr}$	1.65	m
Height of CG	$h_{CG}$	0.57	m
Effective radius	$r_{eff}$	0.332	m

Additionally, in each scenario, four cases are compared together as follows: 1) an uncontrolled case (Base); 2) in-wheel motor control (IWM control); 3) electronic limited slip differential control (eLSD control); 4) integrated control of in-wheel motor and electronic limited slip differential (IWM and eLSD control), which is the vehicle response with the proposed controller. The four cases are compared in order to show the effects of each actuator on vehicle response and to present the integrated control of IWM and eLSD can provide a higher level of handling performance compared to the individual control of IWM and eLSD.

As aforementioned, the first simulation scenario is the open-loop sinusoidal steering input with acceleration to mimic the aggressive cornering maneuvers and to investigate the control performance at high-speed cornering. In this scenario, the open-loop sinusoidal steering input is given to the vehicle. The peak lateral acceleration during the scenario is higher than 0.8g, i.e.,  $a_y > 0.8g$ , to reproduce the vehicle cornering near the limits of handling. Additionally, the vehicle speed was accelerated from 60kph to 80kph in 3.6sec, which is equivalent to the longitudinal acceleration of 0.15g. In this scenario, four cases are compared to reveal the effects of each actuator on cornering performance. The first case is an uncontrolled vehicle (Base), the second case is the individual control of the two front in-wheel motors, the third case is the individual control of the rear axle eLSD, and the last case is the integrated control of two front in-wheel motors and the rear-wheel-drive eLSD, which is the proposed control algorithm in this section.



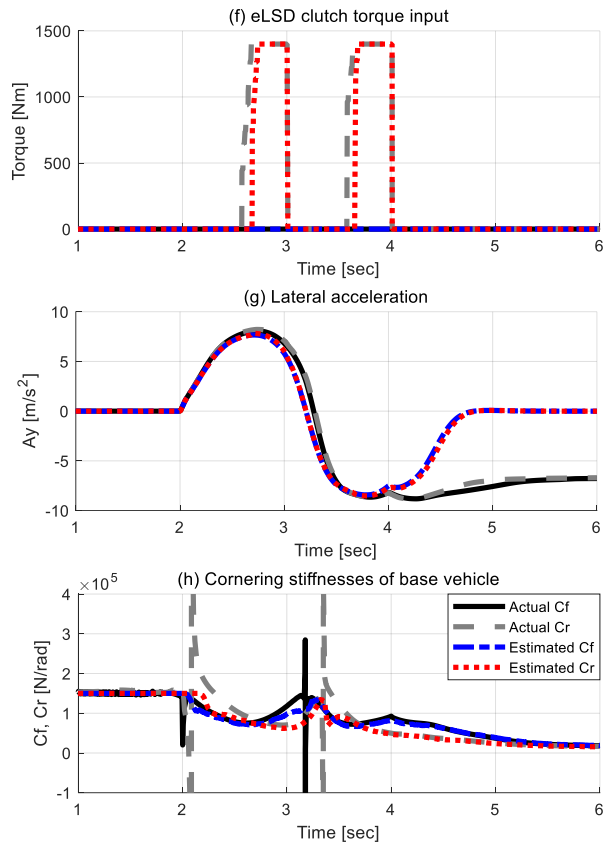


Figure 5.6. Open-loop sinusoidal steering input with acceleration.

Figure 5.6 shows the simulation results for the open-loop sinusoidal steering input with acceleration. As shown in Figure 5.6(g), the peak lateral acceleration in this scenario goes up to the around 0.9g to reproduce the cornering near the limits of handling. As shown in Figure 5.6(a), the same open-loop sinusoidal steering input is given to the vehicle in all the compared cases: 1) Base; 2) IWM control; 3) eLSD control; 4) integrated control of IWM and eLSD. As shown in Figure 5.6(b) and (c), the integrated control and IWM control can maintain the handling performance during the aggressive cornering near the limits of handling, while the uncontrolled case (Base) and eLSD control case shows the vehicle spin-out with the loss of vehicle stability and acceleration performance. Additionally, the vehicle



sideslip angle can be sustained at an appropriate level without vehicle spinout with the integrated control and IWM control, while the other cases show the loss of lateral stability.

Figure 5.6(e) and (f) present the control inputs for the two front IWM torques and eLSD clutch torque in the rear axle eLSD module, respectively. Particularly, the IWM torque inputs in Figure 5.6(e) are controlled with a continuous control action for feedforward control, while the eLSD torque input Figure 5.6(f) shows a discontinuous control action that is originated from eLSD control activation conditions in the lower-level controller for feedback control. Additionally, the real-time estimation results for the two cornering stiffness, i.e.,  $C_f$  and  $C_r$ , is illustrated in Figure 5.6(h), which is utilized in the feedforward control by in-wheel motor.

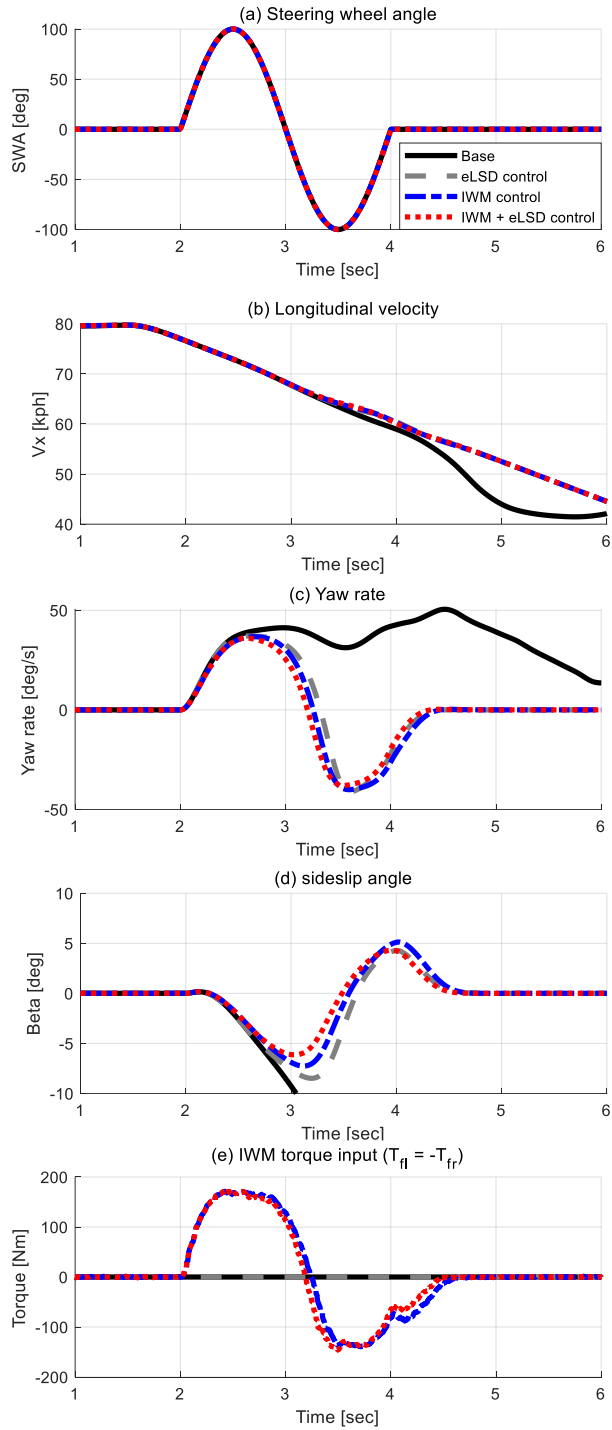
However, as already explained in eLSD actuator characteristics of Section 4.1.1, the eLSD control is not very effective in improving the cornering performance during acceleration [Gadola'18]. This fact can be confirmed when comparing the base vehicle and eLSD control, or even when comparing the IWM control and the integrated control. The two comparison reveals that the effects of the eLSD control on lateral motion are not significant. On the contrary, the eLSD control during deceleration is quite effective, which would be shown in the next simulation scenario.

The second scenario is the open-loop sinusoidal steering input with longitudinal deceleration. The peak lateral acceleration is also higher than 0.8g in this scenario. The vehicle speed is decelerated from 80kph to 40kph in 5sec, which corresponds to approximately longitudinal acceleration of -0.2g. Similarly in the previous

simulation scenario, four cases are compared together in this scenario as follows: 1) Base; 2) individual control of IWM; 3) individual control of eLSD; 4) integrated control of IWM and eLSD.

The simulation results for the open-loop sinusoidal steering input during deceleration have been shown in Figure 5.6. As shown in Figure 5.7(a), the same sinusoidal steering input was given to the vehicle in the four cases. Figure 5.7(b) and (c) show that only the base vehicle spins out and loses the deceleration performance, while other cases do not show the vehicle instability. Particularly as shown in the yaw rate and sideslip angle responses of Figure 5.7(c) and (d), the integrated control of IWM and eLSD shows the superior cornering performance compared to the individual control of IWM and eLSD. Figure 5.7(e) and (f) correspond to the control inputs of two front IWM torque and eLSD clutch torque, respectively. Figure 5.7(h) shows the estimation results for the two cornering stiffness.

Especially, different from the previous accelerating scenario, the eLSD control during acceleration can significantly improve the cornering performance, since the torque transfer between left and right wheels increases during the deceleration, as aforementioned in Section 4.1.1. As shown in Figure 5.7(c) and (d), the yaw rate and side slip angle responses are improved by the eLSD control. In particular, comparing the IWM control and the integrated control, the yaw rate phase delay and sideslip angle are reduced. Additionally, compared to the base vehicle, the individual eLSD control can prevent the vehicle from spinning out and from oversteering.



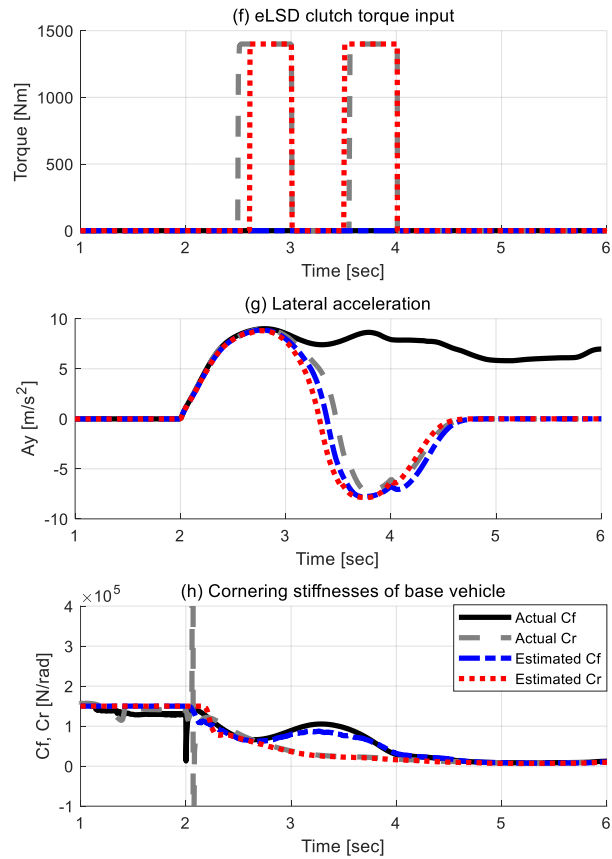
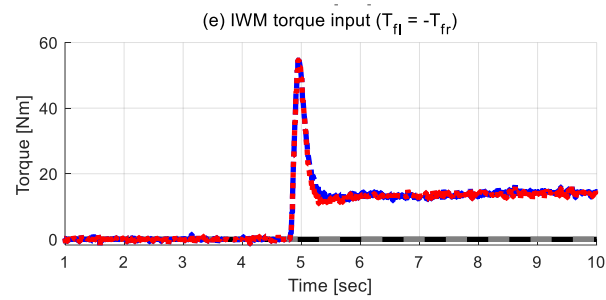
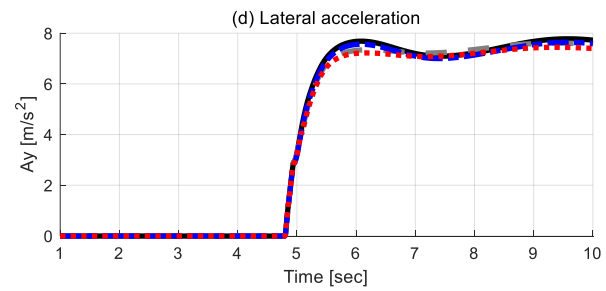
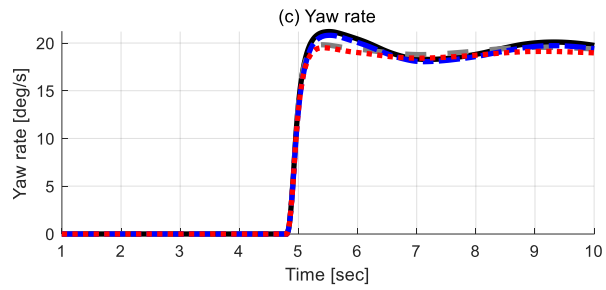
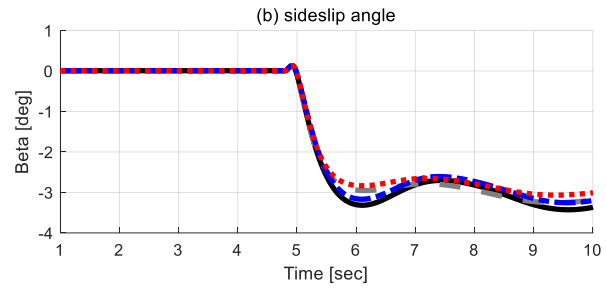
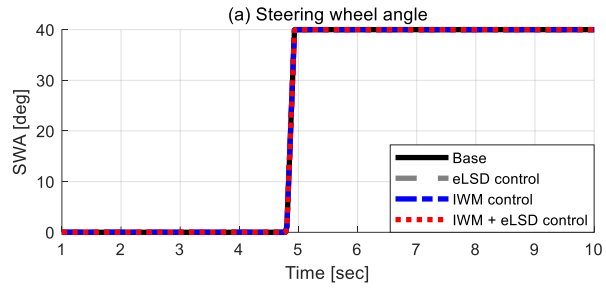


Figure 5.7. Open-loop sinusoidal steering input with deceleration.

The last scenario is the open-loop step steering input with a constant velocity, i.e., step steer test. The step steer test is performed at 80kph with a step steering input of 40deg to generate the steady-state lateral acceleration of 0.7g. The steady-state lateral acceleration is set as a higher value than the ISO standard, i.e., 0.4g and 0.6g, to simulate the maneuver near the limits of handling. As in other previous scenarios, the four cases are compared to reveal the control effect of each actuator on the transient yaw rate response.



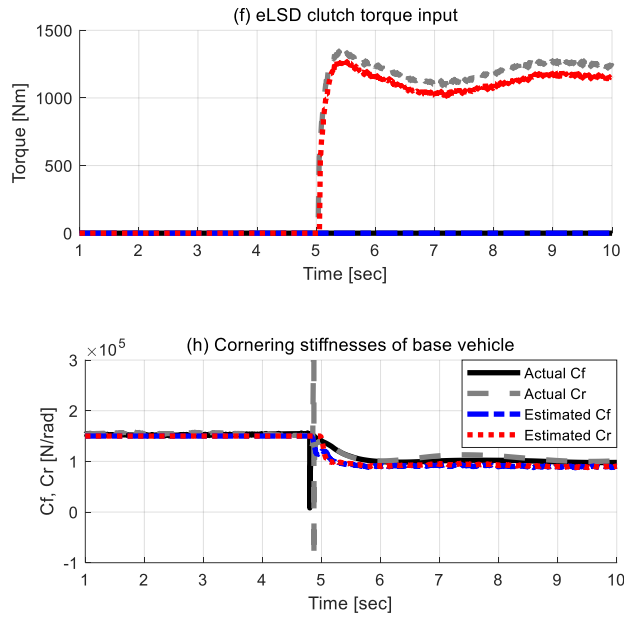


Figure 5.8. Open-loop step steer test at 80kph with a steady-state lateral acceleration of 0.7g.

Figure 5.8 presents the simulation results for the open-loop step steer test at 80kph with a steady-state lateral acceleration of 0.7g. The same step steering input is applied in the four cases, as shown in Figure 5.8(a). As shown in Figure 5.8(c), the integrated control of IWM and eLSD can diminish the yaw rate overshoot well compared to the individual control cases and uncontrolled case. Additionally, the integrated controller can alleviate the fluctuation in the yaw rate and sideslip angle, as shown in Figure 5.8(b) and (c). Especially as shown in Figure 5.8(e), the in-wheel motor torque input shows a momentary increase due to the feedforward control for the transient response. Figure 5.8(c) shows that the eLSD control can also reduce the yaw rate overshoot in the comparison between the Base and eLSD control and between IWM control and integrated control. In short, both IWM control and eLSD control can contribute to reducing the yaw rate overshoot in the step steer test.

# Chapter 6 Vehicle Test Results

## 6.1. Test results for IWM control

In order to implement and validate the proposed algorithm, a hybrid drive test vehicle has been developed by integrating the two front in-wheel motors into an internal combustion engine based rear wheel drive vehicle, as shown in Figure 6.1. In this vehicle setup, torques of the two front wheels are operated and controlled by two front in-wheel motors, and two rear wheels are driven by an internal combustion engine with an open differential.

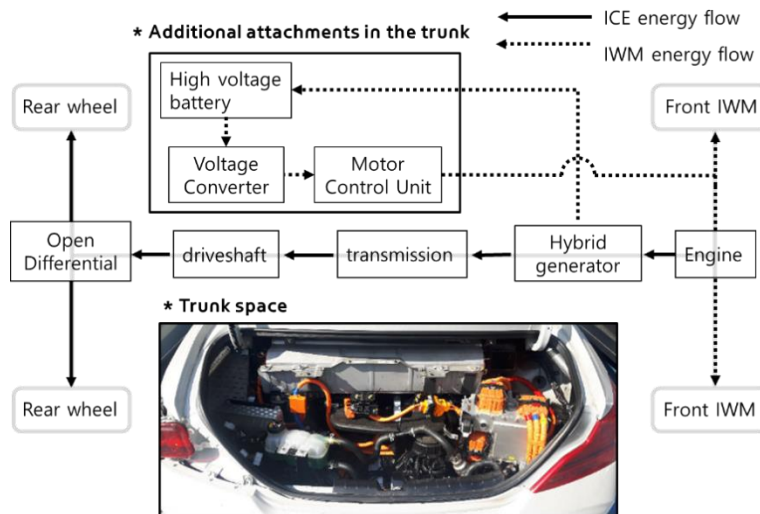


Figure 6.1. Test vehicle setup.

The signal block diagram of the test vehicle has been presented in Figure 6.2. The proposed control algorithm was implemented in the MicroAutobox (a

commercial product of Rapid Control Prototype) via an experimental computer. MicroAutobox receives vehicle status and transmits torque commands to the motor control units (MCUs) of each wheel via through Controller Area Network (CAN). Additionally, a Differential Global Positioning System (DGPS) has been equipped in the test vehicle, in order to measure the global position, longitudinal and lateral velocity of the test vehicle. All the measurements can then be transmitted to the CAN bus and recorded into the experimental computer from the CAN bus.

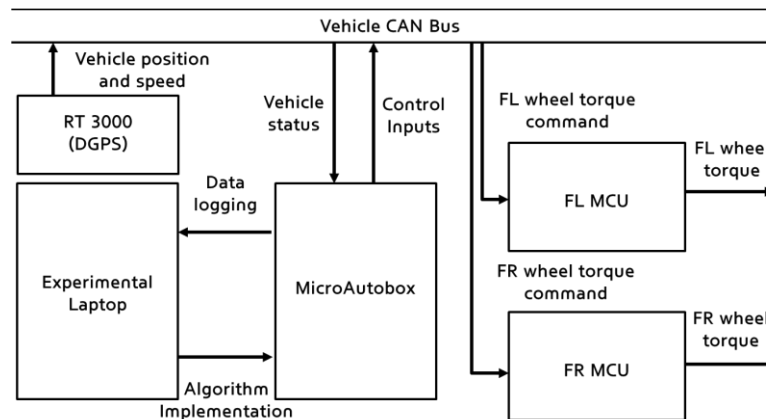


Figure 6.2. Block diagram of the test vehicle.

In the vehicle tests, two closed-loop test scenarios were adopted: 1) constant radius circular turn test; 2) double lane change test. The circular turn test was performed to investigate the steady-state cornering performance with the proposed algorithm. The double lane change test was conducted to examine the control performance at transient cornering. All vehicle tests were conducted on dry asphalt road surface. In both tests, a skilled human driver strived to manipulate the steering angle to follow the given path. Unlike the simulation results, the vehicle response with the proposed algorithm has been compared only to the uncontrolled vehicle

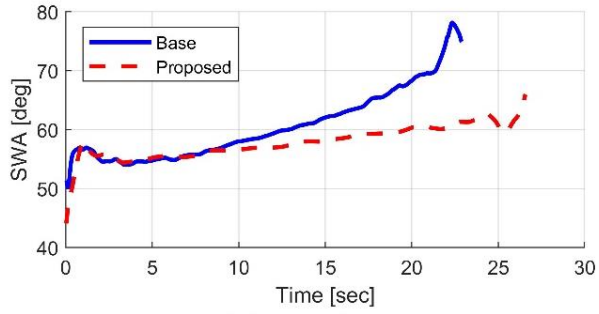


response that is an open-differential based rear wheel drive vehicle without in-wheel motor control. It is because the other yaw rate tracking algorithms (i.e., sliding mode control and integral sliding mode control) can give rise to safety issues due to the chattering problem if they are implemented within the test vehicle.

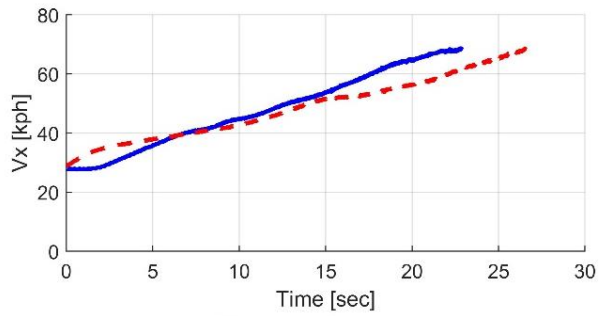
As aforementioned, the vehicle test scenario conducted first was the closed-loop circular turn test to evaluate the control performance at steady-state cornering. In this test, a human driver attempted to maintain a constant turning radius of 30m with a low longitudinal acceleration (i.e.,  $a_x < 0.1$ ), in order to reproduce the steady-state cornering with increasing the vehicle speed.

The overall test results, including the control inputs and understeer curve, are illustrated in Figure 6.3. As shown in Figures 6.3(b) and (d), the vehicle speed started from 25kph and went up to 65kph near the limits of handling. As shown in Figure 6.3(a), the steering angle with proposed algorithm was reduced compared to the uncontrolled case when the same turning radius and yaw rate were set as a vehicle test scenario. Additionally, the modified understeer characteristic can be confirmed in Figure 6.3(g), and understeer gradient of the test vehicle with the proposed algorithm has been reduced compared to the baseline vehicle, achieving the control objective of the proposed algorithm. In summary, compared to the uncontrolled case, the proposed algorithm can modify the understeer characteristics and steady-state yaw rate response, improving the vehicle agility.

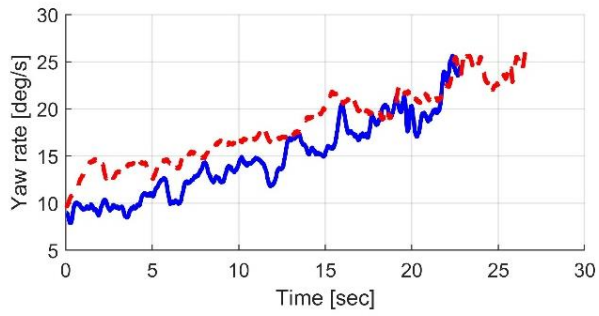
In particular, of the two control inputs (i.e., steady-state and transient control inputs), the steady-state control input contributes to improving the steady-state yaw rate response. The effects of the transient control input could also be investigated in the following vehicle test results.



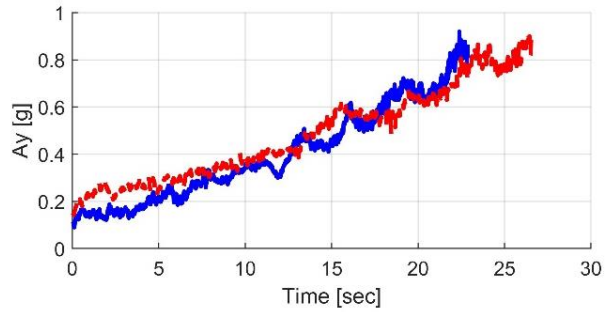
(a) Steering wheel angle



(b) Longitudinal velocity



(c) Yaw rate



(d) Lateral acceleration

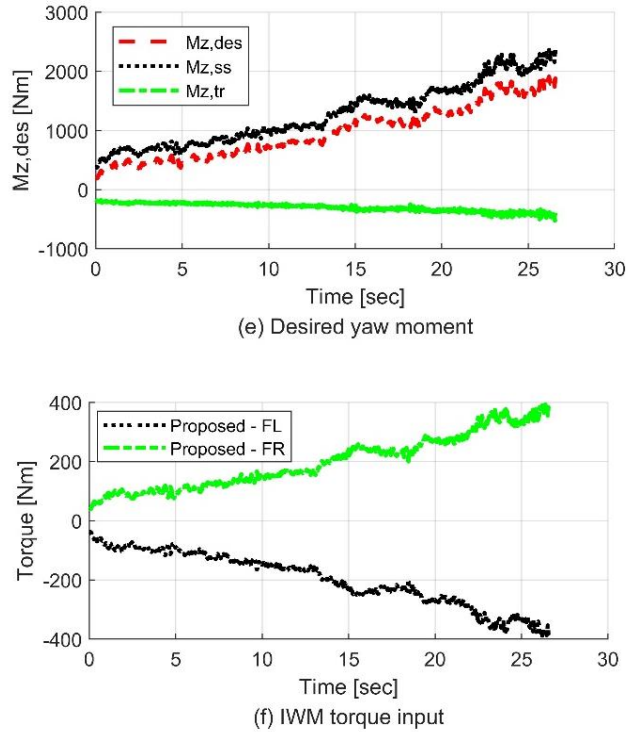
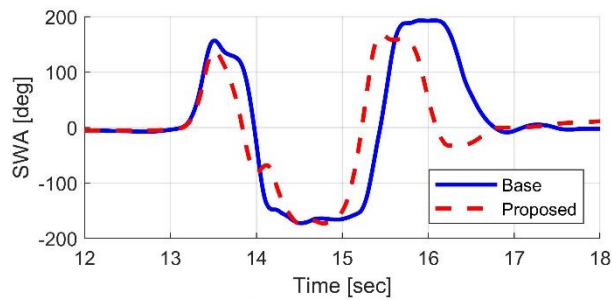


Figure 6.3. Vehicle test results for closed-loop circular turn.

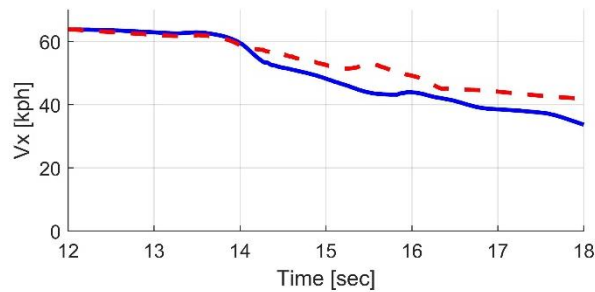
The second test scenario is the closed-loop double lane change test. This test scenario has been performed to investigate the control performance at transient cornering with severe maneuvers. A skilled human driver was instructed to navigate the given path without touching the cones at the path boundary. The initial entry speed was set to 65kph. Throttle and brake pedal inputs were not given to the vehicle during the scenario in order to exclude the effects of the drivers' pedal inputs for a consistent comparison. In order to investigate the vehicle response in severe maneuvers, the lateral acceleration was increased up to the handling limits, i.e.,  $a_y > 0.9g$ .

The overall vehicle states and control inputs have been shown in Figure 6.4. Figures 6.4(c) and (d) show that the proposed control algorithm can reduce the

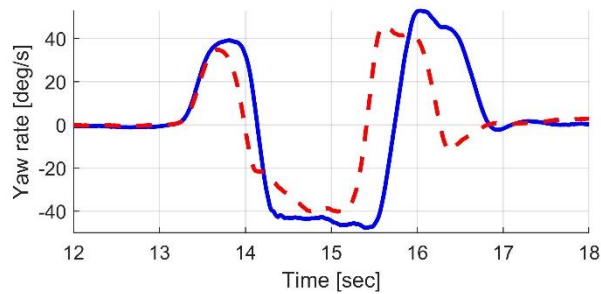
peak values of yaw rate and sideslip angle compared to the base vehicle. Additionally, since the sideslip angle is reduced by the proposed controller, the exit (final) vehicle speed was increased in the controlled vehicle, as shown in Figure 6.4(b). In summary, the proposed controller can improve the vehicle lateral stability with reducing the peak values of yaw rate and sideslip angle compared to the uncontrolled case. Additionally, it should be noted that the transient control input plays an important role in controlling the transient response of the test vehicle, as shown in Figure 6.4(e).



(a) Steering wheel angle



(b) Longitudinal velocity



(c) Yaw rate

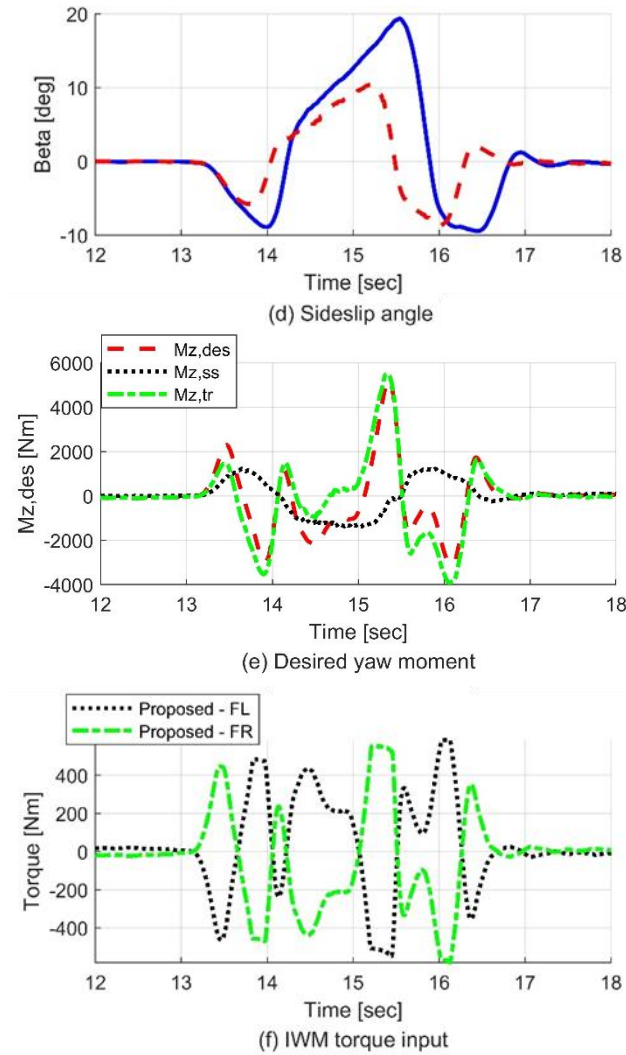


Figure 6.4. Vehicle test results for closed-loop double lane change test.

As can be seen from the vehicle test results so far, the proposed algorithm can enhance both the vehicle agility and stability in vehicle tests while achieving the goals of steady-state and transient control inputs, respectively.

In Section 4, a torque vectoring control for the two front in-wheel motors in a rear-wheel-drive vehicle has been proposed. The proposed algorithm consists of steady-state and transient control inputs. The steady-state control input can

improve the vehicle agility at steady-state cornering by decreasing the understeer gradient of a vehicle. The transient control input can improve the lateral stability by increasing the yaw rate damping coefficient to the steering input in a vehicle. The proposed algorithm has been investigated via both computer simulations and vehicle tests. Simulation results show that the proposed algorithm can enhance the cornering response by modifying the vehicle understeer gradient and yaw rate damping coefficient. In vehicle tests, vehicle response with proposed algorithm has been compared to the uncontrolled case, showing the superior control performance compared to the yaw rate tracking algorithm and uncontrolled case. One potential drawback comes from the sensitivity to the vehicle model uncertainty.

## 6.2. Test results for integrated control of IWM and eLSD

In order to investigate the performance of the proposed control algorithm in an actual vehicle, a test vehicle has been developed based on a front-engine rear-wheel-drive vehicle. As shown in Figure 6.5, two actuators are additionally installed in the test vehicle: 1) two front in-wheel motors (IWMs); 2) an electronic limited slip differential (eLSD) in the rear axle. Additionally, the block diagram of the test vehicle is illustrated in Figure 6.6. The proposed algorithm was implemented in the test vehicle using MicroAutobox with industrial computer. MicroAutobox receives the sensor signals and transmits the control inputs to the actuator ECU through Controller Area Network (CAN) communication. Differential Global Positioning System (DGPS) is additionally mounted in the test vehicle in order to measure the vehicle position and speed. All the measurements from the CAN bus were recorded in the industrial computer.

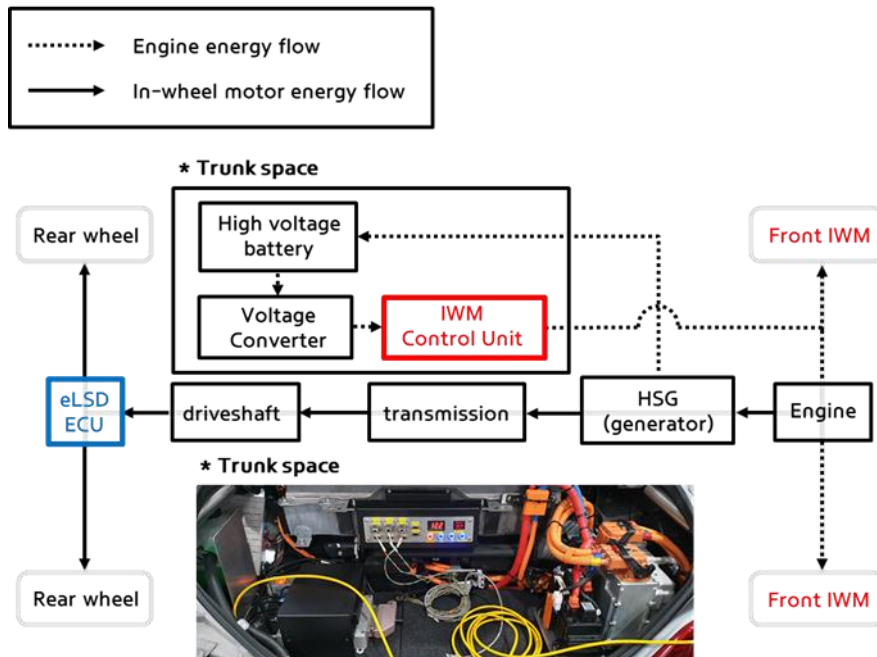


Figure 6.5. Test vehicle setup.

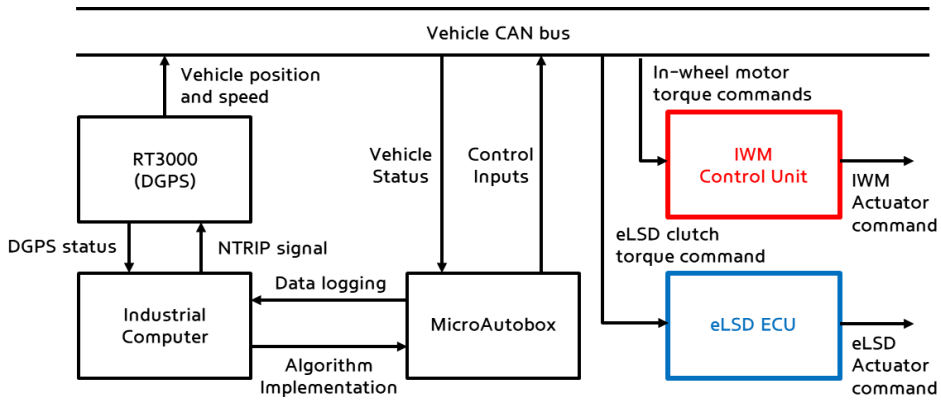


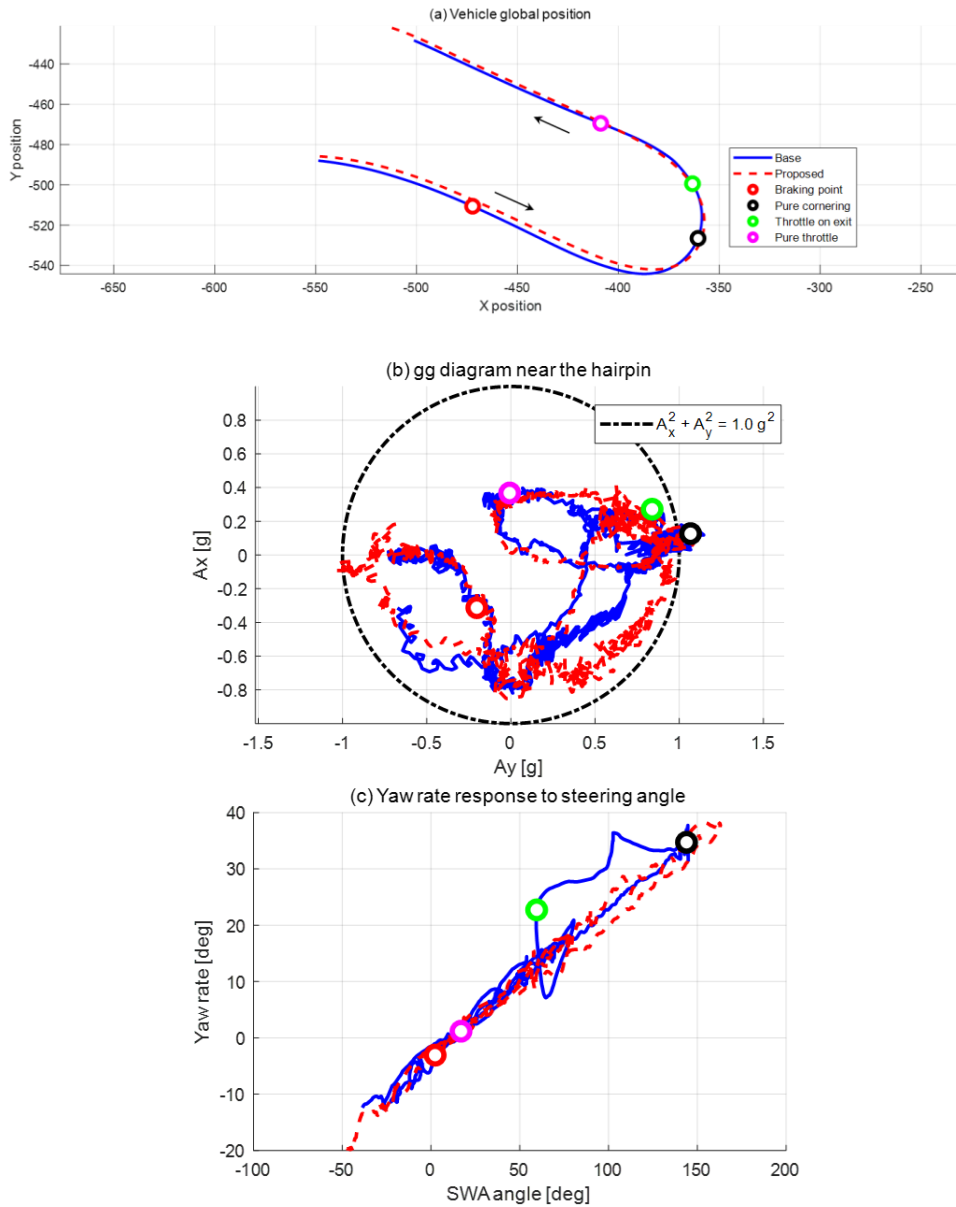
Figure 6.6. Block diagram of the test vehicle.

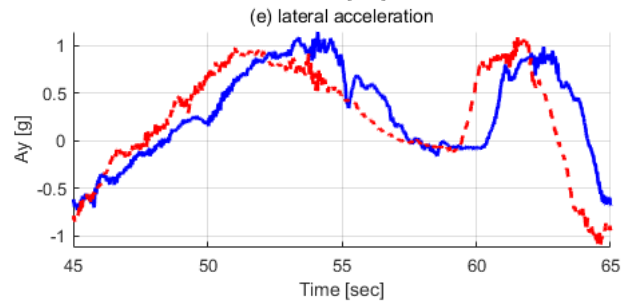
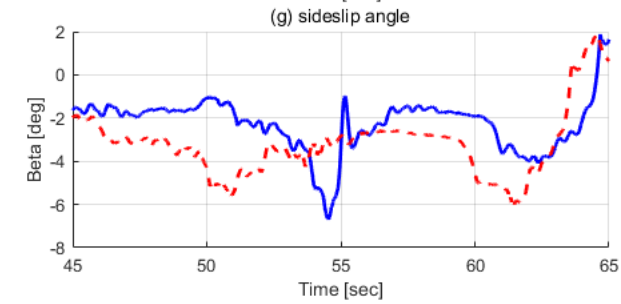
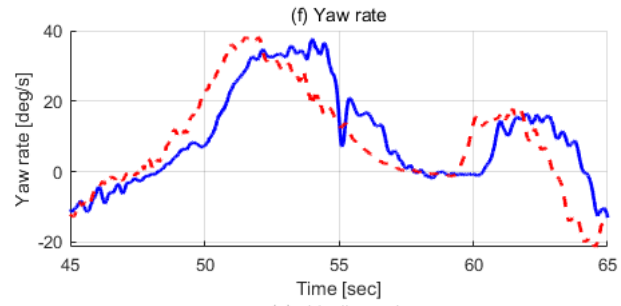
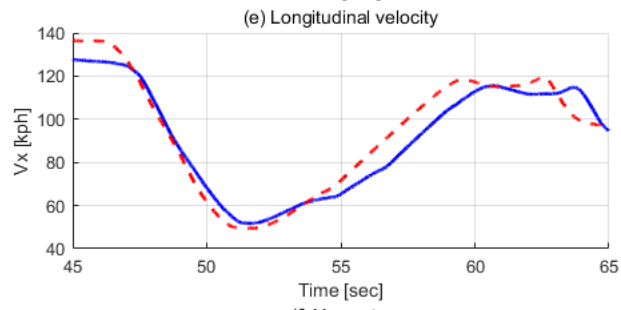
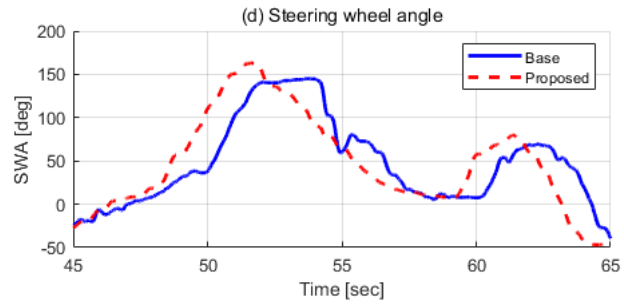
Figure 6.7 shows the vehicle test results near the hairpin corner on a racing track, as shown in Figure 6.7(a). A skilled human driver strived to navigate the hairpin corner for the fastest lap time. The performance of the integrated control can be directly shown in Figure 6.7(b) and (c). Figure 6.7(b) shows that the proposed controller can contribute to enlarging the available area of the g-g diagram, which means that tire friction can be used more efficiently compared to the base vehicle. Figure 6.7(c) presents the yaw rate response to the driver steering input, showing that proposed algorithm can maintain the linearity of the yaw rate response even near the limits of handling, while the base vehicle lose the linearity.

The overall vehicle states are presented in Figure 6.7(d)-(g). As shown in Figure 6.7(g), the base vehicle lost the lateral stability at 55sec, which corresponds to “Throttle on exit” point in Figure 6.7(a). At this moment, the test driver attempted to save the lateral stability via the counter-steering, as shown in Figure 6.7(d). However, the test results with proposed algorithm show the improved handling performance even in the same level of lateral acceleration. Additionally, compared



to the base vehicle, the test vehicle with the integrated control of IWMs and eLSD, can negotiate the hairpin corner with improved longitudinal acceleration performance, as shown in Figure 6.7(e).





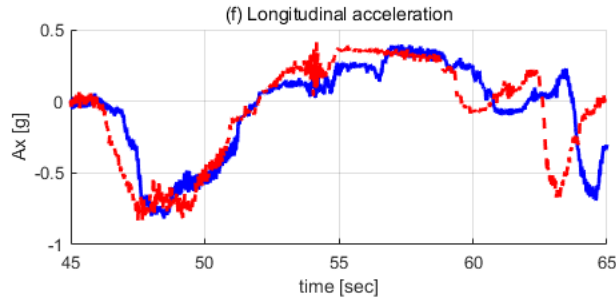


Figure 6.7. Vehicle test results on a racing track.

In Section 4, an integrated control of two front in-wheel motors (IWMs) and electronic limited slip differential (eLSD) is proposed. The proposed algorithm is designed to enhance the cornering performance at high speeds considering the actuator characteristics. Considering the actuator characteristics, the two front in-wheel motors are utilized to improve the steady-state and transient cornering responses based on a feedforward control, and the electronic limited slip differential is utilized to track the target yaw rate based on a feedback control. In computer simulations, the control performance for each actuator is investigated based on two simulation scenarios to mimic the aggressive cornering conditions with longitudinal acceleration and deceleration. Additionally, the step steer maneuver was conducted to show the effects of each actuator on yaw rate overshoot. In vehicle tests on a racing track, the vehicle response with proposed controller shows the improved limit handling performance near the hairpin corner compared to the base vehicle. One potential drawback is that the feedforward control by two front in-wheel motors is vulnerable to the model uncertainties at handling limits.

# Chapter 7 Conclusion

This dissertation has proposed a torque vectoring control using in-wheel motors (IWMs) and integrated control with other chassis modules, such as electronic limited slip differential (eLSD) and rear wheel steering (RWS), in order to improve cornering performance. In particular, the main scope addressed in this dissertation can be arranged in the following three cases: 1) individual control of in-wheel motor (IWM); 2) integrated control of in-wheel motor (IWM) and electronic limited slip differential (eLSD);

Firstly, the individual control of in-wheel motors consists of steady-state and transient control input. The steady-state control input is devised to improve the steady-state cornering response with modifying the vehicle understeer gradient, and the transient control input is designed to enhance the lateral stability by increasing the yaw rate damping coefficient. The proposed algorithm has been investigated through both computer simulations and vehicle tests, in order to show that the proposed algorithm can enhance the cornering response achieving the control objectives and to show the superior control performance compared to the yaw rate tracking algorithm and uncontrolled case.

Secondly, the integrated control of two front in-wheel motors (IWMs) and electronic limited slip differential (eLSD) is designed to enhance the cornering performance at high speeds considering the characteristics of each actuator. The two front in-wheel motors (IWMs) are controlled to improve cornering performance based on a feedforward control, and the electronic limited slip

differential (eLSD) is utilized for the yaw rate feedback control. The computer simulations were conducted to show the effects of each actuator on vehicle lateral motion at aggressive cornering with longitudinal acceleration and deceleration. Additionally, vehicle test results show that the proposed controller can improve the cornering performance at the limits of handling compared to the uncontrolled case.

In summary, this dissertation proposes a control algorithm for enhanced limit handling performance based on vehicle understeer gradient and yaw rate damping characteristics, addressing also an integrated control of in-wheel motors and electronic limited slip differential with considering the characteristics of each actuator. The proposed in-wheel motor control law is formulated to shape the understeer characteristics during steady-state cornering and yaw rate damping characteristic during transient cornering, and the eLSD control is designed to track the reference yaw rate. Vehicle tests have been conducted to validate the control performance of the proposed algorithm, showing significant improvements in the agility and stability of a test vehicle without chattering issues. Additionally, the vehicle tests at a racing track presents the enhanced limit handling performance.

Some potential drawbacks of the proposed approach come from the vehicle and tire model uncertainty, primarily due to tire response at wheel slip and banked road. For example, excessive wheel slip and roll angle would result in an inaccurate estimation of cornering stiffness. A torque vectoring control robust to these model errors and uncertainties would be the future research topic.

# Appendix A. Integrated control of two front in-wheel motors and rear wheel steering

This appendix addresses an integrated control of torque vectoring and rear wheel steering using model predictive control (MPC). The control objective of the proposed MPC is to minimize both the yaw rate and body side slip angle errors without chattering issues. The proposed model predictive controller is designed based on a linear parameter varying (LPV) vehicle model. The vehicle model parameters are estimated in real time and applied in the LPV vehicle model. The performance of the proposed controller has been investigated and compared with the uncontrolled case. The simulation results show that the integrated control of torque vectoring and rear wheel steering can improve the lateral stability and handling performance of vehicles.

Among the various chassis modules, the integration of torque vectoring and rear wheel steering is the main scope of this appendix. The torque vectoring devices can split the different wheel torques in left and right wheels, and rear wheel steering system can improve the vehicle lateral motion by allocating the additional steering input in the rear wheels. Since both the two system, i.e., torque vectoring and rear wheel steering, affects the lateral motion of vehicles, it is important to coordinate the two control inputs considering the effects of each system.

Designing a model predictive control (MPC) can be a methodology to handle these issues. The main advantage of the model predictive control is to predict the effects of each control input on the lateral motion based on a vehicle model, and to be utilized for integrated control of multiple modules considering the influences of

each module [Ataei'20, Borrelli'17].

The purpose of this study is to design the integrated control of torque vectoring and rear wheel steering and improve the cornering performance using the proposed controller. The control objective is to minimize the errors of yaw rate and sideslip angle. Additionally, the reference trajectory is devised to prevent the yaw rate overshoot in the transient response. In order to prevent the chattering, the penalty function for the change of control inputs is added in the cost function. In order to confirm the control performance, computer simulation has been conducted using the Carsim and Simulink software. Two simulation scenarios are conducted to investigate the control performance: 1) Open-loop sine with dwell and 2) Closed-loop double lane change. The simulation results show that the proposed algorithm can improve the cornering performance compared to the uncontrolled case.

## A.1. Prediction model for vehicle motion

Before introducing the proposed MPC algorithm, it is necessary to explain the target vehicle architecture and vehicle model that were considered to design the proposed algorithm. As shown in Figure A.1(a), the architecture of the target vehicle is a rear wheel drive vehicle additionally equipped with two chassis modules: 1) two front in-wheel motors and 2) rear wheel steering system. The lateral motion of vehicles can be described based on a three-degree-of-freedom (3-DOF) planar model and a bicycle model [Gillespie'92, Rajamani'11], as shown in Figure A.1(b).

In order to design a model predictive control (MPC), the bicycle model [Rajamani'11] is adopted to design the MPC algorithm. It is because the bicycle

model can express the direct yaw moment and additional rear wheel force as a control input vector. Additionally, a linear parameter varying model for MPC algorithm can be defined using the bicycle model, inducing the reduced calculation time compared to nonlinear models.

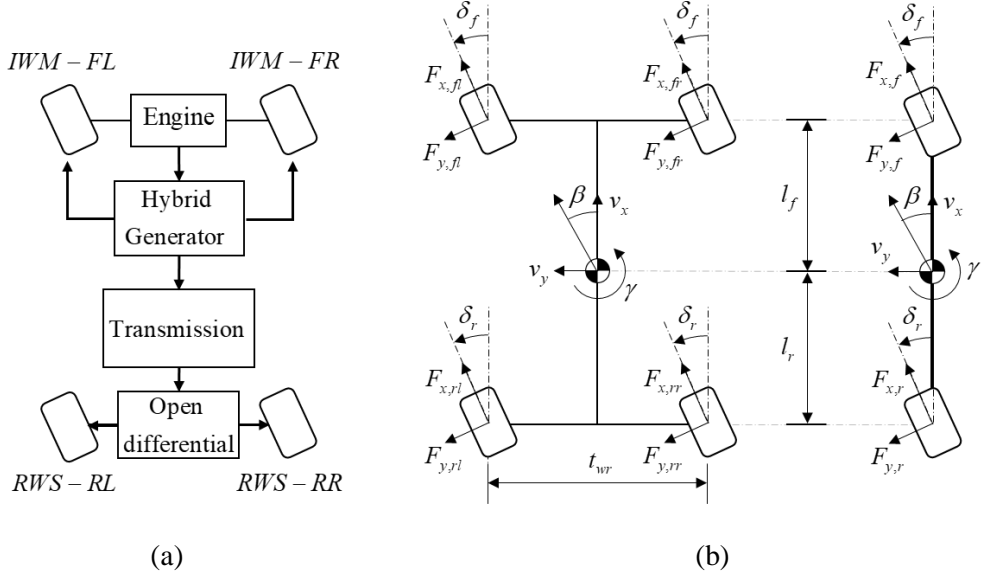


Figure A.1. (a) Target vehicle architecture and (b) 3-DOF planar model and bicycle model.

The controller design of the proposed MPC algorithm is based on the 2DOF bicycle model [Rajamani'11]. In this model, the longitudinal vehicle speed can be assumed to be constant, and the tire model can be linearized for design simplicity. Based on these assumptions, the lateral motion can be described in the bicycle model with additional lateral forces by rear wheel steering and additional yaw moment by torque vectoring as follows:

$$mv_x(\dot{\beta} + \dot{\gamma}) = F_{y,f} + (F_{y,r} + \Delta F_{y,r}), \quad (\text{A.1a})$$

$$I_z \dot{\gamma} = l_f F_{y,f} - l_r (F_{y,r} + \Delta F_{y,r}) + \Delta M_z, \quad (\text{A.1b})$$



where  $\Delta F_{y,r}$  is the additional lateral tire force of rear wheels to be generated by additional rear wheel steering input;  $\Delta M_z$  is the additional yaw moment by torque vectoring devices. In the above equations, the lateral forces, for small slip angle, can be linearized as follows:

$$F_{y,f} = C_r \left( \delta_f - \beta - \frac{l_f}{v_x} \gamma \right), \quad (\text{A.2a})$$

$$F_{y,r} = C_r \left( -\beta + \frac{l_r}{v_x} \gamma \right), \quad \Delta F_{y,r} = C_r \delta_r, \quad (\text{A.2b})$$

Substituting the Equations (A.2a)-(A.2b) into Equations (A.1a)-(A.1b), the slightly modified bicycle model can be derived as follows:

$$\frac{dx(t)}{dt} = Ax(t) + B_{\delta_f} \delta_f(t) + B_u u(t)$$

where  $x = [\beta, \gamma]^T$ ,  $u = [\Delta F_{y,r}, \Delta M_z]^T$ ,

$$A = \begin{bmatrix} -\frac{C_f + C_r}{mv_x} & \frac{C_r l_r - C_f l_f}{mv_x^2} - 1 \\ \frac{C_r l_r - C_f l_f}{I_z} & -\frac{C_f l_f^2 + C_r l_r^2}{I_z v_x} \end{bmatrix}, \quad (\text{A.3})$$

$$B_{\delta_f} = \begin{bmatrix} \frac{C_f}{mv_x} \\ \frac{C_f l_f}{I_z} \end{bmatrix}, \quad B_u = \begin{bmatrix} \frac{1}{mv_x} & 0 \\ -\frac{l_r}{I_z} & \frac{1}{I_z} \end{bmatrix},$$

In the above model, the tire model parameters are estimated in real time using the estimators shown in Equations (19) and (20) of Section 3.1.1.

The vehicle model in Equation (A.3) can be rearranged in continuous-time state-space model as follows:

$$\begin{aligned}
\frac{dx}{dt} &= A_c x + B_{1,c} u + B_{2,c} d, \\
x &= [\beta \quad \gamma]^T, \quad u = [\Delta F_{y,r} \quad \Delta M_z]^T, \quad d = \delta_f, \\
A &= \begin{bmatrix} -\frac{C_f + C_r}{mv_x} & \frac{C_r l_r - C_f l_f}{mv_x^2} - 1 \\ \frac{C_r l_r - C_f l_f}{I_z} & -\frac{C_f l_f^2 + C_r l_r^2}{I_z v_x} \end{bmatrix}, \\
B_{1,c} &= \begin{bmatrix} \frac{1}{mv_x} & 0 \\ -\frac{l_r}{I_z} & \frac{1}{I_z} \end{bmatrix}, \quad B_{2,c} = \begin{bmatrix} \frac{C_f}{mv_x} \\ \frac{C_f l_f}{I_z} \end{bmatrix},
\end{aligned} \tag{A.4}$$

The above continuous-time state-space model can be transformed into a discrete time form using the Euler method as follows:

$$x_{k+1} = A_d x_k + B_{1,d} u_k + B_{2,d}, \tag{A.5a}$$

$$A_d = (I + t_s A_c), \quad B_{1,d} = t_s B_{1,c}, \quad B_{2,d} = t_s B_{2,c}, \tag{A.5b}$$

$$\text{where } x_k = [\beta_k \quad \gamma_k]^T,$$

Based on the above discrete model, the proposed MPC has been designed to obtain the optimal control input  $u = [\Delta F_{y,r} \quad \Delta M_z]^T$ .

The obtained optimal control inputs are converted into the wheel torques and rear wheel steering angle in the lower-level controller to be introduced later based on the following equations:

$$\Delta M_z = \frac{t_{wf}}{2} (F_{x,fr} - F_{x,fl}), \quad F_{x,fl} + F_{x,fr} = 0, \tag{A.6a}$$

$$T_{fl} = r_{eff} F_{x,fl}, \quad T_{fr} = r_{eff} F_{x,fr}, \tag{A.6b}$$

$$F_{y,r} = \hat{C}_r \left( \delta_r - \frac{v_y - l_r \gamma}{v_x} \right), \quad \Delta F_{y,r} = C_r \hat{\delta}_r, \tag{A.6c}$$

As shown in the above equations, the absolute values of torque inputs for the front-left and front-right wheels are equivalent. Additionally, the additional lateral force can be expressed as a linear relationship with additional rear wheel steering angle.

The wheel torque and rear wheel steering angle inputs can be expressed as follows:

$$T_{fl,cmd} = -\frac{2r_{eff}}{t_{wfl}} \Delta M_z, \quad T_{fr,cmd} = \frac{2r_{eff}}{t_{wfr}} \Delta M_z, \quad \delta_{r,cmd} = \frac{\Delta F_{y,r}}{\hat{C}_r}, \quad (\text{A.7})$$

The cornering stiffness for rear axle is estimated using the method already introduced in Equations (19) and (20) of Section 3.1.1.

## A.2. Controller design

In order to design the controller using the model predictive control, the discretized model in Equations (A.5a)-(A.5b) has been utilized. As aforementioned, the control objective of the proposed controller is to minimize the yaw rate and side slip angle errors. Additionally, in order to prevent the control input chattering problem, the penalty function with respect the change of control inputs has been added in the cost function. Lastly, in order to prevent the excessive control at transient response, the convergence trajectory models for the errors of yaw rate and sideslip angle was devised.

The integrated control of two front in-wheel motors and rear wheel steering consists of three parts, as shown in Figure A.2. Firstly, the reference trajectory generates the future temporal path reaching the desired set-point (i.e.,  $\beta_{des}$  and  $\gamma_{des}$ ) to be tracked by the proposed algorithm. Secondly, the MPC based upper-level controller calculates the desired yaw moment and additional rear tire force to track the desired set point. Lastly, the lower-level controller converts the desired yaw moment and additional rear tire force to the torque inputs for two front in-wheel motors and rear wheel steering angle inputs.

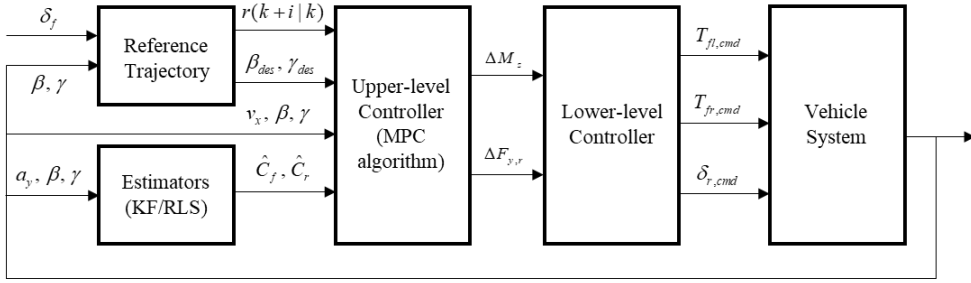


Figure A.2. Block diagram for the integrated control of in-wheel motors and rear wheel steering.

As shown in Figure A.3, the reference trajectory represents the temporal path in future steps to reach the desired set-point value [Richalet'09]. Particularly, the desired set-point stands for the desired yaw rate and sideslip angle, i.e.,  $\beta_{des}$  and  $\gamma_{des}$ . The reference trajectory can be interpreted as a desired closed-loop response in a set-point changing system. Thus, it is assumed that the reference trajectory converges on the desired set-point whether the set-point is constant or not. The reference trajectory is recalculated at each step using the current measurements in order to ensure the closed-loop. This is because the model output will be disturbed and the future prediction would not coincide with the actual output.

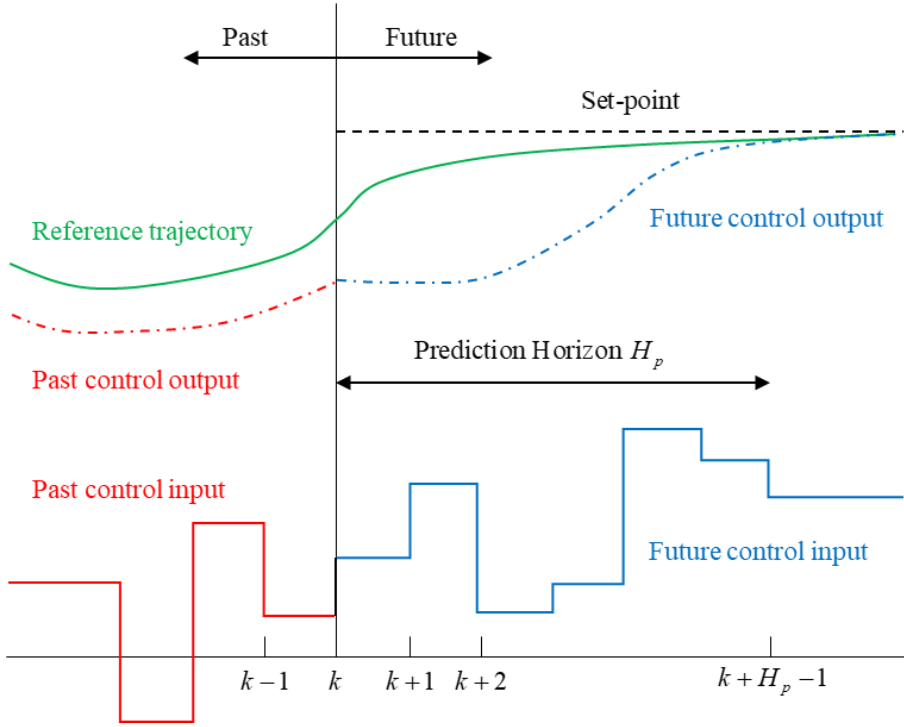


Figure A.3. Concept of the reference trajectory.

The desired values for the yaw rate and sideslip angle can be determined based on the bicycle model under the assumption of steady-state cornering as follows:

$$\gamma_{des} = \frac{v_x}{L + K_{us,des} v_x^2} \cdot \delta_f, \quad (\text{A.8a})$$

$$\beta_{des} = \frac{1}{L + K_{us,des} v_x^2} \left( l_r - \frac{l_f}{2C_r L} m v_x^2 \right) \cdot \delta_f \quad (\text{A.8b})$$

where  $K_{us,des}$  is the desired understeer gradient. The desired yaw rate and side slip angle can be defined as a set-point vector as follows:

$$s(k) = \begin{bmatrix} \beta_{des} \\ \gamma_{des} \end{bmatrix}, \quad (\text{A.9})$$

A reference trajectory can be calculated at each step from the current vehicle states

$x(k) = [\beta \ \gamma]^T$  and the set point  $s(k) = [\beta_{des} \ \gamma_{des}]^T$  as follows:

$$\begin{bmatrix} r(k+1|k) \\ r(k+2|k) \\ \vdots \\ r(k+H_p|k) \end{bmatrix} = \begin{bmatrix} I - \Lambda \\ I - \Lambda^2 \\ \vdots \\ I - \Lambda^{H_p} \end{bmatrix} \cdot s(k) + \begin{bmatrix} \Lambda \\ \Lambda^2 \\ \vdots \\ \Lambda^{H_p} \end{bmatrix} \cdot x(k), \quad (\text{A.10a})$$

$$\Lambda = \text{diag} \left[ \exp(\tau_s / \tau_{ref,1}), \exp(\tau_s / \tau_{ref,2}) \right], \quad (\text{A.10b})$$

where  $\Lambda$  represents an exponential convergence rate from current state  $x(k)$  to the set point  $s(k)$  based on the time constants [Maciejowski'02], i.e.,  $\tau_s$ ,  $\tau_{ref,1}$ , and  $\tau_{ref,2}$ . The time constants in Equation (A.10b) can adjust the convergence rate to the desired vehicle states, i.e.,  $\beta_{des}$  and  $\gamma_{des}$ .

The vehicle lateral motion control can be formulated as a finite-time constrained optimization problem [Borrelli'17]. The cost function for the minimization of yaw rate and side slip angle errors can be formulated as follows [Maciejowski'02]:

$$\min J = \sum_{i=1}^{H_p} \|x(k+i|k) - r(k+i|k)\|_{Q(i)}^2 + \sum_{i=0}^{H_p-1} \|\Delta u(k+i|k)\|_{R(i)}^2, \quad (\text{A.11a})$$

$$\text{subject to } x(k+i+1|k) = A_d x(k+i|k) + B_{1,d} u(k+i|k) + B_{2,d} d, \quad (\text{A.11b})$$

Equation (A.11a) denotes that the tracking error vector  $x(k+i|k) - r(k+i|k)$  and changes in the input  $\Delta u(k+i|k) = u(k+i+1|k) - u(k+i|k)$  are penalized at every point according to the weight matrices  $Q(i)$  and  $R(i)$ , respectively.  $H_p$  is the number of prediction horizon to be considered in the optimization. In this study, the optimal solution is obtained using CVXGEN software [Mattingley'12]. The first element, among the obtained control input sequence, is applied to the system [Borrelli'17].

### A.3. Simulation results

In order to investigate performance of the proposed algorithm, two simulation

scenarios are conducted as follows: 1) Open-loop sine with dwell and 2) Closed-loop double lane change. The two scenarios are adopted to study the control effects on lateral motion at transient cornering. The computer simulations for the validation of controller performance have been conducted for a rear wheel drive E-segment sedan that equipped with two additional actuators: 1) two front in-wheel motors (IWMs) and 2) rear wheel steering (RWS). The proposed algorithm has been implemented in computer simulations using Carsim and Simulink software. The vehicle parameters utilized in the simulations are arranged in Table A.1.

Table A.1. Vehicle parameters.

Vehicle parameter	Symbol	Value	Unit
Vehicle mass	$m$	1960	kg
Yaw moment of inertia	$I_z$	4660	kg·s <sup>2</sup>
CG to front axle distance	$l_f$	1.32	m
CG to rear axle distance	$l_r$	1.52	m
Track width of front axle	$t_{wf}$	1.63	m
Track width of rear axle	$t_{wr}$	1.65	m
Height of CG	$h_{CG}$	0.57	m
Effective radius	$r_{eff}$	0.332	m

In order to show the control performance of the proposed algorithm, the open-loop sine with dwell is conducted on a dry asphalt surface. In this scenario, the open-loop steering input is given to the vehicle. The initial vehicle speed was set to 100kph with no braking and accelerating during the maneuvers. The road-tire friction coefficient is 1.0 in the simulations. The vehicle motion with proposed controller is compared with the uncontrolled case.

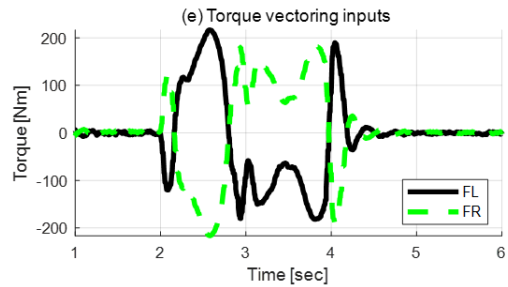
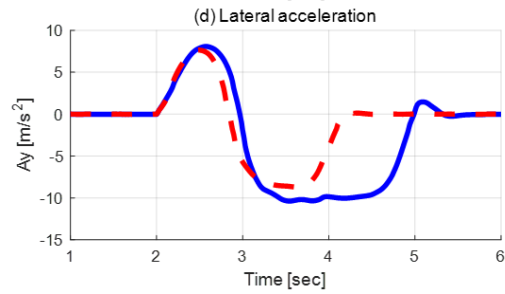
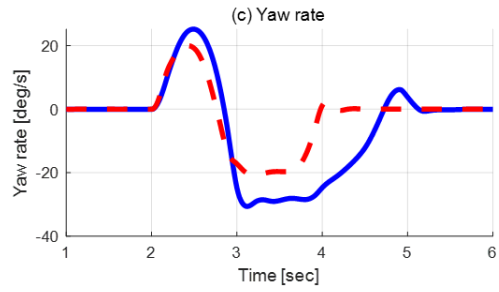
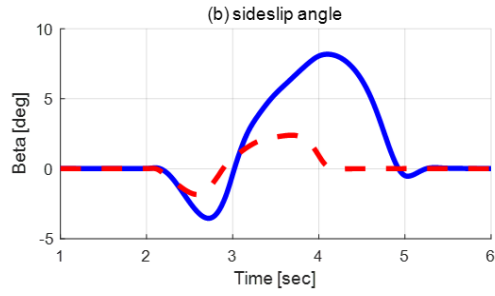
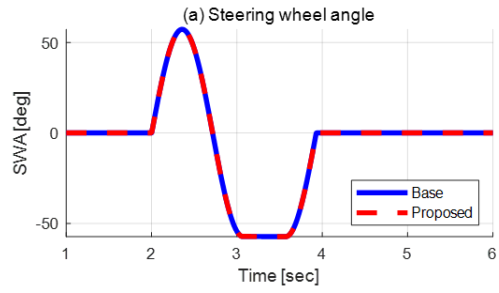






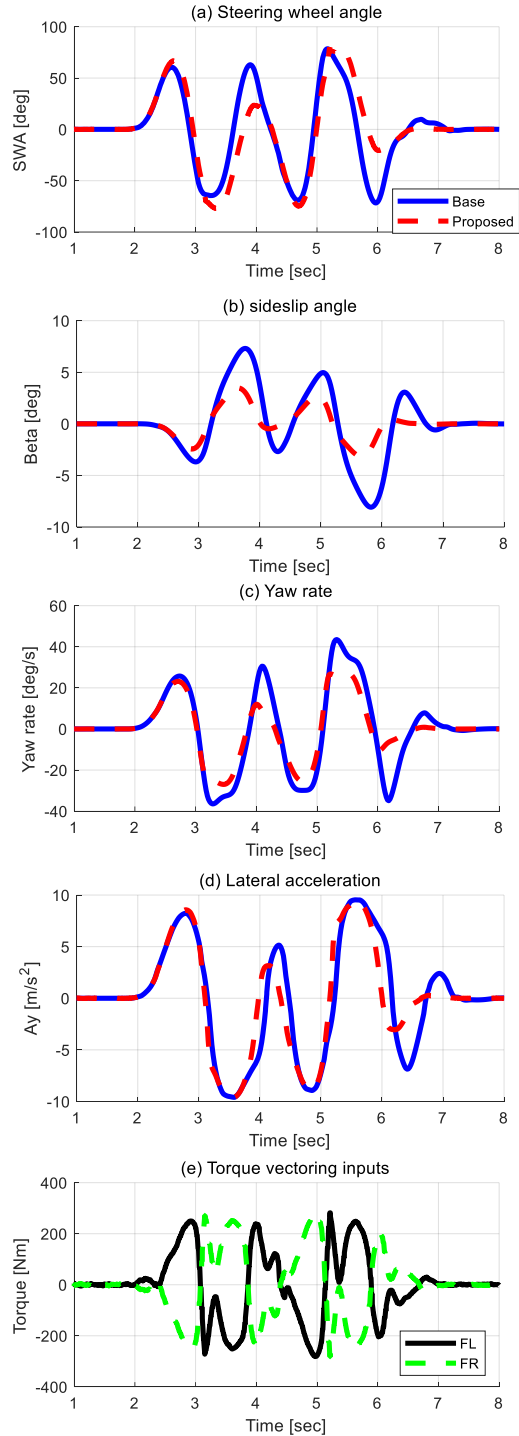
Figure A.4. Open-loop sine with dwell at 100kph.

Figure A.4 presents the simulation results for the open-loop sine with dwell scenario. Figure A.4(a)-(d) shows the vehicle states, and Figure A.4(e) and (f) addresses the control inputs for two front in-wheel motors and rear wheel steering system. The control inputs in Figure A.4(e) and (f) correspond to the additional front wheel torques and rear wheel steering angles.

As shown in Figure A.4(a), the vehicle speed is set to 100kph and open-loop steering input is given to the vehicle, equivalently in the comparison. Figure A.4(b) compares the sideslip angles between the uncontrolled case and controlled case with proposed MPC algorithm, showing the reduced sideslip angle due to the control algorithm. Additionally, as shown in Figure A.4(c), the proposed algorithm also can enhance the yaw rate response. These results show that the proposed algorithm can improve the lateral motion compared to the uncontrolled case. In summary, in the open-loop scenario, the proposed algorithm can improve the cornering performance with enhanced responses of yaw rate and sideslip angle.

Additionally, in order to show the controller performance in severe maneuvers, closed-loop double lane change scenario is conducted. In this scenario, a path following model [Guo'93] is applied to reproduce the drivers' steering input to track the given path. The initial vehicle speed and tire-road friction coefficient are

set to 100kph and 1.0, respectively. In this scenario, the vehicle responses of controlled and uncontrolled cases are compared together.



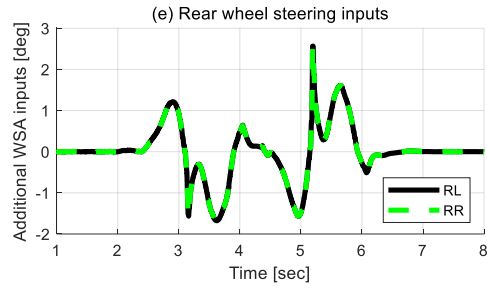


Figure A.5. Closed-loop double lane change at 100kph.

The simulation results for the closed-loop double lane change scenario are shown in Figure A.5. Similarly in the previous simulation results, Figure A.5(a)-(d) corresponds to the vehicle states, and Figure A.5(e)-(f) shows the additional torque inputs and rear wheel steering angle inputs.

As shown in Figure A.5(a), it can be confirmed that the counter-steering inputs is reduced at around 4sec and 6sec. Additionally, as shown in Figure A.5(b) and (c), the yaw rate and sideslip angle responses are stabilized with the proposed algorithm compared to the uncontrolled maneuver. Particularly, between 6sec and 6.5sec, the proposed controller can improve the oversteering motion. Through the simulation results, it is shown that the proposed control algorithm can improve the lateral stability and cornering performance even in the closed-loop scenario.

In this appendix, an integrated control of torque vectoring and rear wheel steering based on the model predictive control has been proposed. The control objective of the proposed algorithm is to minimize the errors of yaw rate and sideslip angle, enhancing the cornering performance. In order to design a model predictive control, a reference trajectory has been devised to adjust the convergence rate to the references for yaw rate and sideslip angle. The proposed algorithm has been validated via two simulation scenarios: 1) Open-loop sine with

dwel; 2) Closed-loop double lane change. Simulation results show that the proposed algorithm can improve the vehicle responses for yaw rate and sideslip angle.

# Bibliography

- Piyabongkarn, D., Lew, J. Y., Rajamani, R., & Grogg, J. A. (2010). Active driveline torque-management systems. *IEEE Control Systems Magazine*, 30(4), 86-102.
- Murata, S. (2012). Innovation by in-wheel-motor drive unit. *Vehicle System Dynamics*, 50(6), 807-830.
- Watts, A., Vallance, A., Whitehead, A., Hilton, C., & Fraser, A. (2010). The Technology and Economics of In-Wheel Motors. *SAE Int. J. Passeng. Cars - Electron. Electr. Syst.* 3(2), 37-57.
- Piyabongkarn, D., Lew, J. Y., Rajamani, R., Grogg, J. A., & Yuan, Q. (2007). On the use of torque-biasing systems for electronic stability control: Limitations and possibilities. *IEEE Transactions on Control Systems Technology*, 15(3), 581-589.
- Hancock, M. J., Williams, R. A., Fina, E., & Best, M. C. (2007). Yaw motion control via active differentials. *Transactions of the Institute of Measurement and Control*, 29(2), 137-157.
- Cha, H., Hyun, Y., Yi, K., & Park, J. (2022). An integrated control of front in-wheel motors and rear electronic limited slip differential for high-speed cornering performance. *Proceedings of the Institution of Mechanical Engineers, Part D: Journal of Automobile Engineering*, 236(7), 1355-1374.
- Park, K., Joa, E., Yi, K., & Yoon, Y. (2020). Rear-Wheel Steering Control for Enhanced Steady-State and Transient Vehicle Handling Characteristics. *IEEE Access*, 8, 149282-149300.
- Kaiser, G., Holzmann, F., Chretien, B., Korte, M., & Werner, H. (2011, June). Torque vectoring with a feedback and feed forward controller-applied to a through the road hybrid electric vehicle. In *2011 IEEE intelligent vehicles symposium (IV)* (pp. 448-453). IEEE.
- Geng, C., Mostefai, L., Denai, M., & Hori, Y. (2009). Direct yaw-moment control of an in-wheel-motored electric vehicle based on body slip angle fuzzy observer. *IEEE Transactions on Industrial Electronics*, 56(5), 1411-1419.
- Nam, K., Fujimoto, H., & Hori, Y. (2015). Design of an adaptive sliding mode controller for robust yaw stabilisation of in-wheel-motor-driven electric vehicles. *International Journal of Vehicle Design*, 67(1), 98-113.

- Zhang, S., Ding, S., & Jiang, H. (2016, March). Direct yaw-moment control of in-wheel electric vehicle by sliding mode technique. In 2016 IEEE International Conference on Industrial Technology (ICIT) (pp. 1844-1849). IEEE.
- Park, G., Han, K., Nam, K., Kim, H., & Choi, S. B. (2020). Torque vectoring algorithm of electronic-four-wheel drive vehicles for enhancement of cornering performance. *IEEE Transactions on Vehicular Technology*, 69(4), 3668-3679.
- Rubin, D., & Arogeti, S. A. (2015). Vehicle yaw stability control using active limited-slip differential via model predictive control methods. *Vehicle System Dynamics*, 53(9), 1315-1330.
- Nagai, M., Hirano, Y., & Yamanaka, S. (1997). Integrated control of active rear wheel steering and direct yaw moment control. *Vehicle System Dynamics*, 27(5-6), 357-370.
- Lee, S. H., Lee, U. K., Ha, S. K., & Han, C. S. (1999). Four-wheel independent steering (4WIS) system for vehicle handling improvement by active rear toe control. *JSME International Journal Series C Mechanical Systems, Machine Elements and Manufacturing*, 42(4), 947-956.
- Eguchi, T., Sakita, Y., Kawagoe, K., Kaneko, S., Mori, K., & Matsumoto, T. (1989). Development of " Super Hicas", a New Rear Wheel Steering System with Phasereversal Control. *SAE transactions*, 98, 1495-1504.
- Warth, G., Frey, M., & Gauterin, F. (2020). Design of a central feedforward control of torque vectoring and rear-wheel steering to beneficially use tyre information. *Vehicle System Dynamics*, 58(12), 1789-1822.
- Her, H., Joa, E., Yi, K., & Kim, K. (2016). Integrated chassis control for optimized tyre force coordination to enhance the limit handling performance. *Proceedings of the Institution of Mechanical Engineers, Part D: Journal of Automobile Engineering*, 230(8), 1011-1026.
- Yim, S. (2021). Integrated chassis control with four-wheel independent steering under constraint on front slip angles. *IEEE Access*, 9, 10338-10347.
- Vignati, M., & Sabbioni, E. (2022). A cooperative control strategy for yaw rate and sideslip angle control combining torque vectoring with rear wheel steering. *Vehicle System Dynamics*, 60(5), 1668-1701.
- Cho, W., Choi, J., Kim, C., Choi, S., & Yi, K. (2012). Unified chassis control for the improvement of agility, maneuverability, and lateral stability. *IEEE Transactions on vehicular Technology*, 61(3), 1008-1020.

- Kim, K., Kim, B., Go, Y., Park, J., Park, J., Suh, I., & Yi, K. (2014). An investigation on motor-driven power steering-based crosswind disturbance compensation for the reduction of driver steering effort. *Vehicle System Dynamics*, 52(7), 922-947.
- Yim, S. (2020). Comparison among Active Front, Front Independent, 4-Wheel and 4-Wheel Independent Steering Systems for Vehicle Stability Control. *Electronics*, 9(5), 798.
- Ariff, M.H., Zamzuri, H., Nordin, M.A., Wira, J.B., Mazlan, S.A., & Rahman, M.A. (2015). Optimal control strategy for low speed and high speed four-wheel-active steering vehicle. *Journal of Mechanical Engineering and Sciences*, 8, 1516-1528.
- Yu, S., Wang, J., Wang, Y., & Chen, H. (2016). Disturbance observer based control for four wheel steering vehicles with model reference. *IEEE/CAA Journal of Automatica Sinica*, 5(6), 1121-1127.
- Nam, K., Fujimoto, H., & Hori, Y. (2012). Lateral stability control of in-wheel-motor-driven electric vehicles based on sideslip angle estimation using lateral tire force sensors. *IEEE Transactions on Vehicular Technology*, 61(5), 1972-1985.
- Peters, Y., & Stadelmayer, M. (2019). Control allocation for all wheel drive sports cars with rear wheel steering. *Automotive and Engine Technology*, 4(3), 111-123.
- Yim, S. (2015). Coordinated control with electronic stability control and active steering devices. *Journal of Mechanical Science and Technology*, 29(12), 5409-5416.
- Nah, J., & Yim, S. (2019). Optimization of control allocation with ESC, AFS, ARS and TVD in integrated chassis control. *Journal of Mechanical Science and Technology*, 33(6), 2941-2948.
- Abe, M. (2015). *Vehicle handling dynamics: theory and application*. Butterworth-Heinemann.
- Milliken, W. F., & Milliken, D. L. (1995). *Race car vehicle dynamics* (Vol. 400, p. 16). Warrendale, PA: Society of Automotive Engineers.
- Vignati, M., Sabbioni, E., & Tarsitano, D. (2016). Torque vectoring control for IWM vehicles. *International Journal of Vehicle Performance*, 2(3), 302-324.
- Canale, M., Fagiano, L., Ferrara, A., & Vecchio, C. (2008). Vehicle yaw control via second-order sliding-mode technique. *IEEE Transactions on Industrial Electronics*, 55(11), 3908-3916.
- Yang, D., Idegren, M., & Jonasson, M. (2018). Torque vectoring control for progressive cornering performance in AWD electric vehicles. In *Proceedings of AVEC*.
- Rajamani, R. (2011). *Vehicle dynamics and control*. Springer Science & Business Media.
- Pacejka, H. (2005). *Tire and vehicle dynamics*. Elsevier.

- Goggia, T., Sorniotti, A., De Novellis, L., & Ferrara, A. (2014, June). Torque-vectoring control in fully electric vehicles via integral sliding modes. In 2014 American Control Conference (pp. 3918-3923). IEEE.
- Joa, E., Cha, H., Hyun, Y., Koh, Y., Yi, K., & Park, J. (2020). A new control approach for automated drifting in consideration of the driving characteristics of an expert human driver. *Control Engineering Practice*, 96, 104293.
- Brown, R. G., & Hwang, P. Y. (1997). Introduction to random signals and applied Kalman filtering: with MATLAB exercises and solutions. Introduction to random signals and applied Kalman filtering: with MATLAB exercises and solutions.
- Ljung, L. (1999). *System Identification. Theory for the User*. PTR Prentice Hall, Upper Saddle River, 609.
- Fujimoto, H., Tsumasaka, A., & Noguchi, T. (2005, November). Direct yaw-moment control of electric vehicle based on cornering stiffness estimation. In 31st Annual Conference of IEEE Industrial Electronics Society, 2005. IECON 2005. (pp. 6-pp). IEEE.
- Guo, K., & Guan, H. (1993). Modelling of driver/vehicle directional control system. *Vehicle system dynamics*, 22(3-4), 141-184.
- Nam, K., Fujimoto, H., & Hori, Y. (2015). Design of an adaptive sliding mode controller for robust yaw stabilisation of in-wheel-motor-driven electric vehicles. *International Journal of Vehicle Design*, 67(1), 98-113.
- Nam, K., Oh, S., Fujimoto, H., & Hori, Y. (2012). Design of adaptive sliding mode controller for robust yaw stabilization of in-wheel-motor-driven electric vehicles. *World Electric Vehicle Journal*, 5(2), 588-597.
- Chae, M., Hyun, Y., Yi, K., & Nam, K. (2019). Dynamic handling characteristics control of an in-wheel-motor driven electric vehicle based on multiple sliding mode control approach. *IEEE Access*, 7, 132448-132458.
- Gillespie, T. (1992). *Fundamentals of vehicle dynamics*. SAE international.
- Piyabongkarn, D., Grogg, J., Yuan, Q., Lew, J., & Rajamani, R. (2006). Dynamic modeling of torque-biasing devices for vehicle yaw control (No. 2006-01-1963). SAE Technical Paper.
- Gadola, M., & Chindamo, D. (2018). The mechanical limited-slip differential revisited: high-performance and racing car applications. *Int J Appl Eng Res*, 13, 1478-1495.
- Gadola, M., Chindamo, D., & Lenzo, B. (2018). On the passive limited slip differential for high performance vehicle applications.
- Piyabongkarn, D., Lew, J., Grogg, J., & Kyle, R. (2006). Stability-enhanced traction and yaw control using electronic limited slip differential. *SAE Transactions*, 931-941.



- Cha, H., Joa, E., Park, K., Yi, K., & Park, J. (2021). Integrated control of in-wheel motor and electronic limited slip differential for lateral stability and maneuverability (No. 2021-01-0974). SAE Technical Paper.
- Pacejka, H. B., & Bakker, E. (1992). The magic formula tyre model. *Vehicle system dynamics*, 21(S1), 1-18.
- Slotine, J. J. E., & Li, W. (1991). *Applied nonlinear control* (Vol. 199, No. 1, p. 705). Englewood Cliffs, NJ: Prentice hall.
- Khalil, H. K. (2015). *Nonlinear control* (Vol. 406). New York: Pearson.
- Edwards, C., & Spurgeon, S. (1998). *Sliding mode control: theory and applications*. Crc Press.
- Joa, E., Park, K., Koh, Y., Yi, K., & Kim, K. (2018). A tyre slip-based integrated chassis control of front/rear traction distribution and four-wheel independent brake from moderate driving to limit handling. *Vehicle system dynamics*, 56(4), 579-603.
- Song, J. (2008). Enhanced braking and steering yaw motion controllers with a non-linear observer for improved vehicle stability. *Proceedings of the Institution of Mechanical Engineers, Part D: Journal of Automobile Engineering*, 222(3), 293-304.
- MTS System Corporation (Ed.): *Flat-Trac III Tire Test Systems. Operation and Control Software Reference*, Eden 2005
- Bakker, E., Nyborg, L., & Pacejka, H. B. (1987). Tyre modelling for use in vehicle dynamics studies. *SAE Transactions*, 190-204.
- Ortiz, A. J. A. C., Cabrera, J. A., Guerra, A. J., & Simon, A. (2006). An easy procedure to determine Magic Formula parameters: a comparative study between the starting value optimization technique and the IMMa optimization algorithm. *Vehicle System Dynamics*, 44(9), 689-718.
- Ortiz, A., Cabrera, J. A., Guerra, A., & Simon, A. (2009). The IMMa optimisation algorithm without control input parameters. *Vehicle system dynamics*, 47(2), 243-264.
- Alagappan, A. V., Rao, K. N., & Kumar, R. K. (2015). A comparison of various algorithms to extract Magic Formula tyre model coefficients for vehicle dynamics simulations. *Vehicle System Dynamics*, 53(2), 154-178.
- Mathworks, "Documentation Optimization Toolbox-Least Squares (Model Fitting) Algorithms, 2016. [Online]. Available: [www.mathworks.co.kr](http://www.mathworks.co.kr)
- Zhang, L., Ding, H., Shi, J., Huang, Y., Chen, H., Guo, K., & Li, Q. (2020). An adaptive backstepping sliding mode controller to improve vehicle maneuverability and

- stability via torque vectoring control. *IEEE Transactions on Vehicular Technology*, 69(3), 2598-2612.
- Ataei, M., Khajepour, A., & Jeon, S. (2017). A novel reconfigurable integrated vehicle stability control with omni actuation systems. *IEEE Transactions on Vehicular Technology*, 67(4), 2945-2957.
- Ataei, M., Khajepour, A., & Jeon, S. (2020). Model predictive control for integrated lateral stability, traction/braking control, and rollover prevention of electric vehicles. *Vehicle system dynamics*, 58(1), 49-73.
- Li, L., Jia, G., Chen, J., Zhu, H., Cao, D., & Song, J. (2015). A novel vehicle dynamics stability control algorithm based on the hierarchical strategy with constrain of nonlinear tyre forces. *Vehicle system dynamics*, 53(8), 1093-1116.
- Zhang, L., Wu, Y., Li, B., Zhang, B., & Zhang, N. (2020). A novel manoeuvre stability controller based on vehicle state prediction and intellectual braking torque distribution. *Proceedings of the Institution of Mechanical Engineers, Part D: Journal of Automobile Engineering*, 234(1), 136-151.
- Kegelman, J. C., Harbott, L. K., & Gerdes, J. C. (2017). Insights into vehicle trajectories at the handling limits: analysing open data from race car drivers. *Vehicle system dynamics*, 55(2), 191-207.
- Maciejowski, J. M. (2002). *Predictive control: with constraints*. Pearson education.
- Borrelli, F., Bemporad, A., & Morari, M. (2017). *Predictive control for linear and hybrid systems*. Cambridge University Press.
- Mattingley, J., & Boyd, S. (2012). CVXGEN: A code generator for embedded convex optimization. *Optimization and Engineering*, 13(1), 1-27.
- Canudas-de-Wit, C., Tsiotras, P., Velenis, E., Basset, M., & Gissinger, G. (2003). Dynamic friction models for road/tire longitudinal interaction. *Vehicle System Dynamics*, 39(3), 189-226.
- Guo, K., Lu, D., Chen, S. K., Lin, W. C., & Lu, X. P. (2005). The UniTire model: a nonlinear and non-steady-state tyre model for vehicle dynamics simulation. *Vehicle system dynamics*, 43(sup1), 341-358.
- Cabrera, J. A., Castillo, J. J., Pérez, J., Velasco, J. M., Guerra, A. J., & Hernández, P. (2018). A procedure for determining tire-road friction characteristics using a modification of the magic formula based on experimental results. *Sensors*, 18(3), 896.
- Xu, N., Askari, H., Huang, Y., Zhou, J., & Khajepour, A. (2020). Tire force estimation in intelligent tires using machine learning. *IEEE Transactions on Intelligent Transportation Systems*.

- Brach, R., & Brach, M. (2011). The tire-force ellipse (friction ellipse) and tire characteristics (No. 2011-01-0094). SAE Technical Paper.
- Richalet, J., & O'Donovan, D. (2009). Predictive functional control: principles and industrial applications. Springer Science & Business Media.
- Woo, S., Cha, H., Yi, K., & Jang, S. (2021). Active differential control for improved handling performance of front-wheel-drive high-performance vehicles. *International journal of automotive technology*, 22(2), 537-546.
- Pugi, L., Favilli, T., Berzi, L., Locorotondo, E., & Pierini, M. (2020). Brake blending and torque vectoring of road electric vehicles: a flexible approach based on smart torque allocation. *IJEHV*, 12(2), 87.
- Xu, W., Chen, H., Zhao, H., & Ren, B. (2019). Torque optimization control for electric vehicles with four in-wheel motors equipped with regenerative braking system. *Mechatronics*, 57, 95-108.
- Geng, C., Uchida, T., & Hori, Y. (2007, November). Body slip angle estimation and control for electric vehicle with in-wheel motors. In *IECON 2007-33rd Annual Conference of the IEEE Industrial Electronics Society* (pp. 351-355). IEEE.
- Xiong, L., Yu, Z., Wang, Y., Yang, C., & Meng, Y. (2012). Vehicle dynamics control of four in-wheel motor drive electric vehicle using gain scheduling based on tyre cornering stiffness estimation. *Vehicle system dynamics*, 50(6), 831-846.
- De Novellis, L., Sorniotti, A., Gruber, P., & Pennycott, A. (2014). Comparison of feedback control techniques for torque-vectoring control of fully electric vehicles. *IEEE Transactions on Vehicular Technology*, 63(8), 3612-3623.
- Chen, Y., Hedrick, J. K., & Guo, K. (2013). A novel direct yaw moment controller for in-wheel motor electric vehicles. *Vehicle System Dynamics*, 51(6), 925-942.
- Ding, S., Liu, L., & Zheng, W. X. (2017). Sliding mode direct yaw-moment control design for in-wheel electric vehicles. *IEEE Transactions on Industrial Electronics*, 64(8), 6752-6762.
- Fujimoto, H., Takahashi, N., Tsumasaka, A., & Noguchi, T. (2006, March). Motion control of electric vehicle based on cornering stiffness estimation with yaw-moment observer. In *9th IEEE International Workshop on Advanced Motion Control, 2006*. (pp. 206-211). IEEE.
- Cha, H., Joa, E., Park, K., Park, J., & Yi, K. (2022). Torque vectoring control of a hybrid drive vehicle to enhance vehicle agility and stability. *Proceedings of the Institution of Mechanical Engineers, Part D: Journal of Automobile Engineering*, 09544070221125529.

- Kim, J., Lee, H., & Choi, S. (2012). A robust road bank angle estimation based on a proportional–integral  $H^\infty$  filter. *Proceedings of the Institution of Mechanical Engineers, Part D: Journal of automobile engineering*, 226(6), 779-794.
- Joa, E., Yi, K., & Hyun, Y. (2019). Estimation of the tire slip angle under various road conditions without tire–road information for vehicle stability control. *Control Engineering Practice*, 86, 129-143.
- Braghin, F., Brusarosco, M., Cheli, F., Cigada, A., Manzoni, S., & Mancosu, F. (2006). Measurement of contact forces and patch features by means of accelerometers fixed inside the tire to improve future car active control. *Vehicle System Dynamics*, 44(sup1), 3-13.
- Braghin, F., Cheli, F., & Sabbioni, E. (2011). Identification of tire model parameters through full vehicle experimental tests.
- Boyd, S., Boyd, S. P., & Vandenberghe, L. (2004). *Convex optimization*. Cambridge university press.
- Sano, S., Furukawa, Y., & Shiraishi, S. (1986). Four wheel steering system with rear wheel steer angle controlled as a function of steering wheel angle. *SAE Transactions*, 880-893.
- Rosolia, U., & Borrelli, F. (2017). Learning model predictive control for iterative tasks. a data-driven control framework. *IEEE Transactions on Automatic Control*, 63(7), 1883-1896.
- Rosolia, U., Carvalho, A., & Borrelli, F. (2017, May). Autonomous racing using learning model predictive control. In *2017 American Control Conference (ACC)* (pp. 5115-5120). IEEE.
- Kabzan, J., Hewing, L., Liniger, A., & Zeilinger, M. N. (2019). Learning-based model predictive control for autonomous racing. *IEEE Robotics and Automation Letters*, 4(4), 3363-3370.
- Hewing, L., Wabersich, K. P., Menner, M., & Zeilinger, M. N. (2020). Learning-based model predictive control: Toward safe learning in control. *Annual Review of Control, Robotics, and Autonomous Systems*, 3, 269-296.
- Mantripragada, V. K. T., & Kumar, R. K. (2022). Deep reinforcement learning-based antilock braking algorithm. *Vehicle System Dynamics*, 1-22.
- Ji, X., He, X., Lv, C., Liu, Y., & Wu, J. (2018). A vehicle stability control strategy with adaptive neural network sliding mode theory based on system uncertainty approximation. *Vehicle System Dynamics*, 56(6), 923-946.
- Kritayakirana, K., & Gerdes, J. C. (2012). Autonomous vehicle control at the limits of handling. *International Journal of Vehicle Autonomous Systems*, 10(4), 271-296.

- Beal, C. E., & Gerdes, J. C. (2012). Model predictive control for vehicle stabilization at the limits of handling. *IEEE Transactions on Control Systems Technology*, 21(4), 1258-1269.
- Kapania, N. R., & Gerdes, J. C. (2015). Design of a feedback-feedforward steering controller for accurate path tracking and stability at the limits of handling. *Vehicle System Dynamics*, 53(12), 1687-1704.
- Siampis, E., Velenis, E., Gariuolo, S., & Longo, S. (2017). A real-time nonlinear model predictive control strategy for stabilization of an electric vehicle at the limits of handling. *IEEE Transactions on Control Systems Technology*, 26(6), 1982-1994.
- Xu, N., Askari, H., Huang, Y., Zhou, J., & Khajepour, A. (2020). Tire force estimation in intelligent tires using machine learning. *IEEE Transactions on Intelligent Transportation Systems*.
- Herrmann, T., Wischnewski, A., Hermansdorfer, L., Betz, J., & Lienkamp, M. (2020). Real-time adaptive velocity optimization for autonomous electric cars at the limits of handling. *IEEE Transactions on Intelligent Vehicles*, 6(4), 665-677.
- De Castro, R., Tanelli, M., Araújo, R. E., & Savaresi, S. M. (2014). Minimum-time manoeuvring in electric vehicles with four wheel-individual-motors. *Vehicle system dynamics*, 52(6), 824-846.
- Smith, E. N., Velenis, E., Tavernini, D., & Cao, D. (2018). Effect of handling characteristics on minimum time cornering with torque vectoring. *Vehicle system dynamics*, 56(2), 221-248.
- Heilmeier, A., Wischnewski, A., Hermansdorfer, L., Betz, J., Lienkamp, M., & Lohmann, B. (2019). Minimum curvature trajectory planning and control for an autonomous race car. *Vehicle System Dynamics*.
- Kapania, N. R., Subosits, J., & Christian Gerdes, J. (2016). A sequential two-step algorithm for fast generation of vehicle racing trajectories. *Journal of Dynamic Systems, Measurement, and Control*, 138(9).
- Subosits, J., & Gerdes, J. C. (2015, July). Autonomous vehicle control for emergency maneuvers: The effect of topography. In *2015 American Control Conference (ACC)* (pp. 1405-1410). IEEE.
- Li, S. E., Chen, H., Li, R., Liu, Z., Wang, Z., & Xin, Z. (2020). Predictive lateral control to stabilise highly automated vehicles at tire-road friction limits. *Vehicle system dynamics*, 58(5), 768-786.
- Laurense, V. A., Goh, J. Y., & Gerdes, J. C. (2017, May). Path-tracking for autonomous vehicles at the limit of friction. In *2017 American control conference (ACC)* (pp. 5586-5591). IEEE.

- Hsu, Y. H. J., Laws, S. M., & Gerdes, J. C. (2009). Estimation of tire slip angle and friction limits using steering torque. *IEEE Transactions on Control Systems Technology*, 18(4), 896-907.
- Singh, K. B., & Taheri, S. (2015). Estimation of tire-road friction coefficient and its application in chassis control systems. *Systems Science & Control Engineering*, 3(1), 39-61.
- Choi, M., Oh, J. J., & Choi, S. B. (2013). Linearized recursive least squares methods for real-time identification of tire-road friction coefficient. *IEEE Transactions on Vehicular Technology*, 62(7), 2906-2918.
- Wang, R., Hu, C., Wang, Z., Yan, F., & Chen, N. (2015). Integrated optimal dynamics control of 4WD4WS electric ground vehicle with tire-road frictional coefficient estimation. *Mechanical Systems and Signal Processing*, 60, 727-741.
- Ribeiro, A. M., Moutinho, A., Fioravanti, A. R., & de Paiva, E. C. (2020). Estimation of tire-road friction for road vehicles: a time delay neural network approach. *Journal of the Brazilian Society of Mechanical Sciences and Engineering*, 42(1), 1-12.
- Khaleghian, S., Emami, A., & Taheri, S. (2017). A technical survey on tire-road friction estimation. *Friction*, 5(2), 123-146.
- Ko, S., Ko, J., Lee, S., Cheon, J., & Kim, H. (2015). A study on the road friction coefficient estimation and motor torque control for an in-wheel electric vehicle. *Proceedings of the Institution of Mechanical Engineers, Part D: Journal of Automobile Engineering*, 229(5), 611-623.
- Zhang, Z., Zheng, L., Wu, H., Zhang, Z., Li, Y., & Liang, Y. (2022). An estimation scheme of road friction coefficient based on novel tyre model and improved SCKF. *Vehicle system dynamics*, 60(8), 2775-2804.

## 초 록

### 극한 주행 핸들링 성능 개선을 위한 토크벡터링 제어 알고리즘

본 논문은 전륜 인휠모터와 후륜 전자식 차동 제한 장치를 이용하여 선회 성능 개선을 위한 토크벡터링 제어 알고리즘에 대해 포괄적으로 설명하였다. 본 논문에서 다루는 주요 연구 범위는 크게 두 가지 범주로 나뉠 수 있다. 첫 번째는 전륜 인휠모터를 이용한 개별적인 토크벡터링 제어이고, 두 번째는 전륜 인휠모터 및 후륜 전자식 차동제한장치를 모두 이용한 전후륜 통합 토크벡터링 제어이다.

첫 번째로, 후륜 구동 차량 내에서 두 개의 전륜 인휠 모터를 활용한 선회 성능 개선을 위한 제어 알고리즘이 설계되었다. 인휠 모터 독립 제어는 정상상태 제어 입력과 과도응답 상태 제어 입력으로 구성되어 있다. 정상상태 제어 입력은 차량의 언더스티어 구배를 변형하면서 정상상태 선회 반응을 개선하기 위해 고안되었고, 과도응답 상태 제어 입력은 차량의 요댐핑 계수를 증가시킴으로써 차량의 횡방향 안정성을 개선하기 위해 설계되었다. 제안된 알고리즘의 성능은 컴퓨터 시뮬레이션과 차량 실험을 통해 확인하였다. 실험 결과에서 알 수 있듯이, 제안된 알고리즘은 제어 목표를 달성하며 차량의 선회 성능을 개선할 수 있었다.

두 번째로, 각 액츄에이터의 특성을 고려하고 고속 주행 상황에서의 선회 성능을 개선하기 위해, 두 개의 전륜 인휠 모터와 후륜의 전자식 차동 제한 장치의 통합 제어 알고리즘이 설계되었다. 두 개의 전륜 인휠 모터는 피드포워드 제어를 기반으로 선회 성능을 개선하기 위해 제어되었고, 후륜의 전자식 차동 제한 장치는 요레이트 피드백 제어를 위해 활용되었다. 컴퓨터 시뮬레이션은 감가속을 포함한 공격적인 선회 상황에서 각 액츄에이터의 제어 효과를 보여주기 위해 수행되었다. 추가적으로, 차량 실험 결과를 통해 제안된 제어기가 제어되지 않은 경우에 비해 핸들링 한계 상황에서의 선회 성능을 개선할 수 있다는 점을 보여주었다.

요약하자면, 본 연구에서는 차량의 언더스티어 그래디언트와 요레이트 댐핑 특성에 기반한 한계 핸들링 성능 개선을 위한 제어 알고리즘을 제안하였다. 또한, 인휠모터와 전자식 차동 제한 장치의 각 액추에이터 특성을 고려하여 인휠모터와 전자식 차동 제한 장치의 통합 제어에 대해 다루었다. 제안된 인휠모터 제어기는 정상상태 선회에서의 언더스티어 그래디언트와 과도응답상태 선회에서의 요레이트 댐핑 특성을 변형하기 위해 고안되었고, 전자식 차동 제한 장치 제어는 목표 요레이트를 추종하기 위해 설계되었다. 제안된 제어기를 검증하기 위해, 컴퓨터 시뮬레이션과 실차 실험이 진행되었고, 차량의 선회 안정성과 민첩성이 채터링 문제없이 확연히 개선된다는 것을 보여주었다. 추가적으로, 레이싱 트랙에서의 실차 실험을 통해 개선된 한계 핸들링 성능 또한 제시되었다.

주요어 : 토크벡터링 제어, 통합 샴시 제어, 비선형 제어, 차량 동역학 및 제어, 차량 상태 추정

학 번 : 2018-25595